Remote sensing of UV-absorbing aerosols using space-borne spectrometers

de Graaf, M.

2006

document version
Publisher's PDF, also known as Version of record

citation for published version (APA)
de Graaf, M. (2006). *Remote sensing of UV-absorbing aerosols using space-borne spectrometers*. [PhD-Thesis - Research and graduation internal, Vrije Universiteit Amsterdam].

Remote sensing of UV–absorbing aerosols using space–borne spectrometers

Martin de Graaf

STELLINGEN

behorende bij het proefschrift:

'Remote sensing of UV-absorbing aerosols using space-borne spectrometers'

Martin de Graaf, 19 juni 2006

1. De residuemethode is ongeschikt voor toepassingen voorbij het UV, door de afname van het Rayleigh signaal in de reflectantie bij langere golflengten en de daarbij behorende relatieve toename van de bijdrage van de bodemreflectie.

2. De residuemethode is in het UV zeer geschikt voor de analyse van aërosolinformatie in heldere, door wolken verontreinigde, scènes, en kan bijdragen aan een beter begrip van het indirecte aërosoleffect.

3. De AAI is een drempelwaarde-grootheid en daarom statistisch onhandig. Voor statistische analyses moet het residue (of een andere normaal verdeelde grootheid) gebruikt worden.

4. De geschiktheid van de residuemethode voor de detectie van roetdeeltjes tot vlak boven ijs- en sneeuwoppervlakken wordt niet veroorzaakt door de onderdrukking van Rayleigh verstrooiing, zoals verondersteld door Hsu c.s. (1999), maar door de golflengte-afhankelijkheid van de optische dikte van roet in het UV.

5. Het belang van leestekens wordt vaak zwaar onderschat, wat wel blijkt uit de eis voor een proefschrift die wordt gesteld in het Statuut VU, artikel 2.25, vierde lid: „Het proefschrift mag niets bevatten, wat is contra Deum aut bonos mores." (Uiteraard heb ik me aan deze eis niet gehouden.)

6. Goed wetenschappelijk werk zal uiteindelijk altijd door experts gewaardeerd worden, maar alleen frauduleuze praktijken garanderen de aandacht van het grote publiek.

7. In 2005 was de sectie 'Buitenland' van *De Telegraaf* (grootste krant van Nederland, oplage 752.721) verstopt achter gemiddeld 7.4 pagina's 'Binnenland' en ander "nieuws"; in bijvoorbeeld het *NRC Handelsblad* (oplage 267.140) was dit 2.0. Wie het vermaledijde gebrek aan kennis over 'Europa' bij de Nederlandse burger wil verbeteren, moet blijkbaar eerst het vak paparazzi verbieden, de veiligheid op de Nederlandse wegen verbeteren en de monarchie afschaffen.

8. Klaverjassen is nooit een kwestie van geluk, soms heb je alleen pech.

9. Net als in België zouden in het verkeer bestuurders het recht op voorrang moeten verliezen zodra ze stil staan; dit zal niet het einde maar wel een oplossing zijn voor automobilisten die weigeren het voorrang te accepteren van van links naderende fietsers.

10. Met het afnemende gebruik van de beleefdheidsvorm u/uw wordt de vorm jou/jouw in toenemende mate foutief gebruikt, door het wegvallen van de analogie. Dit zal in enkele generaties gecorrigeerd worden door het accepteren van het nu al gebezigde jou/joun, in analogie met mij/mijn.

11. Wie nooit van mening verandert, heeft weinig geleerd. (*NRC Handelsblad*)

VRIJE UNIVERSITEIT

Remote sensing of UV–absorbing aerosols using space–borne spectrometers

Remote sensing van UV–absorberende aërosolen met behulp van satellietspectrometers

(met een samenvatting in het Nederlands)

ACADEMISCH PROEFSCHRIFT

ter verkrijging van de graad Doctor aan
de Vrije Universiteit Amsterdam,
op gezag van de rector magnificus
prof.dr. T. Sminia,
in het openbaar te verdedigen
ten overstaan van de promotiecommissie
van de faculteit der Exacte Wetenschappen
op maandag 19 juni 2006 om 13.45 uur
in de aula van de universiteit,
De Boelelaan 1105

door

Martin de Graaf

geboren te Hengelo (O)

promotor: prof.dr. E.A.A. Aben
copromotor: dr. P. Stammes

Cover photos: ’Cumulus forms over a bushfire, Great Sandy Desert, Western Australia’ and ’Dust storm, Alice Springs, Australia’. Photos by Steve Strike.

Graaf, Martin de
Remote sensing of UV–absorbing aerosols using space-borne spectrometers.

ISBN-10: 90-9020628-0
ISBN-13: 978-90-9020628-8

Contents

Samenvatting

De studie naar aërosolen heeft de laatste decennia een enorme vlucht genomen, sinds het besef dat deze kleine, nauwelijks waarneembare deeltjes onze leefomgeving in sterke mate beïnvloeden. Aërosolen spelen een grote rol in klimaatverandering en luchtverontreiniging. Met name bij het bepalen van de toenemende invloed van de mens op het klimaat zijn aërosolen van doorslaggevend belang: in het laatste verslag in 2001 van het Intergovernmental Panel on Climate Change (IPCC), de organisatie die is belast met het bijeenbrengen van de nieuwste wetenschappelijke inzichten in klimaatverandering, werden aërosolen aangewezen als de belangrijkste bron van onzekerheid in klimaatmodellering. Dit heeft het aërosolonderzoek enorm gestimuleerd en de laatste jaren geleid tot een verbeterd inzicht in de invloed van aërosolen.

Een andere stap die heeft geleid tot een enorme verbetering van onze kennis over aërosolen is het lanceren van kunstmatige satellieten waarmee de aarde en de atmosfeer 24 uur per dag geobserveerd kunnen worden. Satellietinstrumenten kunnen de aarde in één dag helemaal in beeld brengen, of een deel van de aarde continu in de gaten houden. Dit is gunstig voor aërosolonderzoek, omdat de verspreiding van aërosolen onregelmatig is, zodat metingen vanaf een enkele plek op de aarde geen goed beeld geven van de globale verdeling, en sommige aërosolbronnen ver weg van de bewoonde wereld liggen.
Satellietinstrumenten zijn er in veel soorten en maten. In dit proefschrift worden de satellietspectrometers GOME en SCIAMACHY gebruikt om aërosolinformatie af te leiden uit de metingen van het zonlicht dat weerkaatst wordt in de atmosfeer en aan het aardoppervlak.

Aërosolen

Aërosolen zijn verzamelingen van kleine, vloeibare of vaste, deeltjes die in de atmosfeer zweven. Wolkendruppeltjes en ijskristallen vallen in principe ook onder deze definitie, maar vaak worden deze apart behandeld. De interactie tussen wolkendeeltjes en andere aërosolen is namelijk zeer belangrijk, aangezien de atmosfeer zeer veel waterdamp bevat en de meeste aërosolen water aantrekken en daardoor kunnen uitgroeien tot wolkendruppels. Aërosolen fungeren zo als wolkencondensatiekernen. Als deze druppels groot genoeg worden, vallen de deeltjes vanzelf terug naar de aarde. Dit is meteen het belangrijkste mechanisme van de verwijdering van aërosolen uit de atmosfeer.
Bronnen van aërosolen zijn gassen die door chemische reacties in vaste of vloeibare vorm worden omgezet, of deeltjes die direct door chemische of mechanische processen in de at-

mosfeer worden gebracht. Voorbeelden van de laatste soort deeltjes zijn woestijnzand dat door de wind van de bodem losraakt, rook van branden, vulkaanas, en zeezout dat uit druppels zeewater ontsnapt.
Het belang van aërosolen voor klimaatdynamica en -verandering is hun eigenschap om zonlicht te verstrooien en te absorberen. Lichtverstrooiing in de atmosfeer is een verschijnsel dat iedereen kent als bijvoorbeeld regenbogen, halo's, het rood van de ondergaande zon en het blauw van de lucht. Als een lichtbundel van de zon de aardse atmosfeer binnendringt, wordt deze verstrooid waardoor de energie van de bundel in verschillende richtingen wordt uitgesmeerd. Als een deeltje ook nog absorberend is, wordt een deel van de energie van de lichtbundel omgezet in warmte, waardoor plaatselijk de atmosfeer verwarmd wordt. Hierdoor spelen aërosolen een belangrijke rol in de stralingsbalans van de aarde, die bepaalt wat de temperatuur in de atmosfeer en aan het aardoppervlak is.

Drie soorten aërosolen absorberen ultraviolet (UV) licht: vulkaanas, woestijnzand en rook (roet). Vulkaanas zal hier niet worden behandeld, omdat deze deeltjes met name invloedrijk zijn als ze lang in de stratosfeer voorkomen, wat alleen gebeurt na zeer zware vulkaanuitbarstingen, zoals die van El Chicon in 1982 en Pinatubo in 1992. De laatste jaren is de concentratie vulkaanas in de stratosfeer gedaald tot de achtergrondwaarde.
Woestijnzand bestaat uit relatief grote mineraaldeeltjes die in de atmosfeer worden geblazen als de windsnelheid groot genoeg is en er een vertikale windschering is, waardoor de deeltjes omhoog geblazen kunnen worden. Grote pluimen woestijnzand komen veel voor in de woestijnband rond 20 tot 30 graden noorderbreedte waar de meeste woestijnen liggen (Fig. 1.1), maar ook op het zuidelijk halfrond zijn woestijnen, en lokaal zijn droge rivierbeddingen belangrijke bronnen. Mineraaldeeltjes worden vaak gevonden in droge en wolkenloze lucht. Dit is gunstig voor satellietmetingen van aërosolen, omdat wolken zeer sterk licht verstrooien en daardoor de relatief zwakke verstrooiing van het licht door aërosolen verhullen.
Rook komt vaak voor in droge gebieden waar veel bos, savanne of ander brandbaar materiaal is. Er is een sterke negatieve correlatie tussen rook en neerslag, niet alleen omdat door neerslag aërosolen uitregenen, maar ook omdat branden voornamelijk ontstaan tijdens langdurige droge perioden (Fig. 3.3). Daarentegen trekken rookdeeltjes wel gemakkelijk water aan en zijn daardoor effectieve wolkencondensatiekernen. Dit is ongunstig voor satellietmetingen van rook, omdat rook daardoor vaak voorkomt in, boven of onder wolken.

Satellietmetingen van aërosolen

GOME en SCIAMACHY zijn satellietinstrumenten van de Europese ruimtevaartorganisatie ESA. GOME werd in april 1995 gelanceerd aan boord van de ERS-1 satelliet. SCIAMACHY, gebouwd door Duitsland, Nederland en België, werd gelanceerd in maart 2002 aan boord van de Envisat satelliet. Beide instrumenten zijn spectrometers die vanuit de ruimte het door de aarde en atmosfeer weerkaatste zonlicht meten in een groot spectraal gebied; in het UV, het zichtbare en infrarode (IR) golflengte-gebied. Het meten in het UV heeft als voordeel dat vrijwel alle gebieden op aarde donker zijn (met uitzondering van ijs- en sneeuwoppervlakken) waardoor het gemeten signaal hoofdzakelijk door de atmosfeer wordt bepaald. Hierdoor kunnen zowel boven land als boven oceaan dezelfde technieken worden gebruikt. Dit is niet onbelangrijk, omdat landoppervlak heel helder kan zijn voorbij het UV, met name woes-

tijngebieden en gebieden met vegetatie, waardoor de fout in de metingen van de atmosfeer groot kan worden. Daarom hebben aërosolmetingen boven land en oceaan vaak verschillende nauwkeurigheden.
Een techniek die gebruik maakt van metingen van de reflectantie van het aarde/atmosfeer-systeem bij twee golflengten in het UV is de Absorbing Aerosol Index (AAI) techniek. Deze techniek bepaalt de afwijking van het gemeten signaal ten opzichte van het signaal dat zou worden gemeten wanneer de atmosfeer alleen uit gassen zou bestaan (zonder wolken en aërosolen). Zo'n atmosfeer wordt een Rayleigh-atmosfeer genoemd, naar het verstrooiingsproces van gassen. Het verwachte signaal is goed te bepalen met behulp van stralingstransportmodellen. De afwijking wordt het residu genoemd en ontstaat door de afscherming van de Rayleigh-atmosfeer onder de aërosollaag. Het residu is zo gekozen dat absorberende aërosolen positieve residuen geven en wolken en verstrooiende aërosolen negatieve residuen (vgl. 1.12). Hierdoor kunnen met positieve residuen absorberende aërosolen in kaart worden gebracht. Een positief residu wordt een AAI genoemd. Het grote voordeel van de AAI is dat deze boven zowel land als oceaan en zelfs boven sneeuw en ijs kan worden gebruikt, en dat wolken geen invloed hebben zolang de aërosolen boven de wolken zitten. De AAI methode werd in de jaren '90 ontwikkeld voor het Amerikaanse satellietinstrument TOMS, dat al sinds 1978 metingen verricht. In dit proefschrift zijn residuen bepaald uit metingen van GOME en SCIAMACHY.

Hoofdstuk 2

In de jaren na de eerste beschrijving van de AAI methode werd de methode in toenemende mate gebruikt voor satellietmetingen van verdelingen van aërosolen boven zowel land als oceaan. Toch is de interpretatie van de AAI verre van eenduidig en geeft de AAI niet een pur sang beeld van aërosolverdelingen. Daarom wordt in hoofdstuk 2 een uitvoerige analyse van de fysische betekenis van de AAI beschreven. De AAI blijkt gevoelig te zijn voor de hoeveelheid aërosolen in de atmosfeer, de mate waarin de aërosolen straling absorberen en de hoogte waarop de aërosolen voorkomen. Dit laatste is een gevolg van de gevoeligheid van het residu voor de hoeveelheid Rayleigh-atmosfeer onder de aërosollaag. Aangezien de hoogte van een aërosollaag vaak onbekend is, is de conversie van de AAI naar belangrijke aërosolgrootheden als aërosol optische dikte en enkelvoudige verstrooiingsalbedo moeilijk. Een andere afhankelijkheid, die ook tot een positief residu kan leiden zonder dat er Rayleigh-atmosfeer wordt afgeschermd, is de golflengte-afhankelijkheid van de brekingsindex van de aërosolen. Andere, minder gevoelige, afhankelijkheden zijn de afhankelijkheid van de gekozen golflengten, de helderheid van het oppervlak, de gronddruk in de gemeten scène, polarisatie van het licht, het vóórkomen van wolken(flarden) in de gemeten scène en de hoek waaronder wordt gemeten.
De AAI methode is toegepast op GOME data van 1995 tot 2000 en vergeleken met bestaande AAI data en aërosolmetingen. De AAI bleek erg gevoelig te zijn voor meetfouten en er kwamen nog onbekende calibratiefouten van GOME aan het licht. Deze zijn gecorrigeerd en de AAI data bleek goed overeen te komen met bekende AAI data van TOMS. De reeks van TOMS AAI wordt veel gebruikt, maar er is geen TOMS data in de periode van mei 1993 tot juni 1996 omdat er in die periode geen TOMS instrument beschikbaar was. De GOME AAI kan een deel van deze ontbrekende data, van juli 1995 tot oktober 1996, invullen.

Hoofdstuk 3

Hoofdstuk 3 beschrijft toepassingen van de GOME AAI data uit hoofdstuk 2. Voor vijftien gebieden op de aarde, waar regelmatig aërosolen voorkomen, is een tijdreeks van gemiddelde residuen gemaakt. Deze reeksen laten zien dat er een grote jaarlijkse gang is in de aanwezigheid van aërosolen in de meeste gebieden, die meestal verklaard kan worden door de jaarlijkse gang in het klimaat van een gebied, met name de wisseling van natte en droge perioden en windregimes. Het laat ook zien dat negatieve residuen nog veel onbekende informatie over geofysische grootheden bevatten.

In hoofdstuk 3 is de analyse van de AAI verder uitgebreid door de methode niet alleen toe te passen bij twee golflengten in het UV, maar bij elf paren van golflengten in het hele bereik van GOME. Eén van de twee gekozen golflengten moest echter wel in het UV liggen, anders verstoorde een helder oppervlak in het zichtbare licht de AAI metingen direct. Deze spectrale residuen, de spectrale reflectanties die GOME meet, en de informatie uit de tijdreeksen werden gecombineerd om te bepalen of het mogelijk is om eenduidig gedrag te vinden in de reflectanties en/of residuen voor verschillende typen aërosolen. Het bleek dat alleen boven oceanen eenduidig kon worden aangegeven wanneer rook voorkwam in combinatie met wolken. Boven land werden de uitkomsten volledig bepaald door de eigenschappen van het oppervlak.

Hoofdstuk 4

Hoofdstuk 4 beschrijft de toepassing van de AAI methode op SCIAMACHY data. De gevoeligheid van de methode bracht de calibratie-onzekerheden van de reflectanties van SCIAMACHY, die op dat moment al door verschillende onderzoekers waren geconstateerd en zeer groot waren, goed in kaart. Voor SCIAMACHY waren vóór lancering al AAI metingen gepland en was een algorithme in de operationele dataprocessor geïmplementeerd. Deze operationele AAI (L2-AAI) maakt gebruik van de vooralsnog slecht gecalibreerde reflectanties van SCIAMACHY en bovendien van stralingstransport-berekeningen waarbij polarisatie verwaarloosd was. De invloed van deze factoren maakt de L2-AAI onbruikbaar. Daarom is een nieuwe AAI bepaald, de *scientific* AAI (SC-AAI), voor alle SCIAMACHY data vanaf het moment dat de eerste data beschikbaar kwam, in juli 2002. De SC-AAI wordt nu dagelijks bepaald, maar in hoofdstuk 4 wordt alleen data tot eind 2004 geanalyseerd.

De SC-AAI werd vergeleken met de TOMS AAI, maar tussentijds werd de definitie van de TOMS AAI veranderd; de twee golflengten waarbij de AAI werd bepaald werden omgedraaid. Dit heeft niet-lineaire veranderingen tot gevolg, zoals ook wordt aangetoond in hoofdstuk 2, waar het de vergelijking bemoeilijkte. De verschillen tussen de verschillende TOMS AAI versies en de SC-AAI worden in hoofdstuk 4 uitvoerig beschreven.

Schittering van zonlicht op oceaanoppervlakken bleek een groot positief residu op te leveren, wat geïnterpreteerd zou kunnen worden als het vóórkomen van absorberende aërosolen. In gebieden waar deze schittering kan optreden zijn positieve residuen verwijderd.

Hoofdstuk 5

Hoofdstuk 5 beschrijft de analyse van twee scènes boven de zuid-Atlantische Oceaan met behulp van SCIAMACHY reflectanties. In één scène bevindt zich wolkenloze lucht met woestijnzand (DDA), in de andere wolken met rook (BBA). Beide hebben ongeveer dezelfde residu-waarde van rond de $3\frac{1}{2}$, maar in beide scènes worden deze residuen duidelijk door verschillende mechanismen veroorzaakt. In hoofdstuk 5 worden deze mechanismen blootgelegd.

De eerste, DDA, scène is een klassieke aërosolscène met goed te bepalen aërosolhoeveelheden. Zonder wolken en met een grote hoeveelheid aërosol is boven de oceaan een goede bepaling mogelijk van de aërosol optische dikte. De AAI wordt in dit geval bepaald door de afscherming van de Rayleigh-laag onder de aërosollaag. Dit wordt aangetoond door de scène te simuleren met een aërosollaag tussen drie en vier kilometer hoogte en een aërosol optische dikte zoals die werd gemeten door MODIS, een spectrometer van de Amerikaanse ruimtevaartorganisatie NASA, met een hoge ruimtelijke resolutie. De hoeveelheid afgeschermde Rayleigh-atmosfeer is in dit geval voldoende om het gevonden residu te verklaren.

De tweede, BBA, scène is een scène met een hoge reflectantie, die veroorzaakt wordt door de aanwezigheid van wolken. Bepaling van de aërosol optische dikte is in dit geval niet mogelijk met de technieken die MODIS of andere satellietinstrumenten gebruiken, zoals in de inleiding van deze samenvatting werd genoemd. Een bepaling van de AAI is echter wel mogelijk, en de verklaring hiervan is onderzocht met behulp van het SCIAMACHY reflectantiespectrum. Het bleek dat in dit geval niet Rayleigh-verstrooiing, maar de verstrooiing door de wolkendruppeltjes onder de aërosollaag werd afgeschermd, met uiteindelijk een vergelijkbaar effect op het residu. Omdat de optische dikte van wolken heel groot is, maakt de hoogte boven de aërosollaag boven de wolk niet meer uit, terwijl de hoogte van een afgeschermde Rayleigh-laag juist heel sterk bepalend is voor de grootte van het residu. Dit verklaart ook waarom de AAI methode werkt boven sneeuw en ijs: een helder oppervlak heeft hetzelfde effect als een wolk onder een aërosollaag. Dit betekent dat rook boven sneeuw en ijs kan worden gedetecteerd tot vlak boven het oppervlak met de AAI methode.

De tweede scène is met verschillende modellen voor de rook- en wolkenlaag gesimuleerd, om te onderzoeken of de rook ook ín de wolkenlaag kan voorkomen, aangezien rookdeeltjes zeer effectieve wolkencondensatiekernen zijn. De modellen gaven geen uitsluitsel over de positie van de aërosollaag ten opzichte van de wolkenlaag, zolang er maar absorptie boven of bovenin de wolk kan plaatsvinden. Voor het kwantificeren van de hoeveelheid aërosolen en mate van absorptie door de aërosolen is een correcte beschrijving van de positie van de aërosolen echter wel essentiëel.

1

Introduction

A.D. 2006, research on aerosols can justifiably be called a hot topic. Aerosols have played an increasingly dominant role in climate research over the last decades. Their role in climate dynamics was recognised long ago, but the interest of the public and broader scientific community was raised when the effects of anthropogenic air pollution became ever more apparent. Aerosols have played a role in many of the popular atmospheric physics topics of the past few decades. Those topics include acid rain, caused by aerosol precursors; the ozone hole, a reduction of our vital stratospheric ozone layer caused by release of CFC's; global warming, caused by the exhaust of anthropogenic fossil fuel combustions, which is possibly amplified or damped by aerosols; global dimming, the reduction of sunlight at the Earth's surface, resulting directly from the increasing amount of anthropogenic aerosols and indirectly from the increase of aeroplane contrails or more complex cloud dynamics.

Much of the research on atmospheric physics and chemistry is aimed at assessing the anthropogenic factor of our changing climate. The anthropogenic era, postulated to have begun as long as 10,000 years ago creating an anomalously stable, warm Holocene [*Ruddiman*, 2003], but definitely apparent since the industrial revolution, has undoubtedly had a tremendous effect on atmospheric processes, creating unbalances that are not yet fully understood. The realisation that we are only at the beginning of this era (or for some the fear that we are approaching the end), triggers emotions ranging from the need to diminish our influence on climate, increase our influence in order to be able to regulate climate to mankind's needs, or the need for scientific understanding. However, many scientific assessments of future climate change are based on climate models extrapolating in time, which may introduce large errors, especially since our understanding of current and earlier climates is still very limited.

The relationship between aerosol research and social issues has been invariably large over recent years. One of the more dramatic recent examples followed from the 2001 attacks on the WTC buildings in New York. The subsequent five day ban on U.S. air traffic provided an unexpected opportunity to assess the effect of contrails, in a period of ever increasing air transport. Another issue is the continuing air pollution of western countries and the rapidly increasing contribution by developing countries, which raises moral dilemmas of economic and environmental conflicts. In the Netherlands, the term 'aërosolen' was forced upon the general public in 2005, when E.U. air pollution regulations were strictly applied by Dutch judges, forcing several construction sites to a grinding halt. The greatest boost of aerosol research however, was given by the Intergovernmental Panel on Climate Change (IPCC), which in their latest (2001) assessment of anthropogenic influence on climate change concluded that aerosols provided the largest uncertainties in climate modelling.

Another major step was the start of the satellite era. With the launch of satellites orbiting the Earth, the possibility was created to observe the Earth and its atmosphere from space. From the start, aerosol scattering has played a role in space-borne remote sensing. First because aerosol effects blur the images of the surface or interesting atmospheric features, which have to be corrected for, later satellite instruments were developed specifically to monitor the variable distributions of aerosols themselves. The relatively new technology of space-borne remote sensing is rapidly developing and many possibilities of this complex technique are still unexplored. Possibilities that are quickly becoming more numerous with the increasing number of satellites in space, carrying increasingly better calibrated instruments, with higher spatial and spectral resolution, and added capabilities. Undoubtedly, this will stimulate aerosol research even further in the future.

Aerosols are currently a focal point in a search for understanding the driving mechanism of the dynamics of our climate. Processes that we experience every day are ultimately driven by the differential warming of the Earth by the sun. The tiny aerosol represents a large gap in understanding this driving force in the Earth's atmosphere.

1.1 Outline of the thesis

Satellite remote sensing of aerosols presents multiple challenges and opportunities. The main challenges are the retrieval of basic aerosol properties over land surfaces, retrieval of aerosol properties under cloudy conditions, and retrieval of different aerosol parameters based on measurements instead of a priori assumptions. Possibilities lay in the tremendous amount of unexplored data from historic, current and future satellite missions.

A relatively new method of aerosol remote sensing is the residue or Absorbing Aersol Index (AAI) method, which is the focus of this thesis. The AAI uses two reflectance measurements in the ultraviolet (UV) wavelength range and radiative transfer model inversion techniques. However, the interpretation of the residue and AAI is difficult, due to the many dependencies and the limited knowledge of the processes governing the residue method. As an increasing number of users are applying the AAI, a thorough knowledge of these processes is crucial. Therefore, the first question addressed in this thesis is: *What are the fundamental sensitivities of the residue method and AAI?*

The residue method has until recently only been applied to data from Total Ozone Mapping Spectrometer (TOMS), except for a few limited studies of the AAI from Global Ozone Monitoring Experiment (GOME) data. In this thesis the aerosol information content in the broad spectral range of GOME and SCanning Imaging Absorption SpectroMeter for Atmospheric CartograpHY (SCIAMACHY) reflectance measurements are explored. These space-borne spectrometers from the European Space Agency (ESA) provide reflectance measurements in the UV, so in principle the residue method can be applied to data from these instruments. However, the characteristics of GOME, SCIAMACHY and TOMS are different, e.g. the orbits and the footprints. Therefore, independent and complementary datasets can be retrieved from the European spectrometers, but the relationship with the TOMS AAI dataset is unknown. Hence, the second question addressed in this thesis is: *How do GOME and*

SCIAMACHY AAI datasets relate to the TOMS AAI and what are the characteristics of the different datasets?

Since the residue is very sensitive to errors in the reflectance measurements, it can be a useful tool to asses and monitor reflectance calibration errors. SCIAMACHY was launched in 2002 and the calibration of the radiance and irradiance measurements was highly uncertain in the first few years it was in orbit. Therefore, the third question addressed in this thesis is: *How accurate are SCIAMACHY reflectances based on residue measurements?*

The broad spectral range of GOME and SCIAMACHY measurements provide opportunities to improve the residue method, apply it in other spectral regions and investigate reflectance spectra of scenes with a known aerosol content, based on the AAI datasets. Therefore, the fourth question addressed in this thesis is: *Is there additional aerosol information content in the broad spectral range of GOME and SCIAMACHY measurements, and can it be used to derive additional aerosol parameters?*

These questions are addressed in the following chapters. A short overview of the contents of the chapters is given below.

In **chapter 2** the aerosol information content of the AAI is assessed. An extensive sensitivity study of the AAI is described, showing the possibilities and limitations of this quantity for aerosol retrieval. The AAI method is explained and the difficulties interpreting the quantity are indicated. The AAI method is applied to GOME data, complementing a part of the AAI data set not covered by TOMS. The GOME AAI is compared to the TOMS AAI, showing the similarities between the two quantities and the differences due to the differences between the two instruments.

In **chapter 3** the broad spectral range of GOME is explored to improve the AAI method. First, the temporal characteristics of aerosol distributions in many regions on Earth are determined using a 5.5 year GOME AAI data set. Then, instead of using two wavelengths in the UV, the residue is determined for eleven wavelengths in the entire spectral range of GOME. These spectral residues and GOME reflectance data are explored in regions where the occurrence of UV-absorbing aerosol types is relatively stable, to find spectral fingerprints of these aerosol types. A type separating algorithm on the basis of the information in GOME spectral data is studied.

In **chapter 4** the AAI is determined from SCIAMACHY data. The strong sensitivity of the AAI to reflectance differences is used to investigate inaccuracies in SCIAMACHY's reflectance measurements. An error in SCIAMACHY's operational AAI, part of the standard product set of SCIAMACHY, due to polarisation neglect in the radiative transfer modelling is demonstrated and corrected. A sunglint mask is proposed and applied. SCIAMACHY's AAI is compared to the AAI from TOMS and GOME.

In **chapter 5** a detailed study of reflectances at the top of the atmosphere (TOA) for a cloudless desert dust scene and a cloudy biomass burning scene over the ocean is performed using the spectral range of SCIAMACHY measurements. Both scenes have an equally high AAI, but the mechanism creating the high AAI is different. The reflectance spectra are simulated using radiative transfer modelling and the aerosol related processes governing the radiative transfer in the scenes are determined. The different mechanisms leading to an enhanced residue are identified, which can help improve aerosol type separating algorithms. Aerosol absorption in a cloudy scene is demonstrated and quantified.

First, an introduction is given of the main processes and concepts used in this thesis.

1.2 Aerosols and Climate

Atmospheric aerosols are solid or liquid phase particles in the atmosphere. Liquid water and ice particles are usually excluded from this definition, but this is a historical and not a physical subdivision. Aerosols range in size from a few tenths of a nanometre to about a hundred micrometres. They can be emitted directly as particles (primary aerosol) or formed by gas-to-particle conversion processes (secondary aerosol) from aerosol precursor gases like sulphur dioxide and nitrogen oxides. Aerosols are removed from the atmosphere by dry or wet deposition. Dry deposition is the return of aerosols to the surface by gravity or dynamic processes. This is the most important removal process for larger particles, since the viscous drag is proportional to the particle radius, while the gravitational force is proportional to the particle volume. Wet deposition is the removal of aerosols from the atmosphere by precipitation. Aerosols can form cloud droplets and precipitate (in-cloud scavenging) or be incorporated in falling rain droplets (below-cloud scavenging). For averaged-sized particles in-cloud scavenging is more important than below-cloud scavenging, as falling cloud droplets produce a flow field around the droplet followed by the aerosol particle, preventing scavenging. Below-cloud scavenging is important for very small particles, of which the Brownian motions exceed the rain droplet fall velocity, and for coarse particles with large inertness [*Henzing et al.*, 2006].

1.2.1 Aerosol radiative effect

Aerosols scatter and can absorb solar radiation and scatter, absorb and emit thermal radiation. Therefore, the addition of aerosols to the atmosphere may change the radiative fluxes at TOA, at the surface, and within the atmospheric column. A positive radiative effect at TOA indicates addition of energy to the system (i.e. warming) whereas a negative effect indicates a loss of energy (i.e. cooling) [*Yu et al.*, 2006]. Absorption of radiation by aerosols may warm the atmosphere, but locally cool the surface, while the net radiative effect may switch sign depending on aerosol altitude [*Penner et al.*, 2003].

Estimates of aerosol direct effect, based on measurements, are most accurate over the dark oceans, where space-based aerosol parameter retrievals are not hindered by high surface reflections. The currently best estimate for aerosol direct forcing at TOA is -5.5 ± 0.2 Wm^2 over the oceans [*Yu et al.*, 2006], although this number might be 10% too high due to thin cirrus contaminated aerosol retrievals. Over land the aerosol direct forcing is much less accurate, due to the high surface reflections over land. Currently, the best estimate for the direct aerosol forcing at TOA over land is -4.9 ± 0.7 Wm^2 [*Yu et al.*, 2006]. A good quantification of the aerosol direct effect at the surface is hampered by the poorly known aerosol absorption. Especially under cloudy conditions aerosol retrievals are difficult and the knowledge of aerosol absorption limited.

In general, the quantification of the direct effect of aerosols is complicated by their effects as cloud condensation nuclei (CCN) and ice nuclei (IN), changing cloud microphysics and the hydrological cycle. These indirect aerosol effects will be discussed below.

1.2.2 Aerosols and clouds

Clouds have traditionally had a separate place in atmospheric physics, probably because clouds have always fascinated people, while aerosols usually escape people's attention, except perhaps in desert areas and near fires. However, aerosols and clouds are closely connected and especially in recent years the unravelling of the issues associated with the connections between clouds and aerosols has developed rapidly.

As stated, precipitation is an important removal process for aerosols globally and the distribution of clouds and water vapour affect the distribution of aerosols. On the other hand, aerosol affect the forming of clouds by acting as CCN and IN. Clouds themselves are an important regulator of the Earth's radiation budget. About 60% of the Earth's surface is covered with clouds. Clouds cool the Earth-atmosphere system on a global basis at TOA by reflecting incoming solar radiation, compensating their warming effect due to the trapping of infrared (IR) radiation. Therefore, even small changes in macrophysical (coverage, structure, altitude) or microphysical properties (droplet size, phase) can have significant effect on climate [*Lohmann and Feichter*, 2005].

The effects of aerosols on the Earth's radiation budget through clouds are indicated as indirect effects, as opposed to their direct effect. The indirect effect that has received the most attention is the increase of cloud droplet concentration and a decrease in cloud droplet size for a cloud with increased CCN and a fixed liquid water content, which increases the reflection of solar radiation [*Twomey*, 1959a, 1977]. This reduction in droplet size reduces the precipitation efficiency, which increases the cloud liquid water content, cloud lifetime [*Albrecht*, 1989] and cloud geometrical and optical thickness [*Pincus and Baker*, 1994]. In addition, absorption by aerosols heats the atmosphere locally, which can result in the evaporation of cloud droplets [*Ackerman et al.*, 2000; *Hansen et al.*, 1997; *Koren et al.*, 2004], and changes in the atmospheric lapse rate and horizontal advection patterns, affecting cloud formation and precipitation on a large scale.

Effects of IN in mixed phase clouds include the growing of ice crystals at the expense of cloud droplets, due to the lower saturation pressure over ice than over water, and the increase of precipitation in supercooled clouds (glaciation indirect effect) [*Lohmann*, 2002], and the increase of convection inside a cloud, due to the release of latent heat when droplets freeze as a result of the presence of IN (thermodynamic effect). The change of release of latent heat high in the atmosphere can have an important effect on the invigoration of updrafts, leading to large hail particles and thunderstorms.

The quantification of aerosol effects on a global scale is difficult due to the many feedback mechanisms and limited measurements available, but excellent overviews can be found in *Haywood and Boucher* [2000] and *Lohmann and Feichter* [2005].

1.3 UV-absorbing aerosol types

Aerosols can be classified in several ways. Aerosols can be classified by production, which can be primary or secondary. Aerosol sources can be used to identify aerosol types, which is important to relate atmospheric aerosol properties to source properties. For example, aerosols and aerosol sources can be of natural origin or anthropogenic, a classification that is often made to estimate the anthropogenic impact on climate via aerosols. However, this classification is not unambiguous, as many anthropogenic activities, like agriculture, forestry, or grazing of cattle, also affect the production and destruction of natural aerosols, which would make these aerosols anthropogenic by definition. Natural aerosols include sea salt particles, soot and carbonaceous aerosols from fires, desert dust, and sulfate and nitrate. Sea salt particles are formed from collapsing ocean water droplets released from breaking waves, which is a wind speed dependent process. The droplets dry, leaving salt particles behind. These small, scattering particles are highly hygroscopic and are efficiently removed by wet deposition. Sulfate and nitrates are mainly formed from oxidation of sulphuric and nitrate acids. The concentration of these scattering particles is very high over industrial areas, indicating the increased role of anthropogenic emissions in the last decades.

The focus in this thesis will be on the optical properties of aerosols. Aerosols can be solely scattering aerosols, which scatter radiation, or absorbing aerosols, which both scatter and absorb radiation. Moreover, the focus will be on UV-absorbing aerosols. These are of interest in space-borne remote sensing applications, because in the UV the surface albedo is low over all surfaces except snow and ice, and retrievals are possible over both land and ocean. Three important aerosol types are UV-absorbing; desert dust aerosols, biomass burning aerosols, and volcanic mineral aerosols. The first two are extensively discussed throughout this thesis and will be introduced here. Volcanic aerosols have a potentially large climatic impact if they are injected into the stratosphere, due to the long lifetime of aerosols in the stratosphere. The lifetime of stratospheric mineral aerosols can be many months, due to the low humidity and absence of efficient wet deposition processes in the stratosphere. The last major volcanic eruption, however, was the eruption of Mt. Pinatubo in 1991 and the last five years the concentration of UV-absorbing stratospheric aerosols has been very low, so volcanic aerosols are not further treated in this thesis.

1.3.1 Desert dust

Desert dust aerosols originate in dry lake beds of deserts and other arid regions, located mainly in the Northern Hemisphere (NH). Wind erosion is the primary production mechanism for desert dust. When the erosivity of the wind, quantified as the wind shear velocity, exceeds the erodibility of the surface, quantified as a threshold shear velocity, aerodynamic forces detach particles from the surface and carry them downwind. The shear velocity of the wind depends on free-stream wind velocity and the roughness of the surface it is passing over. The threshold shear velocity of the surface depends on soil particle size, particle cohesion, and the presence of physical or biological crusts and is modulated by the presence and distribution of nonerodible elements.

The result of the erosion of the surface is creep, saltation (bouncing) or suspension of particles, depending on particle size. Saltation is most important in terms of mass and kinetic energy flux of aeolian sediment transport. Suspension of particles (dust emission) is a byproduct of saltation because saltating particles sandblast the surface and eject fine particles that cannot be detached by purely aerodynamic forces. Typical size ranges for desert dust are 1 – 10 μm. Dust emission often occurs in ”hot spots” arising from surface heterogeneity, and observations of dust storms, particularly in vegetated terrains, often display distinct plumes emanating from relatively small areas which, despite their size, account for the majority of airborne dust [*Okin*, 2005].

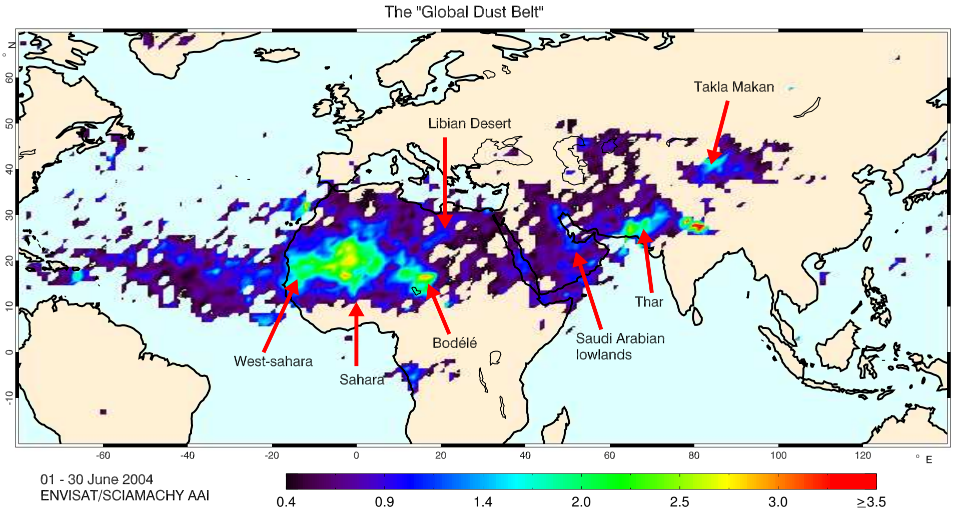

Figure 1.1: *The Global Dust Belt. The one month average of SCIAMACHY AAI (1–30 June 2004) shows the location of the major desert dust sources in the northern hemisphere, indicated with red arrows, and the transport of desert dust over the North Atlantic ocean.*

At the global scale, the Sahara desert is the most important source of mineral aerosols. About several hundred million to one billion tons are estimated to be transported from the Saharan dust region to the tropical North Atlantic Ocean and the Mediterranean Sea every year [*D'Almeida*, 1986; *Prospero et al.*, 1996]. Other major sources are arid regions in the Middle East [*Eckardt and Kuring*, 2005], and the Takla Makan and Gobi deserts in Asia [*Tsunematsu et al.*, 2005; *Kim et al.*, 2005; *Darmenova et al.*, 2005]. The locations of the major dust sources are indicated in Fig. 1.1, using a one month average of the SCIAMACHY AAI (introduced in section 1.6). The sources of desert dust aerosols are located on the continents, mainly at low latitudes, known as the global dust belt [*Prospero et al.*, 2002], although the Southern Hemisphere (SH) arid regions in Australia, southern Africa and southern America also contribute to the total dust loading of the atmosphere [*Tegen and Fung*, 1994].

Dust particles can be lofted to many kilometres in altitude due to the strong vertical mixing in arid areas. The main fraction of the tropospheric desert dust aerosols is usually present in the lowest five kilometres. Saharan dust usually resides in a near-neutrally stable layer of dry air confined between two temperature inversion layers [*Prospero and Carlson*, 1972].

Desert dust particles are typically nonspherical. The composition of mineral aerosols is highly variable. This is caused by the variability in the composition of bed surfaces, spatial and temporal variability of the dust production mechanisms (e.g. selective lifting of the minerals from the bed surface) and spatial and temporal variability of dust composition separation due to physical and chemical processes during dust transport [*Sokolik and Toon*, 1999]. Atmospheric mineral aerosols provide surfaces for reactions, change the concentration of other aerosols in the atmosphere, and affect cloud nucleation and optical properties. African and Saharan dust are effective IN [*Sassen et al.*, 2003; *DeMott et al.*, 2003] and have been shown to reduce precipitation in shallow convective clouds near the source [*Rosenfeld et al.*, 2001]. However, transported Saharan desert dust is largely hydrophobic, while Asian desert dust, on the other hand, is often hydrophilic. This is probably caused by the mixing of Asian dust with soot from industrial sources in China, changing the optical and hygroscopic properties of the particles [*Song-Miao et al.*, 2004; *Kim et al.*, 2005]. Iron in desert dust, transported to downwind terrestrial ecosystems, plays an important role in ocean fertilisation and oceanic CO_2 uptake [*Gao et al.*, 2001; *Bishop et al.*, 2002], affecting the global carbon budget, soil formation and nutrient cycling [*Okin*, 2005].

Mineral aerosols are UV-absorbing, mainly due to the presence of hematite and other iron oxides. The absorption (imaginary index of refraction) of mineral aerosols are largest in the UV and decreases with increasing wavelength [*Patterson et al.*, 1977; *Sinyuk et al.*, 2003; *Torres et al.*, 2005]. Mixing with soot, like for Asian dust, will change the optical properties, but this needs to be resolved.

1.3.2 Smoke

Smoke (biomass burning aerosol) is formed by the combustion of biomass. Natural origins of biomass burning aerosols are due to natural fires, e.g. lighted by lightning. Anthropogenic origins are fires lighted by man, accidentally or to benefit agriculture, and, increasingly, the combustion of fossil fuels. Fires produce a variety of different gases and particulate matter, which can be important exogenous sources of fertilisation for downwind ecosystems [*Keene et al.*, 2006]. Sources of biomass burning aerosols can be anywhere on the continents, but the main sources are regions where biomass is abundant and regions with prolonged dry periods. These include monsoonal tropical forests, monsoonal grass areas and savannas, vegetated desert areas, high latitude coniferous forests and temperate forests.

Smoke properties vary between fires depending on fuel type and moisture, combustion phase, flame temperature, wind conditions, and other variables [*Chambers et al.*, 2005; *Chen et al.*, 2006]. Combustion phases can be smouldering and flaming, although all fires are essentially of a mixed type. Smouldering fires produce different, less and smaller particles than large intense fires that have very high temperatures and are limited in oxygen supply. Grass and shrub fires are smaller in size and intensity, and are mostly consumed by flaming combustion. Forested fires have high particle concentrations and temperatures and typically long burn times, with fire regimes ranging from smouldering to flaming combustion [*Reid et al.*, 2005b].

Fresh smoke particles are typically accumulation mode particles of 0.1 – 0.2 μm in diameter, although larger particles, like giant ash particles of up to a millimetre, can be produced by intense fires [*Reid et al.*, 2005b]. Properties of smoke rapidly changes in the first few hours after creation. Particle sizes increase as the smoke ages. Particles that form at relatively high temperatures are often coated by an (optically) nonabsorbing shell to form an internal mixture [*Martins et al.*, 1998]. The external shell can be formed by gas-to-particle conversion and condensation of volatile compounds. Smoke aerosols are often long-chain aggregates, which interact with water vapour and clouds, collapsing the open structures to form closely packed spherical structures. These packed structures are likely to be externally coated and also have nonabsorbing material in their internal structures. Aged smoke properties are markedly different from fresh smoke properties, but vary more slowly in time. Satellite measurements of

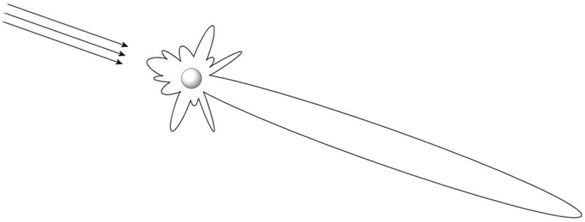

Figure 1.2: *Scattering of light by a particle. Depending on the size and shape of the particle and the wavelength of the light the energy of the light beam is scattered unevenly in all directions.*

smoke yield properties of aged aerosols [*Abel et al.*, 2005].

Biomass smoke particles are important CCN due to their high hygroscopicity, influencing cloud microphysics and precipitation processes. The presence of smoke plumes decreases cloud droplet sizes and increases reflectivity of clouds.

Biomass smoke particles effectively scatter and absorb solar radiation. Black carbon (BC), or soot, is responsible for the short-wave radiation absorption, which depends weakly on wavelength over the near-UV to near-IR spectral region, where the imaginary part of the refractive index of soot is relatively constant [*Bergstrom et al.*, 2002; *Torres et al.*, 2005]. The wavelength dependence of the light absorption is dependent on particle size: smaller particles have a stronger wavelength dependence of light absorption than larger particles. Internally mixed particles composed of an absorbing core surrounded by a nonabsorbing shell, in the same order of size as the particle diameter, in general have a greater absorption efficiency than pure BC particles [*Martins et al.*, 1998]. This is because the nonabsorbing shell increases the total cross-sectional area of the particle and focuses light toward the absorbing core, causing the same amount of BC in the mixed structure to absorb more than pure BC particles.

1.4 Aerosol light scattering and absorption

Scattering results from the interaction of light with matter. A particle in the path of an electromagnetic wave continuously extracts energy from the incident wave and reradiates the energy in all directions (Fig. 1.2). If some of the energy is converted into heat the particle is said to absorb radiation. All the wonderful phenomena that can be observed in the atmosphere, like sunsets, halos, rainbows, glories, etc., are the result of scattering of solar radiation by particles or cloud droplets.

1.4.1 Single scattering

The attenuation of a light beam traversing an extinction medium is expressed by the Beer-Bouguer-Lambert law [e.g. *Van de Hulst*, 1957; *Liou*, 2002],

$$I = I_0 e^{-\tau}, \tag{1.1}$$

where τ is the optical path length of a path of distance s,

$$\tau = \int_0^s k_e \, ds, \tag{1.2}$$

which describes the exponential decrease of an initial monochromatic radiation intensity I_0 along a path s. The extinction by the medium is described by the extinction coefficient k_e, in units of [m^{-1}], which is the sum of scattering and absorption $k_e = k_s + k_a$.

If the extinction medium consists of many scattering and absorbing particles, the extinction coefficient k_e is the product of the extinction cross section C_e of the particles [m^2] and the number density n [m^{-3}],

$$k_e = C_e \cdot n(s). \tag{1.3}$$

The size range of N particles can be described by a distribution function. Many size distribution functions can be used, the most common ones are the power law distribution, the (modified) gamma distribution and the log-normal distribution [cf. *Hansen and Travis*, 1974; *Hovenier et al.*, 2004]. In this thesis log-normal unimodal and weighted log-normal bimodal size distributions are used. The latter is defined as

$$\frac{dN}{dr} = w \cdot \mathrm{L}_f + (1 - w) \cdot \mathrm{L}_c, \tag{1.4}$$

where L_f and L_c are the log-normal distributions of a fine mode part of the particles and a coarse mode part of the particles, respectively. The log-normal distribution is defined as

$$\mathrm{L} = \frac{N}{r\sqrt{2\pi}\ln(v_g)} \exp -\frac{1}{2}\left(\frac{\ln(r) - \ln(r_g)}{\ln(v_g)}\right)^2, \tag{1.5}$$

where r is radius and r_g and v_g are positive constants. The size distributions in this thesis are described using the effective radius r_{eff} and the effective variance v_{eff},

$$\begin{aligned} r_{\mathrm{eff}} &= r_g \exp(5v_g/2), \\ v_{\mathrm{eff}} &= \exp(v_g^2) - 1. \end{aligned} \tag{1.6}$$

For isotropic homogeneous spherical particles the scattering, absorption and extinction cross sections can be found from Lorenz-Mie theory [*Lorenz*, 1890; *Mie*, 1908].

The single scattering albedo ω_0 of a particle is defined as the ratio of its scattering cross section and extinction cross section,

$$\omega_0 = \frac{C_s}{C_e} = \frac{C_s}{C_s + C_a}. \tag{1.7}$$

The single scattering albedo defines the fraction of scattering and absorption of a particle, determined by the refractive index of the particle m, which is an imaginary number $m = m_r + \boldsymbol{i}m_i$. In general, the refractive index is wavelength dependent. A particle or medium which scatters or absorbs wavelength independently is called a gray scatterer or absorber.

The angular distribution of the scattered light is given by the phase function $P(\cos\Theta)$. This is the 11-element of the 4×4 scattering matrix, which transforms a polarised incident

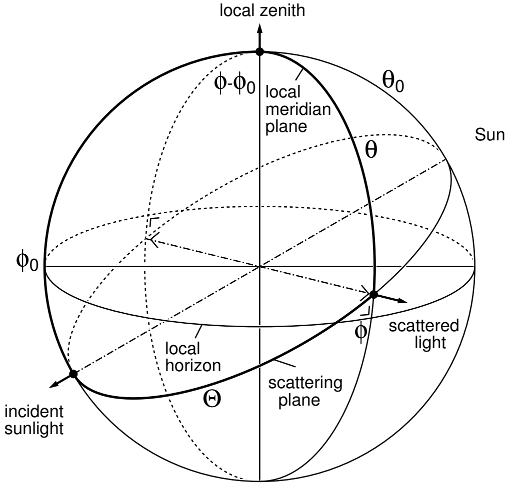

Figure 1.3: *Definitions of the local solar zenith angle θ_0, the local scattering zenith angle θ, the differential azimuth angle $\phi - \phi_0$ and the scattering angle Θ. (Courtesy of L.G. Tilstra.)*

beam of light into a polarised scattered beam of light. The scattering angle Θ relates the direction of incidence (μ_0, ϕ_0) and the direction of scattering (μ, ϕ), see Fig. 1.3, where μ_0 is the cosine of the solar zenith angle θ_0 and μ is the cosine of the scattering zenith angle θ,

$$\cos\Theta = \mu_0\mu + \sqrt{1-\mu_0^2}\,\sqrt{1-\mu^2}\,\cos(\phi - \phi_0). \tag{1.8}$$

The scattering phase functions for several aerosol models and Rayleigh scattering are given in Fig. 1.4a. They were calculated using Mie theory for scattering sulfate particles (S), moderately absorbing carbonaceous particles (C) and strongly absorbing mineral dust particles (D). The average cosine of the scattering angle $\langle\cos(\Theta)\rangle$ is known as the asymmetry or anisotropy parameter g,

$$g = \frac{1}{2}\int_{-1}^{1} \cos\Theta\, P(\cos\Theta)\, d\cos\Theta. \tag{1.9}$$

For molecular scattering the amount of light scattered in the backward and forward direction is equal, $g = 0$, while for aerosols the amount of forward scattered light is greater, $g > 0$, see chapter 2. In some cases the scattering phase function of particles is simulated using a Henyey-Greenstein (HG) phase function [*Henyey and Greenstein*, 1941], defined as

$$\Phi(\cos\Theta) = \frac{1-g^2}{(1+g^2-2g\,\cos\Theta)^{3/2}}, \tag{1.10}$$

so that the asymmetry parameter of the HG phase function is equal to g. In Fig. 1.4b HG functions are plotted for different g.

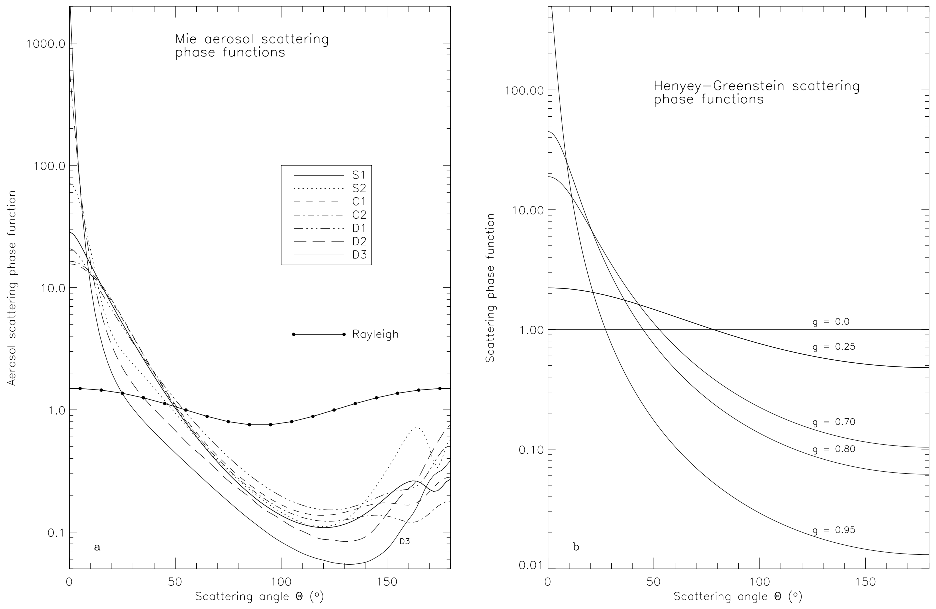

Figure 1.4: *(a) Scattering phase functions (normalised over all scattering angles) for Rayleigh scattering and different Mie aerosol models (S are scattering sulfate aerosols, C are carbonaceous aerosols and D are mineral dust aerosols. The numbers refer to increasing sizes of the aerosols in the models [Torres et al., 1998]). Note the strong forward ($\Theta = 0$) scattering of aerosols, especially for large aerosols. For Rayleigh scattering the amount of light scattered in the backward and forward direction is equal. (b) Single Henyey-Greenstein phase functions.*

1.4.2 Multiple scattering

A light beam travelling through the atmosphere is likely to encounter multiple scatterers. To account for multiple scattering the Doubling-Adding method was used in this thesis. In this method the reflection and transmission for two plane-parallel layers, that are optically thin enough that the single or double scattering approximation is valid, are computed for monochromatic radiation. Then multiple scattering between the layers is obtained by computing the successive reflections between the two layers. If the two layers are identical the result for a homogeneous layer can be obtained by successive doubling of the layers until the desired optical thickness of the layer is reached [*Van de Hulst*, 1980; *Hovenier et al.*, 2004]. The atmosphere is then built by adding different homogeneous layers and computing the successive reflections between the layers. The optical thickness τ of the atmosphere can be found by integrating the extinction coefficient over the vertical height z,

$$\tau = \int_0^\infty k_e(z)dz. \tag{1.11}$$

The Doubling-Adding method used in this thesis accounts for polarisation of light [*De Haan et al.*, 1987].

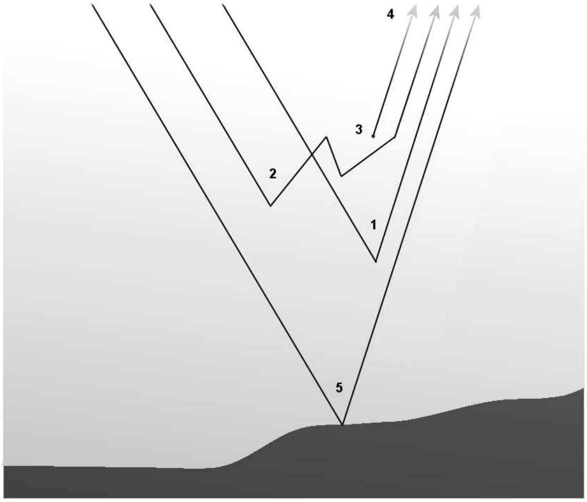

Figure 1.5: *Scattering and absorption processes in the atmosphere (1-4) and at the surface (5): (1) single scattering of the direct solar beam; (2) multiple scattering; (3) emission in the atmosphere; (4) attenuation by extinction; (5) reflection and absorption at the surface.*

1.5 Aerosol remote sensing from space

Aerosol remote sensing can be performed in many ways, using ground-based instruments, air-borne instruments or space-borne instruments. Here, only space remote sensing will be discussed.

Passive satellite instruments measure the reflected radiance of the Sun at TOA. The radiation emerging at TOA, in the direction of a satellite can be attributed to the following processes in the atmosphere: (1) single scattering of the direct solar beam, (2) multiple scattering from all directions, (3) emission from inside the atmosphere and (4) attenuation by extinction. Furthermore, radiation is added by (5) reflection at the surface (see Fig. 1.5). Some instruments are designed to measure Earth's outgoing longwave radiation at TOA (3), but this is of minor importance to aerosol detection and will not be considered here. The processes in the atmosphere that attenuate and eventually scatter the radiation from the Sun toward the satellite instrument are usually simulated using a radiative transfer model, like the doubling-adding model.

Many satellite instruments are used for aerosol properties retrieval, although most were not designed specifically for aerosol retrieval. The amount of aerosol information that can be retrieved with a particular instrument is dependent on the amount of independent pieces of information that can be retrieved simultaneously [*Hasekamp and Landgraf*, 2005]. Early satellite measurements of aerosol properties consisted of reflectance measurements in one channel, e.g. from geostationary satellites like GOES and Meteosat. Infrared Meteosat thermal data is sensitive to the presence of Saharan dust over land. In the presence of dust plumes a decrease of the infrared channel (10.5-12.5 μm) at daytime and an increase at nighttime is

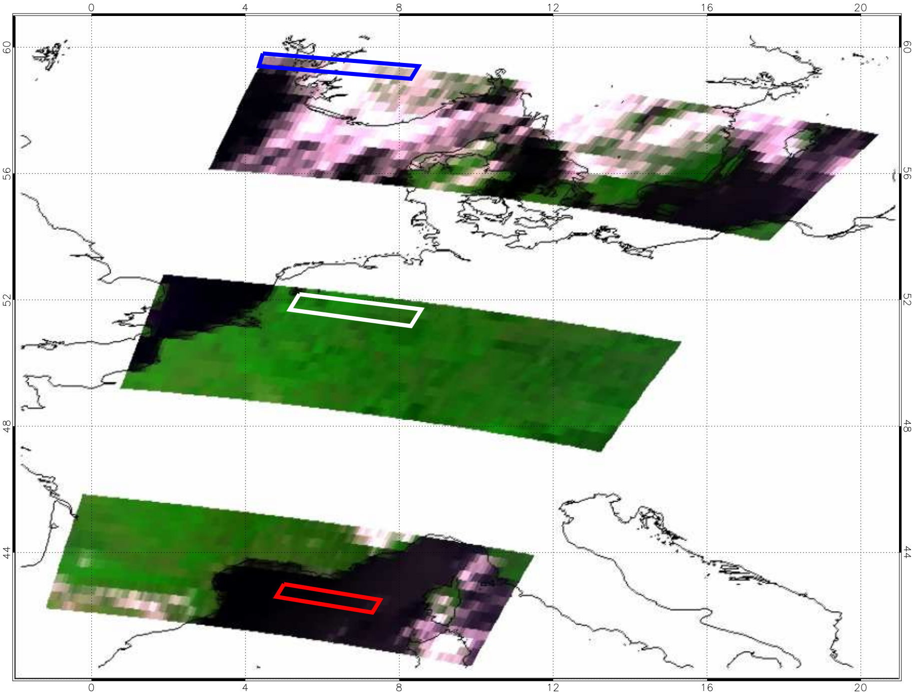

Figure 1.6: *True colour image of SCIAMACHY Polarisation Measurement Devices (PMDs), channel 4, 3 and 2 (RGB), of north-west Europe, showing three subsequent SCIAMACHY nadir states on 29 September 2005. Black pixels indicate sea/ocean scenes, green pixels indicate vegetated scenes and pink/white pixels indicate clouds. The rectangles indicate the selected scenes for which the spectra were determined (see Fig. 1.7).*

observed. Furthermore, in the visible range atmospheric blurring due to the presence of aerosols can be observed [*Tanré and Legrand*, 1991]. Alternatively, two channel measurements were used, e.g. from Advanced Very High Resolution Radiometer (AVHRR) [*Husar et al.*, 1997; *Geogdzhayev et al.*, 2002; *Hauser et al.*, 2005], the first of which was launched in 1978, and Sea-viewing Wide Field-of-view Sensor (SeaWiFS) [*Borde and Verdebout*, 2003], launched in August 1997, both, currently, with a 1.1 km spatial resolution. Algorithms derived only aerosol optical thickness, given a suitable aerosol model based on geographic location [*Tanré et al.*, 1996].

UV measurements were used for the first time with the reprocessing of TOMS data, yielding AAI data since 1978 when the first TOMS instrument was launched [*Hsu et al.*, 1996; *Herman et al.*, 1997; *Torres et al.*, 1998]. This record of almost continuous data is the longest set of space-borne aerosol information. Although the AAI contains aerosol information, it is sensitive to many other parameters. The analysis of the properties of the AAI is one of the topics of this thesis.

Better aerosol retrievals were obtained when instruments with more channels and better

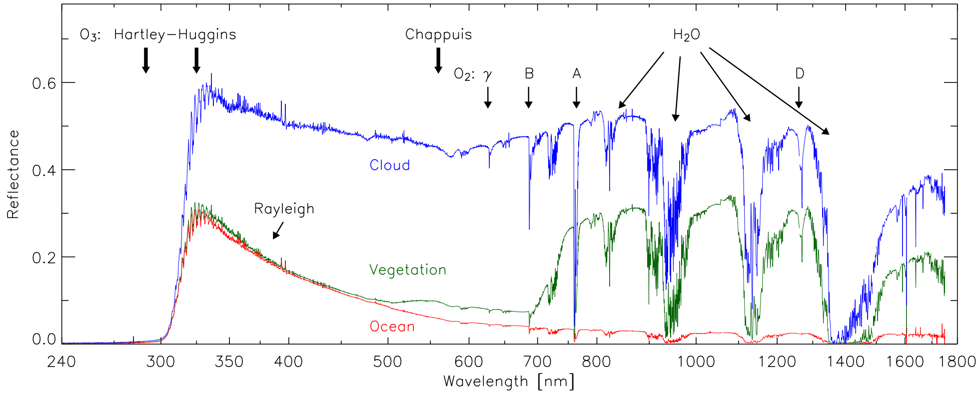

Figure 1.7: *SCIAMACHY reflectance spectra of selected scenes in Fig. 1.6, a cloudless scene over the Mediterranean Sea (red), a cloudless vegetated scene over The Netherlands (green) and a cloudy scene over Scandinavia (blue). Ozone, oxygen and water vapour absorption bands and the strong wavelength dependent decrease of Rayleigh optical thickness in the UV are indicated by arrows.*

on-board calibration became available. One of the main problems using reflectance measurements for aerosol retrievals is the presence of subpixel clouds, but these can be detected using IR channels. Currently the instrument with the most spectral channels and the highest spatial resolution retrieving aerosol information is Moderate Resolution Imaging Spectroradiometer (MODIS), the first of which was launched in December 1999, with a spatial resolution of aerosol retrieval of 0.5 by 0.5 km^2 [*Remer et al.*, 2005; *Kaufman et al.*, 2005; *Remer and Kaufman*, 2006]. Another example of an instrument with a high spatial resolution (0.3 by 0.3 km^2) is Medium Resolution Imaging Spectrometer (MERIS) onboard Environmental Satellite (Envisat). MERIS has 15 spectral channels, although not in the IR. High-resolution aerosol products from MERIS are expected in the near future.

Most instruments using reflectance measurements in one or more channels have different algorithms for retrieval over ocean and land, because the bright surface reflectivity is often difficult to distinguish from aerosol effects. A considerable improvement for this problem was the introduction of multiple viewing angle instruments, like Multiangle Imaging Spectro-Radiometer (MISR) [*Diner et al.*, 2001] and (Advanced) Along-Track Scanning Radiometer ((A)ATSR) [*Veefkind et al.*, 2000]. With these instruments the surface contribution can be specified by viewing the scene from different angles.

Another increase of retrieved aerosol information content can be achieved by measuring polarised light, because the polarisation properties of reflected light are highly sensitive to aerosol microphysics [*Hansen and Travis*, 1974; *Hasekamp and Landgraf*, 2005; *Mishchenko and Travis*, 1997; *Waquet et al.*, 2005]. Aerosol retrievals from Polarization and Directionality of Earth's Reflectances-1 and -2 (POLDER-1 and POLDER-2) polarimeters have been very promising [*Deuzé et al.*, 2000; *Herman et al.*, 2005], but unfortunately both instruments failed after only about eight months. Since December 2004 Polarization & Anisotropy of Reflectances for Atmospheric Sciences coupled with Observations from a Lidar (PARASOL) is part of the A-Train flotilla, a formation of five satellites flying in low polar orbits.

Aerosol retrievals may also be improved by increasing the spectral resolution of the reflectance measurements. Little is known about the aerosol content in (polarised) reflectances at multiple wavelengths. Currently, three space-borne spectrometers are available, GOME, launched in April 1995, SCIAMACHY, launched in March 2002 and Ozone Monitoring Instrument (OMI), launched in July 2004. All three instruments measure Earth's reflectance in the UV and visible at a high (0.2–0.4 nm) spectral resolution, and GOME and SCIAMACHY measure into the near-IR, until 790 nm and 2380 nm, respectively.

GOME

GOME is a spectrometer onboard the Second European Remote Sensing satellite (ERS-2), launched in April 1995 into a sun-synchronous orbit at a mean altitude of about 785 km, with a local equator crossing time of 10:30 AM (local time). Using the maximum swath width of 960 km across track, global coverage can be achieved in three days. The main objectives of GOME were the determination of the global distribution of ozone and several other trace gases, like NO_2 [*Burrows et al.*, 1999]. However, in the eleven years of operation GOME has delivered important information on many more trace gas products, like OClO, volcanic and anthropogenic SO_2, H_2CO from biomass burning, tropospheric BrO and H_2O. Furthermore, the AAI was calculated from GOME data [*Gleason et al.*, 1998; *Torricella et al.*, 1999], from which the global distribution of UV-absorbing aerosols can be studied. In section 2.4 the GOME AAI is described in detail.

Unique to GOME are the measurements of radiance and irradiance at TOA in the UV and visible range from 240 – 790 nm at a spectral resolution of 0.2 to 0.4 nm. This broad spectral range of TOA reflectances are exploited for aerosol retrieval in chapter 3.

SCIAMACHY

SCIAMACHY is a spectrometer onboard Envisat, launched in March 2002 into a sun-synchronous orbit at about 800 km altitude, with an equator crossing-time of 10:00 AM (local time) for the descending node, orbiting the Earth every 100 minutes. SCIAMACHY observes the radiance and solar irradiance in the UV, visible and near-IR wavelength regions (240–2380 nm) at a spectral resolution of 0.2–1.5 nm [*Bovensmann et al.*, 1999]. The radiance is observed in two alternating modes, nadir and limb, yielding data blocks called states (see Fig. 1.6). Using the nadir swath width of approximately 960 km total global coverage is achieved in six days, due to the alternating limb and nadir observations. The trace gases that are being derived from SCIAMACHY measurements include total column O_3, CO, CH_4, CO_2, H_2O, SO_2, NO_2, H_2CO, stratospheric O_3, BrO, NO_2 and mesospheric O_3, besides temperature and pressure, clouds and aerosols. The AAI derived from SCIAMACHY measurements is described in chapter 4.

Figure 1.6 shows an example of a true colour picture using the broad-band Polarisation Measurement Devices (PMDs) of SCIAMACHY, channel 4, 3 and 2 (RGB), to create a relatively high spatial resolution colour image of north-west Europe on 29 September 2005. The reflectance spectra measured by SCIAMACHY, of the scenes indicated by the rectangles, are plotted in Fig. 1.7. SCIAMACHY's spectral reflectance measurements are used in chapter 5 to investigate the spectra of selected aerosol scenes.

1.6 The Absorbing Aerosol Index

The effect of UV-absorbing aerosols on the backscattered radiation field measured by space-based instruments was first studied to reduce the error due to aerosols in ozone retrievals [*Dave*, 1978]. Ozone columns were determined using UV reflectances, one in an ozone sensitive channel, one in a nearby ozone insensitive channel, and separating the spectral contrast in these channels caused by ozone from that caused by all other effects, like Rayleigh and cloud scattering, surface reflection and aerosol absorption and scattering [*Dave and Mateer*, 1967]. This was achieved by predicting the reflectances in the two channels in a clear sky Rayleigh atmosphere bounded from below by a Lambertian surface, which scatters all radiation equally in all directions at all wavelengths, using radiative transfer modelling. If the surface albedo was chosen so that the measured TOA reflectance at the ozone insensitive channel was equal to the clear sky modelled value, the ozone amount could be retrieved in the ozone sensitive channel from the radiative transfer modelling results, assuming that all atmospheric scattering and absorbing effects were taken into account by the (gray) surface reflector. However, this method was unsuccessful when a scene contained broken or thin clouds, sunglint, or UV-absorbing aerosols [*Torres and Barthia*, 1999].

TOMS' indices Halfway the 1990's reprocessed (version 7) TOMS measurements became available, with four channels in ozone insensitive channels (331, 340, 360 and 380 nm), which provided the possibility to study UV-absorbing aerosols. Essentially the same method as described above for ozone was applied to study the effect of aerosol absorption on the spectral contrast. Aerosol absorption lowered the reflectance more strongly at shorter wavelengths compared to that in a Rayleigh atmosphere, even for gray absorbers, due to the strong (λ^{-4}) wavelength dependence of Rayleigh optical thickness in the UV. Scattering effects produce a reversed effect and the reflectance difference at 340 and 380 nm ($R_{340} - R_{380} < 0$) was used to indicate the presence of biomass burning aerosols in South Africa using all 14.5 years of available TOMS data in 1996 [*Hsu et al.*, 1996]. This was the first index describing UV-absorbing aerosols.

The Absorbing Aerosol Index was part of the standard TOMS version 7 data set, in a slightly different form. A residue was defined using

$$r_{340,380} = -100 \cdot {}^{10}\log\left(\frac{R_{340}^{\text{meas}}}{R_{340}^{\text{Ray}}}\right). \tag{1.12}$$

where R_{340}^{Ray} is calculated for a Rayleigh atmosphere, using a surface albedo that is found from the measured reflectance at 380 nm, satisfying $R_{380}^{\text{Ray}}(A_s) = R_{380}^{\text{meas}}$. Due to the minus sign in Eq. 1.12, a positive residue is an indication of the presence of UV-absorbing aerosols, which was called the Absorbing Aerosol Index (AAI), while scattering aerosols produce negative residues and clouds near-zero residues [*Torres et al.*, 1998]. The residue is more sensitive to the reflectance measurements than the pure difference between reflectance measurements,

$$\frac{dR_{\lambda}^{\text{meas}}}{R_{\lambda}^{\text{meas}}} = -\frac{\ln 10}{100} dr_{\lambda,\lambda_0}\,, \tag{1.13}$$

so a 1% difference in $R_{\lambda}^{\text{meas}}$ yields a change in r_{λ,λ_0} of 0.434 [*Torres et al.*, 1998]. The residue is plotted as a function of R_{340}^{meas} and R_{380}^{meas} in Fig. 1.8, using a typical viewing geometry. Values

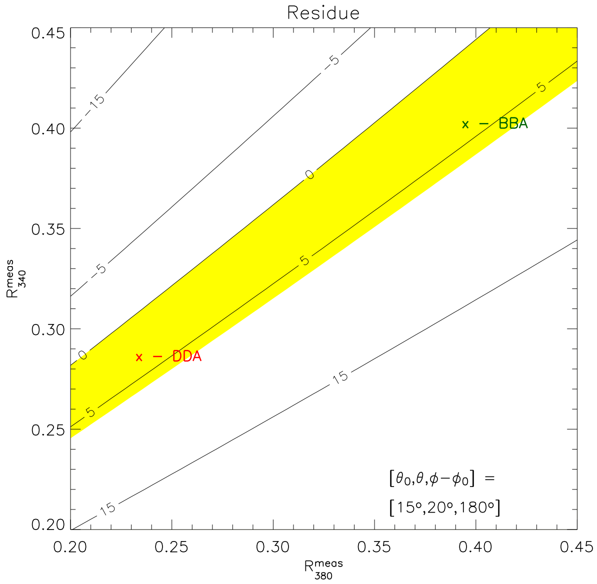

Figure 1.8: *Residue as a function of measured reflectances. The yellow area gives the range of normal AAI values which are indicative for absorbing aerosols. A typical low reflectance case is marked 'DDA' and a typical high reflectance case is marked 'BBA'. Both cases have roughly the same residue.*

of residues that are indicative of absorbing aerosols range from zero to about six, indicated by the yellow area in Fig. 1.8.

Several sensitivity studies showed that the AAI is sensitive to the absorption optical thickness $\tau(1-\omega_0)$ of the aerosol layer, but also to the height of the aerosol layer [*Herman et al.*, 1997; *Torres et al.*, 1998; *Hsu et al.*, 1999b]. This is because the AAI is sensitive to the attenuation of Rayleigh scattered radiation below the aerosol layer, which increases as the aerosol layer height increases. Figure 1.9 illustrates the main sensitivities of the AAI.

Applications of the AAI The sensitivity to aerosol layer height hampers a translation of AAI into aerosol optical thickness and/or aerosol single scattering albedo. However, the availability of TOMS v7 AAI triggered many studies of the distribution of UV-absorbing aerosols.

The long lifetime of 14.5 years of the NIMBUS-7/TOMS instrument, from 1979 to 1993, allowed the space-based recording of the distribution of volcanic ash from two major volcanic eruptions, the El Chicon eruption in April 1982 [*Seftor et al.*, 1997] and the Mt. Pinatubo eruption in June 1991 [*Torres et al.*, 1995]. Volcanic sulfate aerosols have a large climatic impact due to the long lifetime of the aerosols that are injected in the stratosphere.

Smoke was detected over the Amazonian rain forest, in Indonesia during the 1997 El Niño draught [*Duncan et al.*, 2003], Canada [*Spichtinger et al.*, 2001], and Greenland [*Hsu et al.*, 1999a], using the AAI. The unexpected ability of the AAI to detect smoke aerosols over snow and ice in Greenland, which are bright surfaces even in the UV, was attributed to the

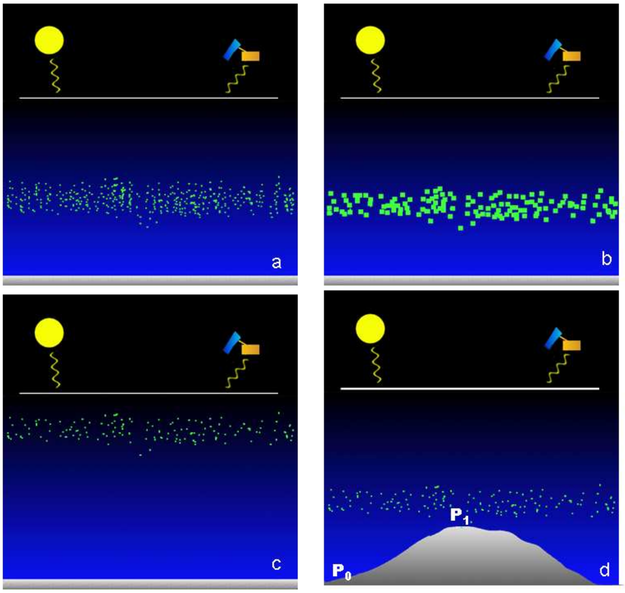

Figure 1.9: *Illustrations of cases with positive residues. The residue is positive when the aerosols absorb radiation that is Rayleigh scattered below the aerosol layer. The residue increases when the aerosol absorption is larger due to (a) more absorbing aerosols (larger optical thickness) or (b) more efficiently absorbing aerosols (smaller single scattering albedo). However, if the aerosols are at a higher altitude (c) the amount of Rayleigh scattered radiation below the layer increases and the AAI becomes larger as well. Conversely, if the 'amount of atmosphere' below the aerosol layer is less than anticipated, e.g. due to the presence of mountains (d), the AAI is also larger.*

Rayleigh multiple scattering reduction by gray aerosols. However, as shown in chapter 5 of this thesis, the wavelength dependence of the aerosol optical thickness (AOT) produces the high AAI in the case of a bright surface. Modelled emissions of smoke and other biomass burning aerosols were improved using AAI observations and modelling [*Zhang et al.*, 2005].

Saharan dust was observed over the North Atlantic ocean [*Chiapello et al.*, 1999; *Colarco et al.*, 2002; *Moulin and Chiapello*, 2004], in the Middle-East [*Alpert and Ganor*, 2001] and in the sub-Sahel [*Pandithurai et al.*, 2001], and Asian dust in China [*Darmenova et al.*, 2005], using the AAI. The major desert dust source regions are located in the Northern Hemisphere (NH), mainly the region from the west coast of North Africa, through the Middle East and China, which were studied in great detail using the AAI [*Prospero et al.*, 2002].

Other applications of the TOMS AAI included assessing UV reduction at the Earth's surface due to absorbing aerosols [*Krotkov et al.*, 1998], studying pyro-cumulonimbus injection of smoke into the stratosphere [*Fromm et al.*, 2005], identifying errors from absorbing aerosols in ozone column amounts from TOMS [*Torres and Barthia*, 1999], and in sea surface temperature from AVHRR measurements [*Diaz et al.*, 2001].

The success of the AAI to measure global aerosol distributions triggered sensitivity studies to refine the methodology of the AAI method. For example, since mineral aerosols have a wavelength dependent effect on the backscattered radiation [*Sinyuk et al.*, 2003], the sensitivity of mineral aerosols on the AAI is different than that of gray aerosols [*Mahowald and Dufresne*, 2004]. Therefore, mineral aerosols can be detected even closer to the surface than initially expected.

Other Aerosol Indices Meanwhile, the TOMS AAI algorithm was applied to data from other instruments, like GOME data in 1995, when no TOMS data was available [*Gleason et al.*, 1998], and June 1997 [*Torricella et al.*, 1999]. In this thesis the derivation of an AAI from both the GOME (chapter 2) and SCIAMACHY (chapter 4) instruments will be described. A residue applied to visible wavelength was derived from MODIS ($r_{412,470}$) and SeaWiFS ($r_{412,490}$) data [*Hsu et al.*, 2004]. In this wavelength range, the spectral dependence of cloud reflectance is flat, due to the little droplet absorption, while desert dust reflectance has a strong spectral dependence here. Therefore, positive residues separate dust plumes from clouds. This positive residue was called the Deep Blue Aerosol Index (DAI). Residues calculated in the entire wavelength range of GOME measurements are treated in chapter 3. An alternative Aerosol Index was derived from POLDER data [*Tanré et al.*, 2001], which should not be confused with the AAI. The POLDER $\mathrm{AI}_{\mathrm{pol}}$ multiplies the AOT at a certain wavelength with the wavelength dependence of the AOT, given by the Ångström parameter α [*Ångström*, 1929], $\mathrm{AI}_{\mathrm{pol}} = \tau_{\mathrm{aer}} \cdot \alpha$. The Ångström parameter is dependent on particle size, large particles have an almost zero α, while the Ångström parameter of small particles is around 1.5 – 2. The $\mathrm{AI}_{\mathrm{pol}}$ worked well to characterise natural and anthropogenic aerosol distributions [*Kapustin et al.*, 2006]. The POLDER measurements are used in chapter 3. However, the $\mathrm{AI}_{\mathrm{pol}}$ is not considered further in this thesis.

Despite the high sensitivity to aerosol layer height the AOT can be retrieved from the AAI [*Torres et al.*, 1998], using predefined aerosol models and assuming aerosol layer height. Using not only the ratio of the reflectance measurements at 340 and 380 nm, but also the absolute value of the measurements, two pieces of information may be retrieved, for example the AOT and the single scattering albedo [*Torres et al.*, 1998]. Sensitivity studies showed errors up to 70% in AOT due to a one kilometre error in aerosol layer height. However, comparisons with AERONET measurements showed retrievals from TOMS AAI within ±30% for AOT and ±0.03 for single scattering albedo for detailed measurements in 2000 [*Torres et al.*, 2005] and long term time series [*Torres et al.*, 2002].

An aerosol model is commonly selected on basis of geographical considerations. Aerosol type can be constant for some regions, but in other regions different types of aerosols can be present at a time [*Herman et al.*, 1997; *Tanré et al.*, 2001; *Torres et al.*, 2002]. However, selection criteria for aerosol types on the basis of direct measurements are not available.

The chapters in this thesis use the work of the above mentioned studies as a starting point. The residue was determined from GOME and SCIAMACHY data, but the spectrometers present more detailed spectral information in the UV, visible and IR. This information was used to identify the processes governing the residue method and an attempt is made to build an aerosol type classification algorithm from spectral reflectances. Detailed investigations of the method and measurements showed new processes of aerosol-cloud interaction and provide an opportunity to refine the quantification of the aerosol indirect effect.

2

Absorbing Aerosol Index – sensitivity analysis, application to GOME and comparison with TOMS

Abstract

The Absorbing Aerosol Index (AAI) was investigated and used to analyse GOME data and compare it to TOMS data. The physical interpretation of the AAI was studied with an extensive theoretical sensitivity analysis. The dependence of the method on a number of atmospheric, surface and aerosol properties was studied using a numerical radiative transfer model. It was found to be sensitive (producing positive values) to absorbing aerosols with wavelength dependent refractive indices and to elevated absorbing aerosols, both with wavelength dependent and wavelength independent (gray) refractive indices. It was found to be insensitive to clouds, while small size scattering aerosols yield negative values. AAIs were calculated from GOME data for the period July 1995 to December 2000 and compared to TOMS AAI data. In a part of this period, July 1995 to October 1996, no TOMS observations were available and the GOME data can be used to supplement the TOMS data set. The GOME AAI corresponds very well with known absorbing aerosol events. It suffers from lower spatial resolution and less frequent temporal coverage as compared to TOMS, but is useful as an independent data source of global aerosol measurements.

M. de Graaf, P. Stammes, O. Torres and R.B.A. Koelemeijer (2005), *JGR 110 (D01201)*, DOI: 10.1029/2004JD005178

2.1 Introduction

The Absorbing Aerosol Index (AAI) indicates the presence of elevated absorbing aerosols in the troposphere. It separates the spectral contrast at two ultraviolet (UV) wavelengths caused by absorbing aerosols from that of other effects, including molecular Rayleigh scattering, surface reflection, gaseous absorption and aerosol and cloud scattering [*Torres et al.*, 1998].

Traditionally, aerosol optical thickness measurements are being made using space-borne sensors operating in the visible and infrared (IR), where multiple scattering in the atmosphere is less important than in the ultraviolet (UV) and inversion calculations are relatively simple. In the visible and near-IR the large surface albedos of many land types make retrieval of aerosols difficult over these regions. With the ongoing development of numerical radiative transfer codes and increasing computational speeds accounting for multiple scattering is no longer a problem, allowing for new techniques of aerosol measurements in the UV. Because the surface albedos of both land and ocean are small in the UV, this wavelength range should be suitable for aerosol detection over land.

The AAI has many names, most notably the residue, the spectral contrast anomaly, the absorbing aerosol index or simply aerosol index. This range of names reflects the ambiguous status of the index; physical interpretation of the index is difficult. We will adopt here the name residue (r) for the result of equation 2.1 in section 2.2.1, which is a quantity derived from measured reflectances. The name AAI is used for the index indicating absorbing aerosols, which is derived from the residue as defined in section 2.3.8.

The residue emerged as an error estimate in the Total Ozone Mapping Spectrometer (TOMS) ozone retrieval algorithm [*Torres et al.*, 1998; *Torres and Barthia*, 1999]. As TOMS instruments have flown, on various platforms, from 1978 to present providing nearly daily global coverage, the TOMS AAI record is the longest aerosol record available and it is used extensively to investigate aerosol impact on climate and study heavy dust, biomass burning and volcanic eruption events [e.g. *Hsu et al.*, 1996; *Herman et al.*, 1997; *Seftor et al.*, 1997; *Chiapello et al.*, 1999; *Pandithurai et al.*, 2001; *Alpert and Ganor*, 2001; *Moulin and Chiapello*, 2004]. However, from May 1993 to June 1996 no TOMS observations were available.

The purpose of this paper is twofold. Firstly, physical interpretation of the absorbing aerosol index is facilitated by presenting an extensive analysis of the main sensitivities of the index, which we feel is missing in the literature. A theoretical basis for the AAI was given by *Torres et al.* [1998], using aerosol models with spectrally independent refractive indices m. The radiance changes for different surface albedos, aerosol refractive indices, aerosol layer height and solar zenith angles were discussed, giving insight in the behaviour of an aerosol laden atmosphere and the resulting residue values therein. The main sensitivities are known: the residue is dependent on aerosol type [*Torres et al.*, 1998] and aerosol single scattering albedo and aerosol layer height [*Herman et al.*, 1997], but to which extent is unclear.

Recently, new evidence showed the incorrectness of the assumption of a spectrally independent refractive index for mineral dust and the implications for the AAI [*Sinyuk et al.*, 2003; *Mahowald and Dufresne*, 2004]. In the present study the sensitivity of the residue for spectrally dependent refractive indices is compared to the residues found for spectrally independent refractive indices. Other sensitivities are studied as well. The definition of the residue is given in section 2.2 and the calculation method used in this paper is presented. In section 2.3 the influence on the residue of aerosol micro- and macrophysical parameters, atmospheric optical, physical and chemical parameters and surface parameters are investigated separately, by means of a radiative transfer model study.

Secondly, the current TOMS AAI record is compared to and supplemented with AAIs derived from five and a half years of Global Ozone Monitoring Experiment (GOME) data. In section 2.4 the GOME data is presented for the period July 1995 - December 2000 and the derived residue and AAI products are described.

2.2 Residue Method

In this section, the definition and derivation of the residue is given and the method of calculation used for the GOME data. The AAI is a quantity derived from the residue. Its definition will be given after the sensitivity study of section 2.3.

2.2.1 Definition of the Residue

The residue r is a wavelength-dependent variable defined as [*Herman et al.*, 1997]

$$r_\lambda = -100 \cdot \left\{ {}^{10}\log(\frac{I_\lambda}{I_{\lambda_0}})^{\text{meas}} - {}^{10}\log(\frac{I_\lambda}{I_{\lambda_0}})^{\text{Ray}} \right\}, \tag{2.1}$$

where I_λ is the radiance at the top of the atmosphere (TOA) at a wavelength λ. The superscript $^{\text{meas}}$ refers to a measured TOA radiance of a real atmosphere with aerosols, as opposed to a calculated TOA radiance for an aerosol-free atmosphere with only Rayleigh scattering and absorption by molecules and surface reflection and absorption. The latter is referred to as $^{\text{Ray}}$.

The reflectance is defined as

$$R = \frac{\pi I}{\mu_0 E_0}, \tag{2.2}$$

where E_0 is the solar irradiance at TOA perpendicular to the direction of the incident sunlight and μ_0 is the cosine of the solar zenith angle θ_0. So $\mu_0 E_0$ is the solar irradiance at TOA incident on a horizontal surface unit. Using equation (2.2) we can replace all quotients of radiances in equation (2.1) with quotients of reflectances.

If the surface albedo A_s for the Rayleigh atmosphere calculation is chosen so that

$$R_{\lambda_0}^{\text{meas}} = R_{\lambda_0}^{\text{Ray}}(A_s), \tag{2.3}$$

where λ_0 is a reference wavelength, equation (2.1) can be reduced to

$$r_\lambda = -100 \cdot {}^{10}\log(\frac{R_\lambda^{\text{meas}}}{R_\lambda^{\text{Ray}}}), \tag{2.4}$$

where R_λ^{Ray} is calculated for surface albedo $A_s(\lambda_0)$, so the surface albedo is assumed to be constant in the range $[\lambda, \lambda_0]$. In this paper we will look at several wavelength pairs λ/λ_0: 340 nm/380 nm, 331 nm/360 nm and 335 nm/380 nm.

2.2.2 Calculation of the Residue

Equation (2.3) involves finding a surface albedo for which the measured reflectance at the reference wavelength is equal to the reflectance of a pure Rayleigh atmosphere with all scattering and absorption effects accounted for in the surface albedo. This inversion process was performed with Lookup Tables (LUTs) of the reflectances, as described below.

On the assumption that the atmosphere is bounded from below by a Lambertian surface, which reflects incident radiation uniformly and unpolarised in all directions, the surface contribution to the reflectance at TOA can be separated from that of the atmosphere [*Chandrasekhar*, 1960]:

$$R(\mu, \mu_0, \phi - \phi_0, A_s) = R_0(\mu, \mu_0, \phi - \phi_0) + \frac{A_s t(\mu) t(\mu_0)}{1 - A_s s^*}. \tag{2.5}$$

The first term, R_0, is the path radiance, which is the atmospheric contribution to the reflectance. The second term is the contribution of the surface with an albedo A_s. t is the total atmospheric transmission, s^* is the spherical albedo of the atmosphere for illumination from below, μ is the cosine of the viewing zenith angle θ and $\phi - \phi_0$ is the relative azimuth angle. The path radiance can be expanded in a Fourier series. For a Rayleigh atmosphere, when $R = R_{\lambda_0}^{Ray}$, the expansion is exact with only three terms in $\phi - \phi_0$, because of the cosine-squared scattering angle dependence:

$$R_0(\mu, \mu_0, \phi - \phi_0) = a_0 + \sum_{i=1}^{2} 2a_i(\mu, \mu_0) \cos i(\phi - \phi_0). \tag{2.6}$$

R_0 is calculated with LUTs of $a_i(\mu, \mu_0)$, $t(\mu)$ and s^* for all wavelengths used. Then the surface albedo A_s in equation (2.3) can be found from

$$A_s = \frac{R - R_0}{t(\mu) t(\mu_0) + s^*(R - R_0)}, \tag{2.7}$$

by replacing R by $R_{\lambda_0}^{meas}$ in equation (2.7). Note that this equation allows negative surface albedos, which occurs for highly absorbing (aerosol) layers.

Lookup tables of a_i, $t(\mu)$ and s^* were prepared as a function of μ and μ_0, surface pressure P_s and ozone column density Ω with the radiative transfer model DAK, described in section 2.3.1. The coefficients were calculated for 42 Gaussian distributed μ and μ_0 points, ozone columns of 167 and 501 DU and surface pressures of 1013, 802, and 554 hPa, as the dependence of the residue on total ozone column was found to be linear, whereas the dependence on surface pressure was non-linear, see section 2.3.6. The surface albedo and reflectance were found by interpolation between these points. Interpolation between ground pressure points was performed with a second order polynomial, all other interpolations were linear.

2.3 Residue Sensitivities

The effects of several aerosol parameters on the residue were studied, as well as the effect of polarisation, clouds and atmospheric constituents, using the radiative transfer model DAK. Thereto the measured reflectances ($R_\lambda / R_{\lambda_0}$) were replaced by simulated reflectances. The 340 nm/380 nm pair was chosen as the default pair.

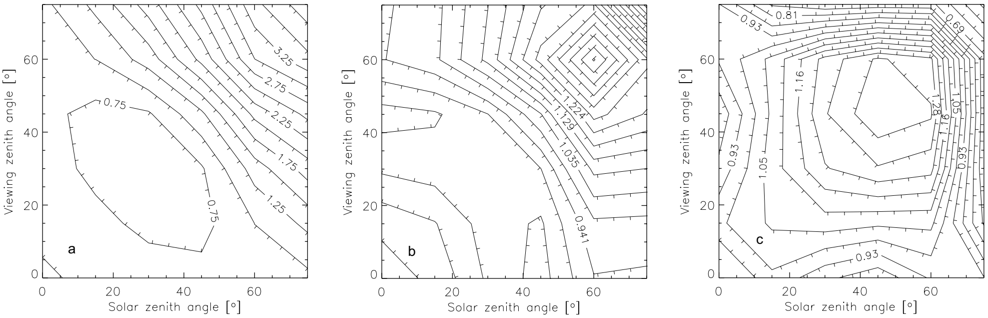

Figure 2.1: *The residue for varying geometries. The standard atmosphere parameters were adopted, with an absorbing ($\omega_0 = 0.9$) aerosol layer between 3 and 4 km, with optical thickness $\tau = 1.0$ and asymmetry parameter $g = 0.7$, over a dark surface ($A_s = 0.05$). (a) Relative azimuth angle ($\phi - \phi_0$) is 0°. (b) Relative azimuth angle is 90°. (c) Relative azimuth angle is 180°.*

2.3.1 Radiative Transfer Model DAK

The Rayleigh atmosphere reflectances and the LUT coefficients were calculated with the Doubling-Adding KNMI (DAK) radiative transfer model [*Stammes*, 2001]. This model computes the monochromatic reflectance and transmittance in a plane-parallel atmosphere including polarisation, using the polarised doubling-adding method [*De Haan et al.*, 1987]. This method calculates the polarised internal radiation field of the atmosphere in an arbitrary number of layers, each of which can have Rayleigh scattering, gas absorption, and aerosol and cloud particle scattering and absorption.

2.3.2 Standard Atmosphere, Geometry and Definition of Aerosol Models

For the atmospheric gas and temperature profile the standard Mid-Latitude Summer (MLS) atmosphere [*Anderson et al.*, 1986] was adopted throughout all calculations. The standard ground pressure was 1013 hPa, the standard ozone column was 334 DU. Linear polarisation was taken into account. A surface albedo of 0.05 was used to simulate dark surfaces and 0.6 to simulate bright surfaces. An aerosol layer could be introduced to simulate aerosol effects. The default altitude of the bottom of this one kilometre thick layer was three kilometres.

Two different types of phase functions were used to simulate the aerosols: the Henyey-Greenstein (HG) function and Mie phase functions. The HG phase function is defined as [*Henyey and Greenstein*, 1941]

$$\Phi(\cos\Theta) = \frac{1 - g^2}{(1 + g^2 - 2g\cos\Theta)^{3/2}}. \tag{2.8}$$

Here Θ is the scattering angle and $g = <\cos\Theta>$ is the asymmetry parameter. The asymmetry parameter is a measure for the amount of forward scattered radiation by aerosols; the greater g, the greater the amount of radiation scattered in the forward direction. For Rayleigh scattering the amount of radiation in the forward direction is equal to the amount of backward scattering, so g is zero. The default value for the asymmetry parameter chosen for HG aerosol was $g = 0.7$, representing moderately forward scattering aerosols. The analytic HG function can be used to separate the effects of the single scattering albedo and the asymmetry parameter.

Mie aerosol phase functions were used to model more realistic aerosols. In Mie calculations the complex refractive index m needs to be changed to vary the single scattering albedo, which also affects the asymmetry parameter. This introduces spectral variations in these parameters, which affect the residue calculations. Three types of aerosols were used, a carbonaceous aerosol model (C2), a small mode dust aerosol model (D1a) and a large mode dust aerosol model (D3). C2 is a smoke model with wavelength independent refractive index defined in *Torres et al.* [1998], D1a is the fine dust model introduced in *Torres et al.* [2002], with the updated imaginary part of the refractive index of *Sinyuk et al.* [2003]. D3 is the large mode dust aerosol model as defined by *Torres et al.* [1998], also with the updated imaginary part of the refractive index of *Sinyuk et al.* [2003]. In Table 2.1 the values of the parameters of the different aerosol models used in this study are summarised. The size distribution of the Mie aerosols was assumed to be log-normal.

The default viewing zenith angle θ in all sensitivity runs was zero (nadir view) and the default solar zenith angles θ_0 were 0°, 15°, 30°, 45° (and 60°). The values of the residue increase quickly for solar zenith angles θ_0 and viewing zenith angles θ larger than 60°, see Figure 2.1a-c. The relative azimuth angle $(\phi - \phi_0)$ is 0°, 90° and 180° in these figures, respectively. Because the radiative transfer code is plane parallel and the residue is not accurate for large solar zenith and viewing zenith angles, the zenith angles considered in the sensitivity runs were limited to $\leq 60°$. The radiative transfer results are symmetric, so viewing zenith angle and solar zenith angle can be interchanged which is reflected in the symmetry of Figure 2.1. For a viewing zenith angle of 30° the residue varies by about 42% between a solar zenith angle of 0° and 60° when the azimuth angle is zero. For an azimuth angle of 90° this variation is about 10 % and for an azimuth angle of 180° it is about 20 %. The GOME viewing zenith angles are always less than about 30°.

Table 2.1: *Parameters for the aerosol models used in this study.*

	λ	C2	D1a	D3	HG[*]
r_g		0.14	0.12	0.50	–
ν_g		1.45	2.20	2.20	–
Re(m)		1.55	1.55	1.55	–
im(m)	340	0.04	0.006	0.006	–
	380	0.04	0.0042	0.0042	–
ω_0	340	0.82	0.90	0.75	0.90
	380	0.83	0.93	0.81	0.90
g	340	0.73	0.70	0.83	0.70
	380	0.73	0.69	0.80	0.70
τ	340	1.00	1.00	1.00	1.00
	380	1.04	1.01	1.01	1.00

[*] Default values. If other values are used, it will be indicated.

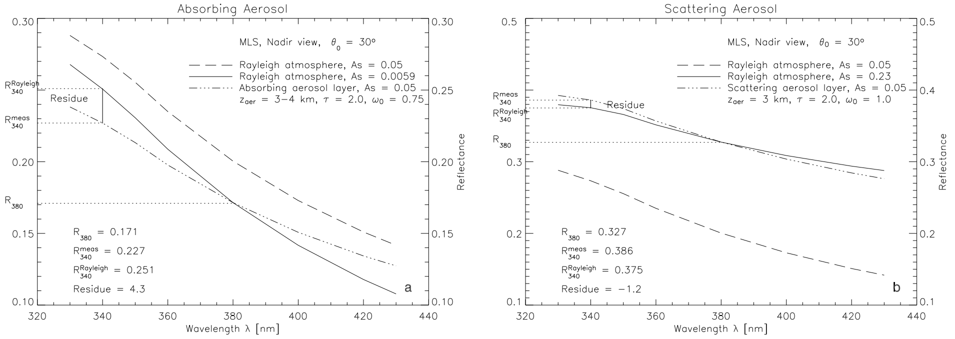

Figure 2.2: *340 nm/380 nm residue calculation in an atmosphere with (a) absorbing aerosols and (b) scattering aerosols. Solar zenith angle θ_0 is 30°, viewing zenith angle θ is 0°. Aerosols are present between 3 and 4 km, with optical thickness τ is 2.0, the aerosol single scattering albedo ω_0 is 0.75 for absorbing aerosols (a) and 1.0 for scattering aerosols (b). The phase function of the aerosols is modelled with a Henyey-Greenstein function with an asymmetry parameter of 0.7. See text for explanation of the plots.*

2.3.3 Absorbing Versus Scattering Aerosols

The calculation of the residue is visualised for an atmosphere with absorbing aerosols and one with scattering aerosols (Figure 2.2), simulated with the DAK model. To produce significantly large residues with HG aerosols, the optical thickness of the aerosol layers is 2.0 and the absorbing aerosols have a single scattering albedo of 0.75 (highly absorbing); the scattering aerosols have a single scattering albedo of 1.0 (non-absorbing).

Consider the spectral dependence of the TOA reflectance in a Rayleigh atmosphere with no aerosols present and a surface albedo of 0.05 (dashed line in Figure 2.2a and b). The reflectance of an atmosphere with an absorbing aerosol layer between 3 and 4 km is decreased for all wavelengths due to the absorption by the aerosols (dashed-dotted line in Figure 2.2a). This aerosol atmosphere is approximated by a pure Rayleigh atmosphere with a different, but wavelength independent surface albedo (solid line in Figure 2.2a). Using the 'measured' reflectance value at λ_0 = 380 nm to fix the Rayleigh case, a surface albedo A_s of 0.0059 is found. Apparently, according to Figure 2.2a, a wavelength independent surface albedo does not produce a good approximation for all wavelengths for the absorbing aerosol case.

The slope of the absorbing aerosol curve (dashed-dotted line in figure 2.2a) is decreased compared to the slope of the Rayleigh curve (dashed line in figure 2.2a), even if the refractive index of the aerosols is wavelength independent, because suppression of Rayleigh scattering by the absorbing aerosols is stronger with decreasing wavelength, due to the higher Rayleigh optical thickness of the atmosphere at shorter wavelength ($\tau_{Ray} \propto \lambda^{-4}$). The slope of the Rayleigh curve is increased for decreasing surface reflection (solid line compared to the dashed line in figure 2.2a), because the subtracted contribution of the surface was spectrally flat. This is the essence of the residue method which is a measure of the deviation between the Rayleigh reflectance curve and the aerosol reflectance curve at a wavelength other than 380 nm. (The case shown here yields a residue r of 4.3 at 340 nm.)

Now consider a case with scattering aerosols (Figure 2.2b). The reflectance with the

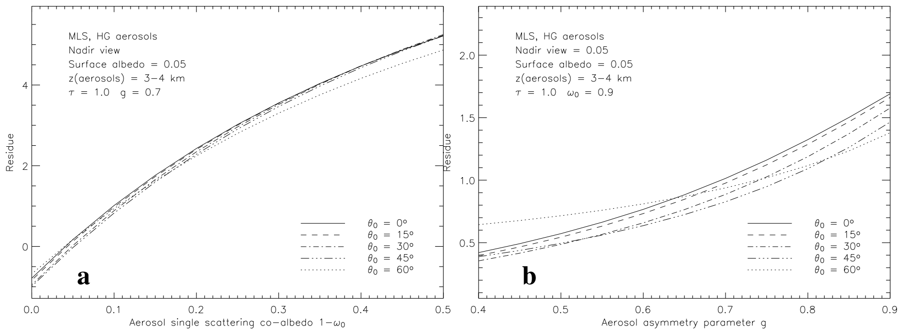

Figure 2.3: *HG aerosols: (a) Dependence of the residue on aerosol single scattering co-albedo* $(1-\omega_0)$*. (b) Dependence of the residue on aerosol asymmetry parameter* g.

aerosol layer added (dashed-dotted line) is now larger than the Rayleigh reflectance (dashed line), giving rise to a higher equivalent surface albedo of 0.23. The Rayleigh reflectance curve for this surface albedo (solid line) matches the aerosol reflectance curve much better, leading to a smaller absolute residue. The Rayleigh reflectance curve has become much flatter, because the contribution of the surface to the reflectance, which is spectrally flat, has increased. Therefore, in the case of scattering aerosols the spectral dependence of the residue is opposite to the one of absorbing aerosols, yielding a negative value (in the case shown here the residue is -1.2 at 340 nm).

2.3.4 Sensitivity of the Residue for HG Aerosol

First the Henyey-Greenstein aerosol model was used in the sensitivity studies. This way the asymmetry parameter and single scattering albedo can be kept spectrally independent.

Aerosol single scattering albedo The residue decreases with increasing aerosol single scattering albedo ω_0 (Figure 2.3a shows the dependence of the residue on aerosol single scattering co-albedo, $1-\omega_0$). Because aerosols with a lower single scattering albedo absorb the radiation coming from below the aerosol layer more effectively than aerosols with higher single scattering albedo, a lower aerosol single scattering albedo yields a higher residue. HG aerosols with single scattering albedo larger than about 0.95 produce zero or negative residues. This sensitivity increases when aerosol models are used which produce a spectrally dependent single scattering albedo, even if this dependence is small. This will be shown below.

Asymmetry parameter Aerosols scatter mainly in the forward direction thus having positive g values, in the range of $g = 0.40 - 0.85$ [*Dubovik et al.*, 2002a; *IPCC*, 2001]. In this range the residue is raised for stronger forward scattering (Figure 2.3b). For higher g the effect of scattering is reduced compared to the effect of absorption, leading to higher residues. Also, as the amount of forward scattered radiation increases, more radiation reaches the surface where absorption takes place yielding a higher residue. This was confirmed in a run with

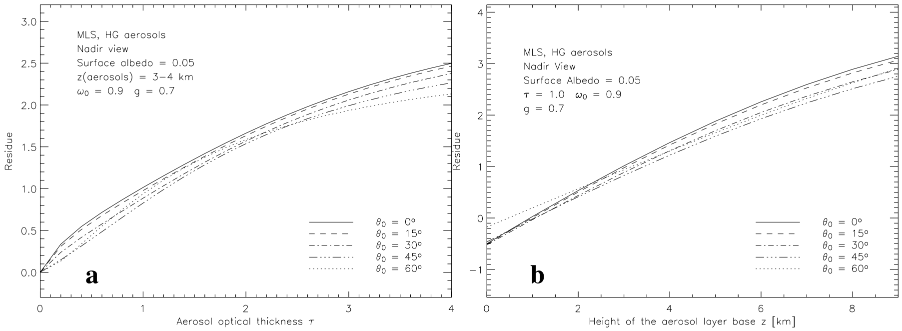

Figure 2.4: *HG aerosols: (a) Dependence of the residue on aerosol optical thickness τ. (b) Dependence of the residue on altitude of the aerosol layer z.*

high surface albedo (0.6), where the increase of residue with increasing g was much less than for a low surface albedo (0.05).

Aerosol optical thickness The residue increases with increasing optical thickness τ (Figure 2.4a). The residue is zero for zero optical thickness by definition. As the optical thickness increases Rayleigh scattering is suppressed and more radiation is absorbed. Therefore less radiation will emerge at TOA and the deviation from the clear sky radiation increases, yielding a higher residue. This is the basis for the detection of absorbing aerosols.

A linear increase of residue with optical thickness with a slope proportional to the single-scattering albedo was also found by *Torres et al.* [1998] and *Herman et al.* [1997].

Aerosol layer altitude The residue is highly dependent on the altitude z of the aerosol layer (Figure 2.4b; the value on the x-axis in this figure refers to the base of the one kilometre thick aerosol layer). The dependence is nearly linear in height, as was found by *Torres et al.* [1998] and *Herman et al.* [1997].

Absorbing aerosols mainly interact with Rayleigh scattered radiation coming from below the aerosol layer. The higher the aerosol layer, the greater the amount of affected Rayleigh scattered radiation, increasing the residue. This means that the residue method is especially suited for detection of elevated tropospheric aerosols and stratospheric aerosols.

2.3.5 Sensitivity of the Residue for Mie Aerosol

Data on aerosol properties suggest that the refractive index of dust aerosol is strongly wavelength dependent in the UV [*Patterson et al.*, 1977; *Sinyuk et al.*, 2003]. This has implications for the residue, as will be shown below with the Mie aerosol models, in which this wavelength dependence is taken into account.

Aerosol optical thickness Like with HG aerosol, the residue increases with aerosol optical thickness (Figure 2.5a). The increase is larger for larger aerosols, because the single scat-

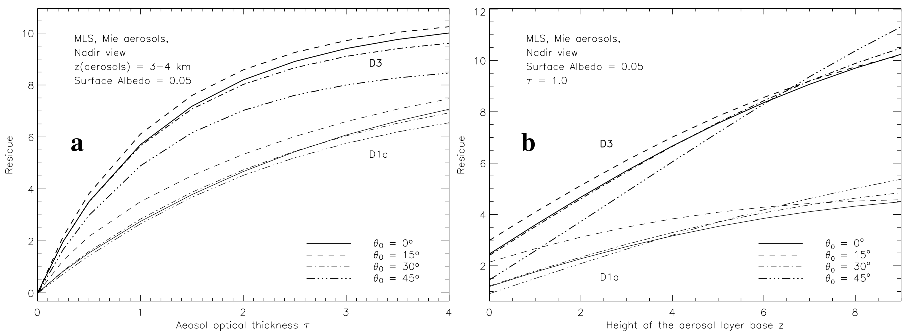

Figure 2.5: *Mie aerosols: (a) Dependence of the residue on aerosol optical thickness τ. (b) Dependence of the residue on altitude of the aerosol layer z.*

tering albedo is smaller (see Table 2.1). The residue is also much larger for aerosols with a wavelength dependent refractive index than for gray aerosols (cf. Figure 2.4a and 2.5a); although the D1a aerosols have almost the same characteristics as the HG aerosols, they produce a much stronger residue increase for increasing aerosol optical thickness than the HG aerosols.

Aerosol layer altitude The residue increases linearly with aerosol layer altitude, like it did for HG aerosol (cf. Figure 2.4b and 2.5b). The slope is proportional to the aerosol single scattering co-albedo, as was found in previous studies [*Herman et al.*, 1997; *Torres et al.*, 1998]. But there is an off-set for aerosols with a wavelength dependent refractive index: using gray aerosols the residue is positive only for aerosol higher than about one to two kilometres in altitude, whereas non-gray absorbing aerosols can be detected even very close to the surface.

This result is consistent with the study of *Mahowald and Dufresne* [2004], who found a stronger residue signal over mineral aerosol sources when gray dust aerosol models were replaced by aerosol models with wavelength dependent refractive indices. This implied the detection of non-gray aerosols closer to the surface, and thus closer to the source, than previously assumed.

2.3.6 Sensitivity of the Residue to Atmospheric and Surface Parameters

Surface albedo Increasing the surface albedo has two competing effects. Firstly, it will increase the role of absorption by the aerosol layer compared to that of the surface. The reason is that below the aerosol layer radiation is bounced back and forth between the surface and the aerosol layer before escaping to space. Absorption takes place each time both at the surface and in the aerosol layer. When the surface albedo is raised, the relative importance of the absorption by aerosols is increased, amplifying the effect of the absorption characteristics of the aerosol layer. This can be spectrally flat, producing no effect on the residue with increasing surface reflection, or wavelength dependent, increasing the residue with increasing surface reflection.

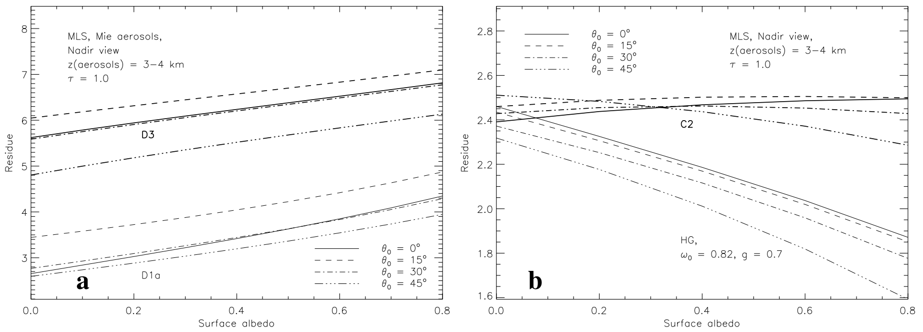

Figure 2.6: *Dependence of the residue on surface albedo for nadir view and solar zenith angles between* 0° *and* 45°. *(a) Atmosphere with Mie aerosols type D1a (normal lines) and D3 (bold lines). (b) Atmosphere with Mie aerosols type C2 (bold lines) and HG aerosols with C2 characteristics:* τ*=1.0,* ω_0*=0.82, g=0.7. (normal lines).*

Secondly, increasing the surface albedo increases the amount of directly reflected radiation emerging at the top of the atmosphere, which results in itself in a zero residue. This will reduce the effect of an aerosol layer and lower the residue for increasing surface reflection.

For aerosols of type D1a and D3, with strongly wavelength dependent single scattering albedo, the first effect is most important. So the residue increases for increasing surface reflection (Figure 2.6a).

For HG aerosols, with wavelength independent single scattering albedo, the first effect results in a constant residue for increasing surface albedo, but the second effect reduces the residue (Figure 2.6b). This is also true for a thin aerosol (gray or non-gray) layer; the presence of such a layer will only be felt when the amount of directly reflected radiation by the surface is small. On the other hand, the residue of a very thick layer of gray aerosols is constant with increasing surface albedo (not shown).

For smoke aerosols, like the C2 model with a weakly wavelength dependent single scattering albedo, the two effects balance each other and the residue does not change much with increasing surface albedo (Figure 2.6b).

The above result for gray absorbers can also be found in *Torres et al.* [1998], where the residue versus aerosol optical thickness was modelled using gray absorbing and scattering aerosols over a dark ($A_s = 0.05$) and a bright surface ($A_s = 0.6$). Using a bright surface instead of a dark surface hardly changed the residue for the absorbing aerosols [*Torres et al.*, 1998, Figure 5]. The above result for the non-gray aerosols seems to be confirmed by observations. TOMS AAI values are larger over underlying clouds, which serve as a bright surface. Smoke aerosols have been observed over both dark surfaces (e.g. biomass burning aerosols over tropical forests in South America [*Gleason et al.*, 1998]) and over bright surfaces (e.g. biomass burning aerosols over snow and ice in Greenland [*Hsu et al.*, 1999a]).

Clouds The effect of clouds on the residue is comparable to the effect of a high surface albedo when the aerosols overlie the cloud. But when the cloud overlies the aerosols the residue is completely determined by the cloud characteristics. This is illustrated in Fig-

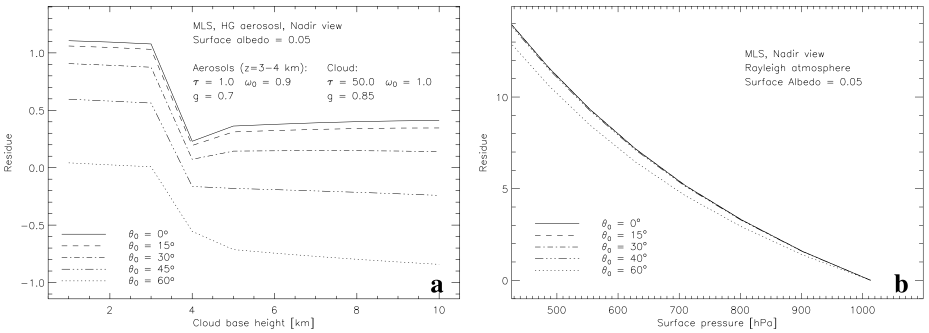

Figure 2.7: *(a) Dependence of the residue on cloud base height, with an aerosol layer between 3 and 4 km altitude. The cloud has optical thickness* $\tau = 50.0$ *and scattering particles with* $\omega_0 = 1.0$ *and* $g = 0.85$*. The base of the 1 km thick cloud was varied between 0 and 10 km in steps of 1 km. (b) Dependence of the residue on surface pressure. Rayleigh atmosphere with MLS profile, nadir view, solar zenith angles vary between 0° and 60°.*

ure 2.7a with HG aerosols (the effect for Mie aerosols can be inferred from Figure 2.6). In Figure 2.7a a cloud was present at different altitudes in an atmosphere with an absorbing HG aerosol layer at an altitude of 3 – 4 km. The cloud is modelled as scattering HG aerosols characterised by a high optical thickness of $\tau = 50$, an asymmetry parameter $g = 0.85$ and a single scattering albedo $\omega_0 = 1.0$. The vertical extent of the cloud is 1 km.

When the cloud is present under the aerosol layer (left side of Figure 2.7a) the residue is the same as for an aerosol layer over a bright surface. The cloud reflects almost all light incident on it, so effectively it becomes the new surface. As the cloud base is raised from 0 to 3 km the residue is slightly reduced due to a decrease in the amount of intercepted radiation by the aerosol layer (the distance between the cloud and the aerosol layer is reduced). Then there is a transition to a new situation when the cloud base is between 3 and 4 km and coincides with the aerosol layer. The residue drops by about 0.9. When the cloud base is raised even further the residue stays almost constant. The cloud intercepts almost all incident radiation and acts as an opaque 'roof' over the aerosol layer; consequently the residue is almost entirely determined by the cloud characteristics. Cloud droplets are in fact scattering aerosols and produce zero or negative residues, depending on the solar zenith angle. This means that the residue method will not be affected very much by low clouds, but high clouds will certainly obscure absorbing aerosols layers.

Ozone absorption A linear relationship between residue and ozone was found by scaling the total ozone column Ω (not shown). The reduction of the TOA radiance due to ozone absorption is, to first order, equal to $\exp(-\tau_{O_3}M)$, where τ_{O_3} is the optical thickness of the ozone column and M is the geometrical airmass factor, $M = 1/\mu_0 + 1/\mu$. Since τ_{O_3} is about 0.01 at 340 nm, the exponential can be approximated by $1 - \tau_{O_3}$.

The dependence of the residue on Ω is limited: if Ω is increased from 100 to 500 DU, the 340 nm/380 nm residue increases by 1, for the 335 nm/380 nm residue the increase is twice as large, but still linear. Therefore the ozone contribution in a Rayleigh atmosphere can be corrected for by linear interpolation. The LUTs include this dependence on Ω (see section 2.2.2).

Regarding the interaction of the absorption processes by ozone and aerosols, it has been shown that particle absorption effects introduce errors in the TOMS total ozone retrieval process, and a correction method making use of AAI has been developed [*Torres and Barthia*, 1999].

Surface pressure The residue is strongly dependent on surface pressure (Figure 2.7b). The surface pressure was lowered by removing the lower part of a Rayleigh atmosphere, which also simulates the effect of topography. In this way an apparent residue is introduced, as a result of the reduced multiple scattering due to the lower amount of Rayleigh scatterers in the atmosphere. This effect is wavelength dependent, with more multiple scattering at lower wavelengths, yielding a residue. The dependence is not linear (Figure 2.7b), therefore the surface pressure is accounted for by a second order polynomial interpolation in the residue calculations (see section 2.2.2).

2.3.7 Sensitivity of the Residue to Other Optical Parameters

Wavelength The wavelength pair (λ, λ_0) in equation (2.1) determines the absolute value of the residue. In the next sections residues from various satellite instruments will be presented. Most of these instruments use different wavelength pairs (Table 2.2); therefore the effect of varying the wavelengths was investigated.

Firstly, the 340 nm/380 nm residue, as used for the first three TOMS instruments, was compared to the 335 nm/380 nm residue, used for GOME, for varying geometries, surface reflectances, aerosol characteristics and aerosol layer heights, 83160 configurations in total. The residue is increased by about 10 % when the radiance at 335 nm is used instead of the radiance at 340 nm for all cases (Figure 2.8a). This is expected for a wavelength pair lying farther apart; at 335 nm multiple Rayleigh scattering is more important, increasing the optical path through the absorbing aerosol layer and increasing the chance of absorption. It can also be seen from Figure 2.2a.

Secondly, the 331 nm/360 nm residue, used for the latest TOMS instrument, was compared to the 335 nm/380 nm residue (Figure 2.8b). The 331 nm/360 nm residues are about 35 % smaller than the 335 nm/380 nm residues. The relationship now becomes non-linear because of the use of different reference wavelengths λ_0. The second, smaller branch in Figure 2.8b is caused by highly absorbing aerosols (ω_0 = 0.6 – 0.7) over a dark surface

Table 2.2: *Wavelengths used to calculate a residue from various UV satellite instruments.*

Instrument	Platform	period	λ/nm	λ_0/nm
TOMS	Nimbus-7	1978-1993	340	380
TOMS	METEOR-3	1991-1994	340	380
TOMS	ADEOS	1996-1997	340	380
TOMS	Earth Probe	1996-present	331	360
GOME	ERS–2	1995-present	335	380

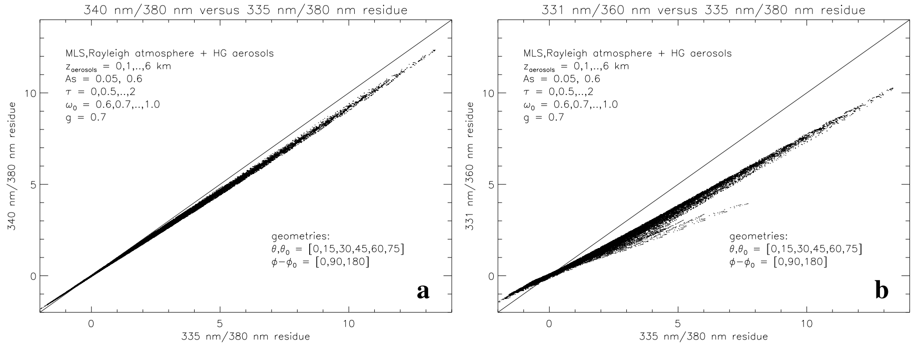

Figure 2.8: *(a) Scatter plot of residues calculated for* λ = 340 *nm versus* λ = 335 *nm* (λ_0 = 380 *nm in both cases). (b) Scatter plot of residues calculated for* λ = 331 *nm and* λ_0 = 360 *nm versus residues calculated for* λ = 335 *nm and* λ_0 = 380 *nm. Residues are determined at all geometries with* θ_0 *and* θ *= [0°, 15°, 30°, 45°, 60° and 75°],* $\phi - \phi_0$ *= [0°, 90° and 180°]. A 1 km thick aerosol layer was present between 0 and 6 km, in steps of 1 km, the aerosol optical thickness was varied between 0 and 2, in steps of 0.2, the single scattering albedo of the aerosol was varied between 0.6 and 1, in steps of 0.1. The surface albedo was 0.05 or 0.6.*

(A_s = 0.05). For these points large negative surface albedos are needed for the equivalent Rayleigh curves. This causes non-physical effects to play a role in the calculations and breaks down the linearity. Because of the larger Rayleigh optical thickness at 360 nm than at 380 nm this effect is greater for the 331 nm/360 nm residue than for the 335 nm/380 nm residue.

The difference between the 331 nm/360 nm and 340 nm/380 nm residues was checked too, and showed a similar pattern as shown in Figure 2.8b, but the mean difference was now 25 %, as expected.

Polarisation Inclusion of polarisation is essential in Rayleigh multiple scattering calculations in the UV. When (linear) polarisation was not accounted for in the LUTs calculations, errors in the reflectances yielded residues as large as 4 to 5 in pure Rayleigh atmospheres (where residues need to be zero by definition).

2.3.8 Conclusion; Defining the Absorbing Aerosol Index

The above sensitivity study shows that there are at least two possibilities to create a positive residue. Firstly, an absorbing aerosol layer can absorb Rayleigh scattered radiation from below the layer. Because the Rayleigh optical thickness is strongly wavelength dependent this creates a difference in the reflectance at two UV wavelengths relative to that of a Rayleigh atmosphere, even with gray absorbers. When the absorbing ability of the layer increases more radiation is absorbed and the deviation increases, increasing the residue. The same is true when the amount of atmosphere under the absorbing layer increases.

Secondly, the aerosol absorption itself can be wavelength dependent, creating a spectral difference in the TOA reflected radiation. This will also create a positive residue if the absorption at the shorter wavelength is stronger, even when the aerosol layer is close to the surface. When the spectral absorption difference increases the residue will increase, meaning that different aerosol types produce different residues under the same circumstances.

For an atmosphere which is dominated by scattering (either by particles, molecules, the surface or clouds) the reflectance will not deviate much from the reflectance of a Rayleigh atmosphere with an adjusted surface albedo, yielding zero or small negative residues.

Therefore the AAI is defined only when a positive residue is found, which excludes clouds and scattering aerosols. The calculation often involves using negative surface albedos and its absolute value has no unique interpretation, but high values of the AAI indicates the presence of absorbing aerosol layers, both over dark and bright surfaces. There have been some efforts of translating the AAI into physical meaningful parameters [*Gleason et al.*, 1998; *Hsu et al.*, 1999a], but we prefer to present the AAI itself rather than a derived product, because the interpretation of the AAI is still developing.

The next sections show that the AAI corresponds well to occurrences of biomass burning and dust events, which are major sources of absorbing aerosols.

2.4 AAI from GOME and TOMS

AAIs were retrieved from Global Ozone Monitoring Experiment (GOME) data and compared to the AAIs derived from various Total Ozone Mapping Spectrometers (TOMS) instruments that have flown for the past 24 years. AAI data were derived from GOME before for the SCAR-B study [*Gleason et al.*, 1998], but only two weeks of data of GOME in its validation phase were considered. GOME data have also been used to retrieve aerosol optical thickness information [*Torricella et al.*, 1999], but these data are not very reliable. This is probably due to cloud contamination in the data.

2.4.1 TOMS

The Total Ozone Mapping Spectrometers (TOMS) were designed to provide daily global maps of ozone. Four TOMS instruments have flown on different platforms to provide a long term record of global ozone maps and related data products, among which is the AAI. Nimbus-7/TOMS was the most successful instrument, operating for fourteen years, from October 1978 to May 1993. Meteor-3/TOMS flew from October 1991 until December 1994. ADEOS/TOMS was launched in August 1996 after an eighteen month period when the program had no on-orbit capability and provided data until June 1997. Earth Probe (EP)/TOMS was launched in July 1996 into a sun-synchronous orbit with at an altitude of 500 km and an equator crossing time of about 1116 LT to provide supplemental measurements, but was boosted to a higher orbit (740 km altitude) to replace the failed ADEOS/TOMS in December 1997. The new orbit resulted in 90 % daily coverage (84 % at equator and 100 % at latitudes $\geq 30°$).

The TOMS instruments measure incident solar radiation and backscattered UV radiation at six discrete one nm wide wavelength bands. For the first three TOMS instruments these wavelength bands were centred around 313, 318, 331, 340, 360 and 380 nm. On EP/TOMS the 340 and 380 nm bands have been eliminated in favour of a 309 nm and a 322 nm band (Table 2.2). As a result the AAI from EP/TOMS was calculated with the 331 nm/360 nm pair, while previous AAIs were based on the 340 nm/380 nm pair.

TOMS AAI

TOMS daily residues and TOMS monthly AAIs can be downloaded from the Internet, both gridded to 1° latitude × 1.25° longitude grid boxes. TOMS AAIs are calculated by averaging daily positive residues over one month, with all averages lower than 0.7 set to zero. Erroneous measurements are flagged, which is true at least for all measurements at latitudes higher than 60° N and 60° S, where satellite measurements are inaccurate due to large solar zenith angles.

2.4.2 GOME

GOME is a 4–channel grating spectrometer, operating in the wavelength range of 237 – 794 nm with a spectral resolution of 0.2 – 0.4 nm. GOME was launched in April 1995 on board the ERS–2 satellite into a near-polar sun-synchronous orbit at a mean altitude of about 785 km, with a mean local equator crossing time of 1030 LT. GOME performs nadir observations by scanning the surface from east to west (corresponding to a viewing zenith angle of $-30°$ to $+30°$) in 4.5 s. One across-track scan is divided into three 1.5 s ground pixels with an average size of 40×320 km^2 each. For about 10 % of the time, the swath is reduced to 240 km, and all pixel sizes are four times smaller. Once per day the sun is observed over a diffuser plate for radiometric calibration. A region over the Himalayas is never observed, because in this region data from the ERS–2 satellite is downlinked to Earth and during this time no observation can be stored. Since 1999 – 2000 GOME suffers from serious radiometric degradation. Only GOME data from 27 June 1995 to 31 December 2000 were used.

2.4.3 Data Preparation and Corrections

A residue r was determined for each pair of calibrated GOME TOA reflectances centred at 335 nm and 380 nm, averaged over a one nm wide wavelength window (see *Koelemeijer et al.* [2003] for more details on the data calibration). The ground pressure in the residue calculation was found from the ETOPO–5 surface elevation database [*Haxby et al.*, 1983], assuming the MLS profile. For ozone the GOME level 2 total ozone column product was used. The solar and viewing angles were averaged over the GOME ground pixels. Pixels with solar zenith angles larger than 80° were discarded. The residues were gridded into 1° latitude × 1.25° longitude boxes for each day.

Daily and monthly mean AAIs were determined by averaging all positive residues in a box. To avoid single aerosol events from showing up in the monthly mean plots, a minimum of two AAIs was set for the monthly average to be valid. This excluded 0.01 % of the points. AAI values greater than 5.5 (0.0017 % of the data) were considered outliers and removed. At latitudes higher than 60°N and 60°S the AAI was not retrieved. Note that TOMS monthly mean AAIs start at 0.7 and GOME monthly mean AAIs start at 0.0.

As mentioned above, GOME suffered from severe degradation from 1999 onwards. The residues clearly show this degradation. The yearly averaged residue over 1996 – 1998 was very constant around -1, while after 1998 it decreased rapidly to -2 in 1999 and even -3.5 in 2000. To correct for this degradation the global monthly averaged residue was analysed. As shown in Figure 2.9 the residue varies sinusoidally over the years from 1995 to 1998, after that the signal decreases rapidly. The variation found in 1995 – 1998 was fitted to a sine with a period of one year. An amplitude of 0.13 and a phase shift of 8.0 (months) was found, the

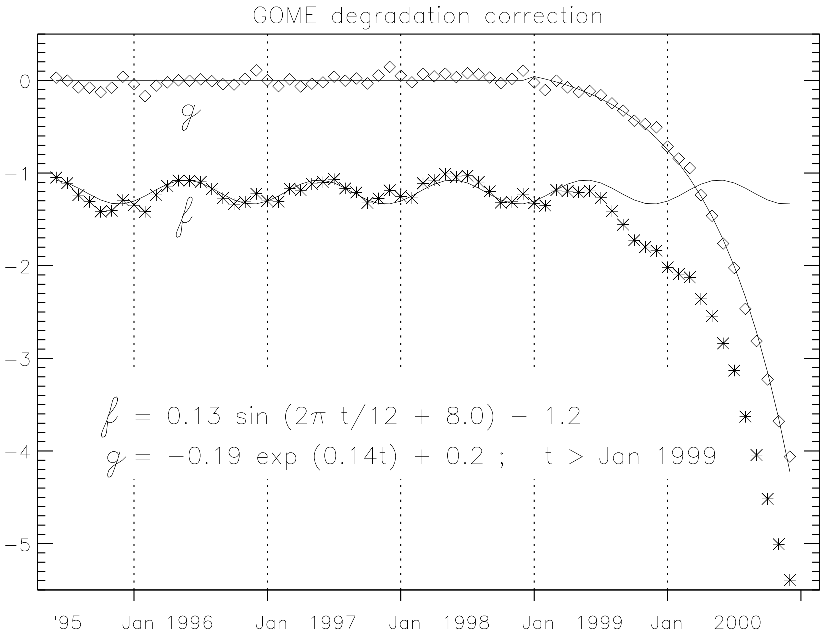

Figure 2.9: *Diagram illustrating the GOME degradation correction. The asterisks denote the global monthly mean AAI for the period 1995 – 2000. The period 1995 – 1998 was fitted to a sine function with a period of one year* $f = a_0 \sin(2\pi t/12 + a_1) + a_2$, *with* $a_0 = 0.13$, $a_1 = 8.0$, $a_2 = -1.2$. *The difference between the sine and AAIs of the last two months was fitted to an exponential function* $g = a_0 \exp(a_1 t) + a_2$, *with* $a_0 = -0.19$, $a_1 = 0.14$, $a_2 = 0.2$.

mean residue was −1.2. The residues from the years 1999 and 2000 were corrected with the difference between the global monthly averaged residues and the fit. This difference increases exponentially. The last two months of 2000 the residues and AAIs are not reliable anymore, because the correction is too large.

The sinusoidal variation was investigated further. To exclude the possibility of a solar zenith angle θ_0 error, the monthly averaged residue was determined in two 30° × 30° areas, one on the northern Hemisphere (NH) containing Hawaii (0° – 30° N, 150° – 180° W, blue box in Figure 2.10a) and one on the southern Hemisphere (SH) over the southern Indian Ocean (30° – 60°S, 60° – 90°E, red box in Figure 2.10a). In these areas very few aerosols are found throughout the year. In both areas a sinusoidal variation was found, but the phase shift was almost the same in both the NH (7.6 months) and the SH (7.9 months). As the θ_0 variations over both boxes have opposite signs, so would the residue variations if they were caused by θ_0 errors.

A possible explanation of the sinusoidal variation is the GOME solar calibration which is performed daily. The angle under which the sun illuminates the diffuser varies throughout the year. An error in the characterisation of the Bi-directional Scattering Distribution Function (BSDF) of the diffuser could lead to an error in the reflectance.

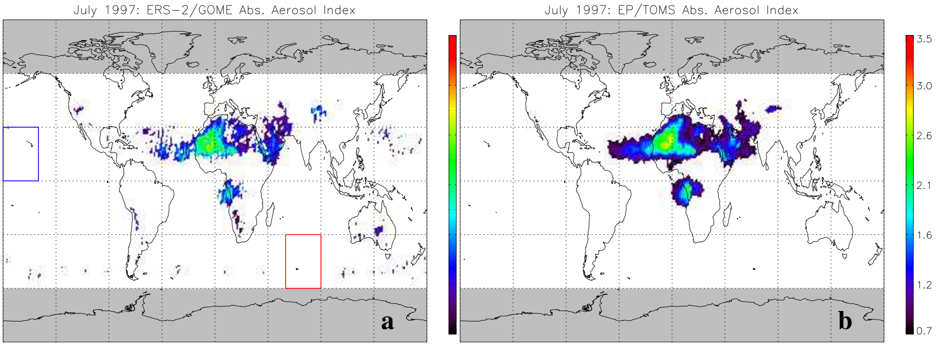

Figure 2.10: *(a) Global map of the monthly mean GOME AAI for July 1997. (b) Same for TOMS for July 1997. In the shaded areas no indices are retrieved. The blue and the red boxes in (a) indicate the areas for the solar zenith angle error analysis (see text).*

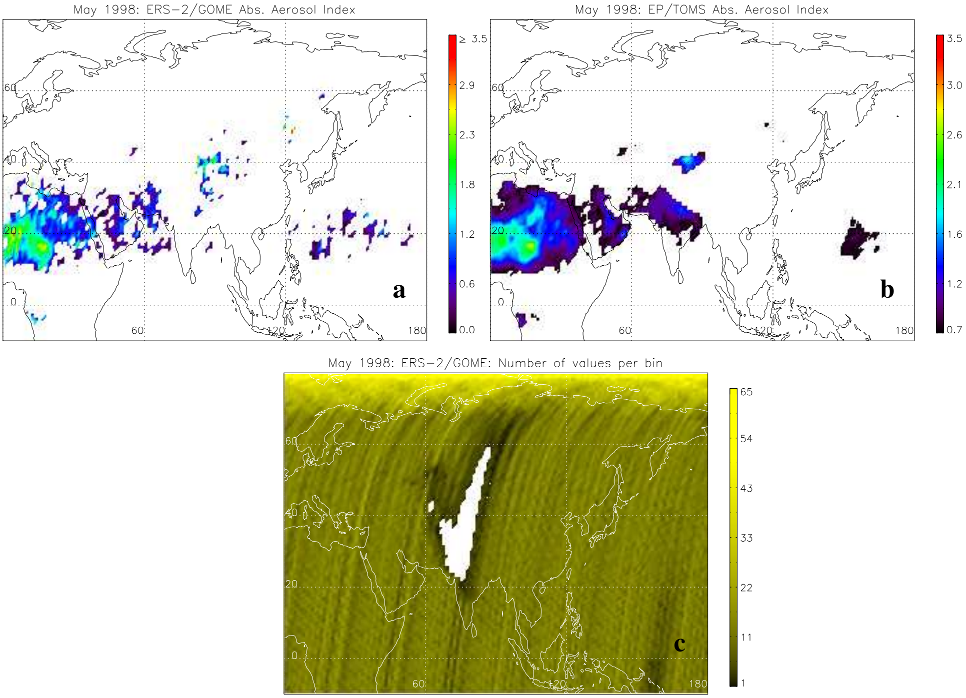

Figure 2.11: *(a) Monthly mean GOME AAI in May 1998 for the region centred on the Himalayas. (b) Same for TOMS in May 1998. (c) Plot of the number of residues used per bin to calculate the monthly mean GOME AAI in May 1998 for the same region as (a) and (b). The number of values is low (black) and even zero for a large part (white), due to GOME's data storage problem during downlinking of data.*

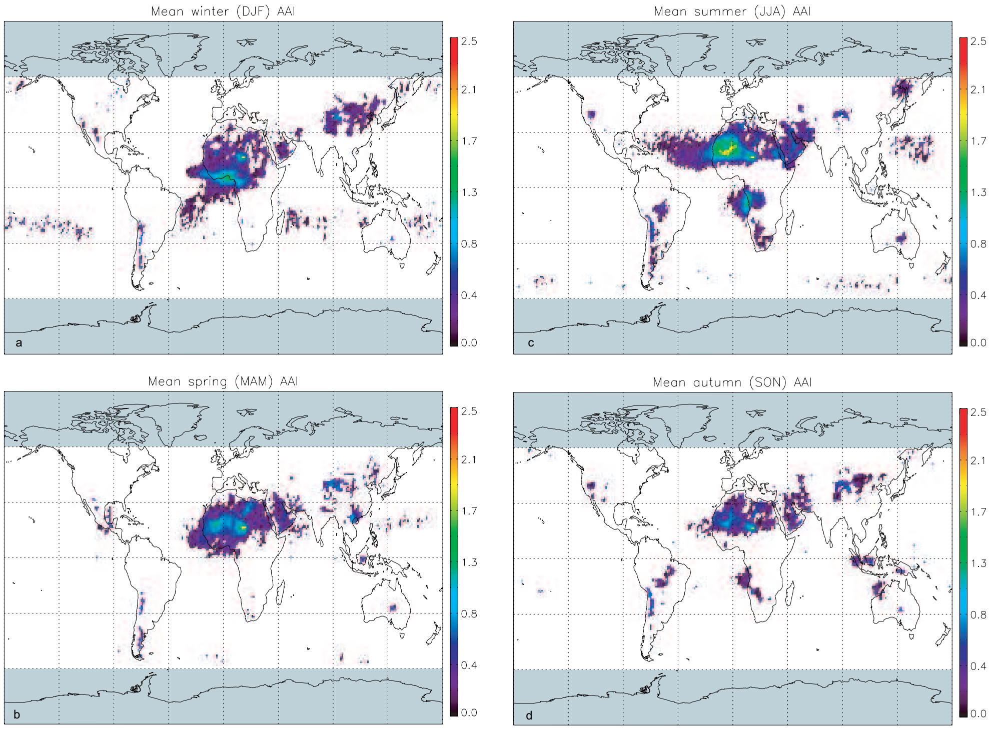

Figure 2.12: *Global maps of the GOME AAI for different seasons during the 5.5 years period June 1995 – December 2000. (a) Average AAI in December, January and February (DJF) of all years. (b) Same as (a) for March, April and May (MAM). (c) Same as (a) for June, July and August (JJA). (d) Same as (a) for September, October and November (SON).*

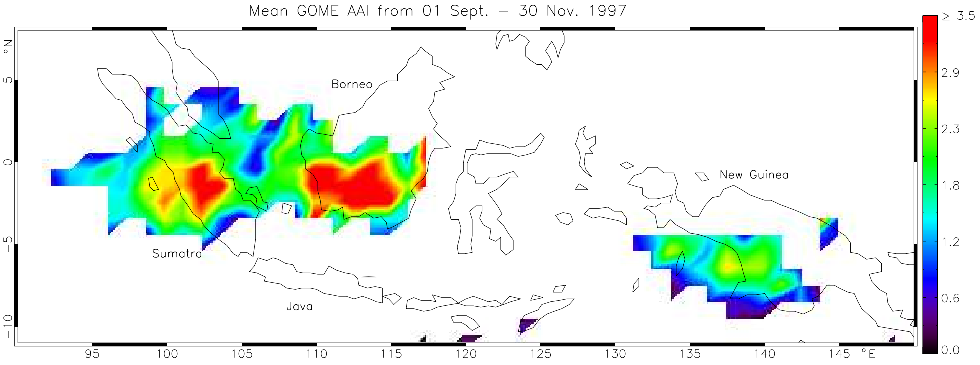

Figure 2.13: *Indonesian wildfires in the fall of 1997. Shown is the AAI averaged from 01 September – 30 November 1997.*

GOME Residues and AAIs

The data is available on the Internet at http://www.temis.nl. Both the daily files with the gridded residues and the monthly mean AAI and pictures of global monthly mean AAI can be found there.

Figure 2.10a is an example of the monthly averaged GOME 335 nm/ 380 nm AAI for May 1998. The TOMS index is shown in Figure 2.10b for the same month. The GOME AAI compares very well with the TOMS AAI. TOMS uses a threshold of 0.7, i.e. positive residues are averaged, but only averages larger than 0.7 are plotted. For GOME another threshold applies, because GOME data is calibrated differently and GOME uses different residue wavelengths than TOMS, so the absolute values also differ.

The GOME AAI is more patchy than the TOMS index. This is because GOME covers the Earth only every three days, while TOMS has daily global coverage, so GOME has three times less data.

To indicate the coverage of GOME an extra data file is provided on the Internet for every month of data available. This data file gives the number of residue values per bin in that month. An example of this number of values is given in Figure 2.11c. This figure shows the region centred on the Himalayas, which is the region where ERS–2 data is downlinked to the Earth and no data storage is possible, resulting in a gap where no data is ever available and a boundary area where only very few observations are available. The result of this phenomenon can be seen in Figure 2.11a and b. The TOMS data (Figure 2.11b) clearly shows an aerosol plume over India, which is absent in the GOME data (Figure 2.11a). This can be observed almost every spring, when TOMS data show aerosol plumes in this area, contrary to GOME data. Please recall that GOME needs at least two values per month in one bin to produce a valid monthly mean.

The GOME data show dense and persistent aerosol plumes over North Africa for all seasons, connected to very frequent dust storms over this part of the African continent, see Figure 2.12; in these figures the seasonal averages over all years are plotted. The centre of this plume is over the Sahara during the boreal summer and shifts to the south during the boreal winter. This feature, and other structures over the large aerosol sources, correspond well with those found in the TOMS data.

From July to August a persistent plume is present west of Angola. This is biomass burning aerosol from forest fires.

In all seasons plumes are present over Asia. The plumes in middle-east Asia may be dust aerosols from the Gobi desert, but they are generally not present in the TOMS data. A small part of the signal may be due to the presence of the Himalayas, which are not well resolved in the ETOPO-5 topography database. The database has a spatial resolution of $12' \times 12'$, which might be insufficient to resolve the high peaks of the Himalayas. This introduces errors in the ground pressure values, yielding high apparent residues (Figure 2.4a). The latter argument also holds for the signal over the Andes; a small but very persistent signal can be found there, which is probably caused by the insufficient resolution of the topography database.

An Amazonian aerosol plume can be found occasionally, connected to biomass burning of the tropical forests.

Over the southern oceans around Antarctica some spots of AAI can be found during spring and summer (Figure 2.12), which are absent in the TOMS data (compare Figures 2.10a and 2.10b). The reason for these AAIs is unclear but they might be caused by errors due to

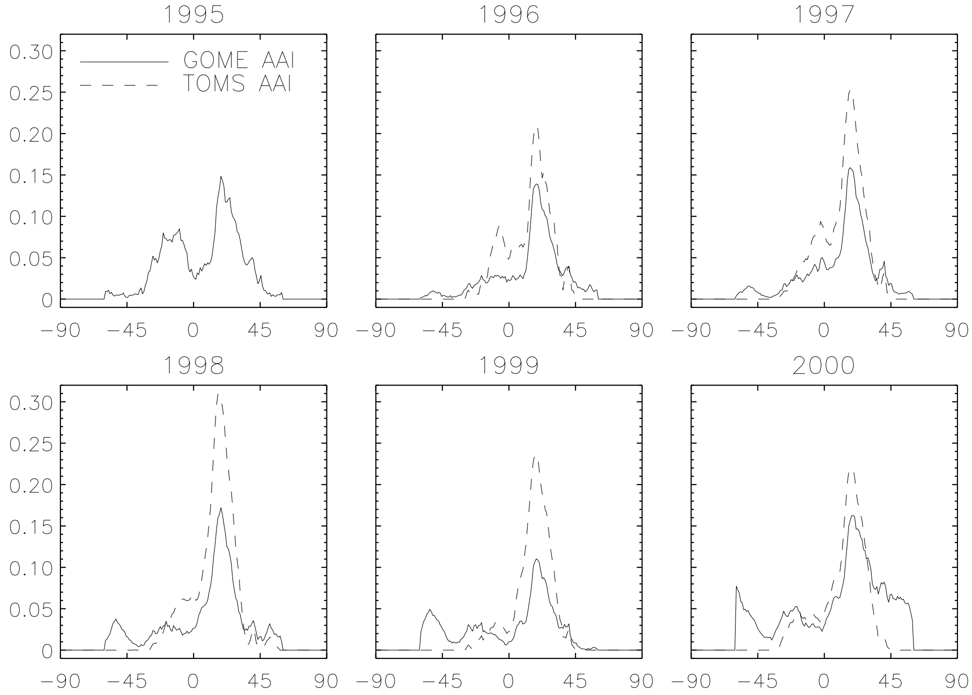

Figure 2.14: *Zonal mean of GOME AAI (solid line) and the TOMS AAI (dashed line) for six consecutive years as a function of latitude. Negative latitudes are on the southern hemisphere. From GOME only data from July to December was available in 1995 and in 2000 the last two months were discarded. TOMS data was available from July 1996 to December 2000.*

high solar zenith angles.

As another example of the GOME AAI the Indonesian wildfires of September to November 1997 are considered. These are captured very well by GOME (Figure 2.13). These fires released large amounts of UV absorbing aerosols, which show up in the data as high AAI values. The maxima of the 3 months averaged AAI correspond very well with the maxima of the total number of ATSR–2 fire-counts [*Duncan et al.*, 2003, Figure 1].

To determine the zonal behaviour of the AAI, the monthly means of the AAI were averaged over longitude per year from July 1995 until December 2000 (Figure 2.14, solid line). A clear maximum in the AAI exists over the subtropics in the NH, caused by the persistent subtropical aerosol sources like the Sahara and Gobi deserts. In the SH a smaller peak can be found in the subtropics, mainly caused by forest fires in the tropical forests and dust from Australian deserts. However, this peak is not always clear and shifts between 45° S and the equator. Between 45° S and 60° S another local maximum can be found which grows continuously from year to year. In 1995 the peak is almost absent, while in 1999 and 2000 its amplitude is bigger than that of the southern subtropical peak (see Figure 2.14). The reason for these high values of the AAI is unclear, but is probably a calibration error.

The NH subtropical maximum in the zonally averaged GOME AAI is very stable from year to year at about 0.15, contrary to the zonally averaged TOMS AAI, which was determined from July 1996 to December 2000 (Figure 2.14, dashed line). The TOMS AAI has its maximum at the same latitude as the GOME AAI, but its amplitude is always higher than that of the GOME AAI and it is much more variable, ranging from 0.20 to 0.32. As the TOMS AAI was determined with the 331 nm/360 nm pair it would be expected to be about 35 % lower than the GOME AAI, but instead it is up to twice as high. This might be caused by the lower sampling rate of GOME. As the AAI is an average of only positive residues (section 2.4.2) single high values can show up in these averages, and TOMS has a three times higher chance of sampling such a high value than GOME. Furthermore, the TOMS pixel size of 50 × 50 km is much smaller than the GOME pixel size of 40 × 320 km, which raises the chance of high residue values.

2.5 Conclusions

The Absorbing Aerosol Index (AAI) separates absorbing from scattering effects in the UV, which makes it useful to monitor UV-absorbing aerosols like desert dust and biomass burning aerosols from space, both over land and sea. The AAI is based on the spectral contrast of the reflectances at two UV wavelengths, compared to that of a pure Rayleigh atmosphere. Its absolute value depends on many parameters, most notably aerosol optical thickness, the height of the absorbing layer, and in the case of aerosols, the microphysical properties of the aerosols. This makes a unique retrieval of one of these aerosol quantities from the AAI difficult.

Data from the Global Ozone Monitoring Experiment (GOME) instrument can be used to retrieve the AAI. These AAI data correspond well with known UV-absorbing aerosol events and the TOMS AAI. As GOME has a global coverage only every three days, the AAI is not very suitable to monitor aerosol events on a day-to-day basis, but well suitable to provide monthly global maps of absorbing aerosols. The GOME AAI is particularly useful in the period July 1995 – August 1996, when there were no measurements from TOMS.

The residue r is very sensitive to errors in the reflectances and can be used as an additional calibration tool. The sinusoidal variation found in the global AAI data is probably due to a calibration error previously undetected in the GOME radiance data. The amplitude of the variation was 0.15 in r, which corresponds in first order approximation to a very small variation in R_λ^{meas} of 0.0035 (see equation 2.4).

The cause for the AAI over the southern oceans around Antarctica is unclear. Applying the calibration correction described previously slightly reduced the signal, but did not eliminate it. It is unlikely that these AAIs correspond to aerosol events in this area, because the air around Antarctica is usually very clean and also the TOMS data do not show any high values there. But no explanation was found so far.

The topography database used for retrieval of the GOME AAI has an insufficient spatial resolution to resolve the steepest mountain ranges in the world, like the Himalayas and the Andes. This yields apparent residues over mountainous areas when there are no aerosol events. This problem can be resolved with a database with a higher resolution.

The quantitative use of the aerosol information content in the satellite measurements of near UV radiances has been used to develop an algorithm to retrieve aerosol optical thickness and single scattering albedo [*Torres et al.*, 1998, 2002]. The near UV algorithm has been applied to the TOMS record [1979-2000], to produce the longest available AOT data set over the oceans and the continents [*Torres et al.*, 2002]. Both the AOT and the single scattering albedo products have been validated making use of ground based observations [*Torres et al.*, 2002, 2005]. The near UV algorithm is also being applied to observations by the recently deployed Ozone Monitoring Instrument (OMI) on the Aura satellite

This work could be extended with SCIAMACHY data, once data will become available. The GOME and SCIAMACHY extended spectral range may be used to improve the AAI. Incorporating information at other wavelengths, e.g. in the visible, may help separate different aerosol species or retrieve other aerosol information [*Torres et al.*, 2001].

Acknowledgements This work was financed by the Dutch Space Agency (NIVR) SCIAMACHY validation project and DAEDALUS, project number EVK2-CT-2002-00174.

3

Temporal and spectral variation of desert dust and biomass burning aerosol scenes from 1995 – 2000 using GOME

Abstract

Global Ozone Monitoring Experiment (GOME) Absorbing Aerosol Index (AAI) and AAI-related residue data were used to investigate areas with UV-absorbing aerosols. Time series of regionally averaged residues show the seasonal variation and trends of aerosols and clouds in climatologically important parts of the globe. GOME spectra were used to study scenes containing specific types of aerosols. AAI data are specifically sensitive to biomass burning aerosols (BBA) and desert dust aerosols (DDA). Areas where these aerosols are regularly found were analysed to find spectral fingerprints in the ultraviolet (UV), visible and near-infrared (near-IR), to establish an aerosol type classification of BBA and DDA. Spectral residues are different for BBA and DDA, but over deserts the surface albedo is dominant beyond the UV and spectral residues cannot be used over land. Over oceans, about half of the BBA scenes show a very high reflectance that is never observed for DDA scenes. However, in the case of low reflectance scenes BBA and DDA cannot be distinguished. This is in part due to the microphysical and optical properties of biomass burning aerosols, which are highly variable in time, making it difficult to specify them spectrally as one type. Because of their high hygroscopicity BBA are often found in the presence of clouds, which disturb the spectrum of the scenes. Desert dust aerosols are much less hygroscopic and behave spectrally more uniformly.

M. de Graaf, P. Stammes, I. Aben (2006) *ACPD 6*, SRef-ID: 1680-7375/acpd/2006-6-1321

3.1 Introduction

The Absorbing Aerosol Index (AAI) [*Herman et al.*, 1997; *Torres et al.*, 1998; *De Graaf et al.*, 2005] record is well-known as the longest record of global aerosol measurements currently available and the AAI has been used to indicate UV-absorbing aerosols, starting with Total Ozone Mapping Spectrometer (TOMS) data in 1978. Several new instruments are currently adding independent and complementary AAI data, like GOME [*De Graaf et al.*, 2005], SCanning Imaging Absorption SpectroMeter for Atmospheric CartograpHY (SCIAMACHY) [*De Graaf and Stammes*, 2005] and Ozone Monitoring Instrument (OMI) [*Torres et al.*, 2001]. The AAI can be regarded as the colour of a scene, at two UV wavelengths (usually 340 and 380 nm), as compared to the colour of a pure Rayleigh atmosphere. Its greatest advantage is the applicability over both land and oceans and the low sensitivity to sub-pixel cloud contamination. The AAI is sensitive to UV-absorbing aerosols and has been used extensively to study two well known types of UV-absorbing aerosols, desert dust [e.g. *Chiapello et al.*, 1999; *Alpert and Ganor*, 2001; *Pandithurai et al.*, 2001; *Spichtinger et al.*, 2001; *Prospero et al.*, 2002; *Colarco et al.*, 2002; *Moulin and Chiapello*, 2004] and biomass burning aerosols [e.g. *Hsu et al.*, 1996; *Gleason et al.*, 1998; *Hsu et al.*, 1999a, b; *Goloub and Arino*, 2000; *Darmenova et al.*, 2005].

Time series of TOMS data have been used to study seasonal variation of regional aerosol loading. The global distribution and the spatial coverage of UV-absorbing aerosols were demonstrated with time series of TOMS AAI-related residues from 1984 to 1988 [*Herman et al.*, 1997]. TOMS AAI data from 1979 to 1993 were converted to aerosol optical thicknesses (AOT), using geographical information on aerosol type and assuming a height for the aerosol layer, and regionally averaged AOT time series showed the seasonal variation of major desert dust and biomass burning areas around the Atlantic Ocean [*Torres et al.*, 2002]. Here, time series of regional averaged residues are presented from 1995 to 2000 for a number of climatologically important parts of the globe. Using these time series and other studies, the types of aerosols that are most important for these areas are identified. The influence of the African Monsoon on the aerosol loading over Africa is demonstrated.

Desert dust and biomass burning aerosols have the same effect on the UV radiation by attenuating the Rayleigh reflected radiation below the aerosol layer [e.g. *Torres et al.*, 1998; *De Graaf et al.*, 2005]. Desert dust also has a direct effect on the AAI because of its strongly wavelength-dependent imaginary part of refractive index in the UV [*Sinyuk et al.*, 2003; *De Graaf et al.*, 2005]. In the wavelength region from 0.4 to 1.0 μm the spectral dependence of the absorption coefficients of DDA and BBA is different: Biomass burning aerosols with a black carbon (BC) core, obtained with an aircraft over the North Atlantic Ocean, showed a decreasing single scattering albedo with increasing wavelength, while most mineral aerosols have an increasing single scattering albedo with increasing wavelength [*Bergstrom et al.*, 2002]. Ground-based (AERONET) data showed a similar spectral distinction between BBA and DDA in the same (440 to 1020 nm) spectral region: The single scattering albedo of BBA decreases with wavelength, while the single scattering albedo of DDA increases in the near-UV and becomes constant at longer wavelengths [*Dubovik et al.*, 2002a]. Here, the effect of these spectral differences on the measured scene is investigated, using empirical data in the spectral range 335 – 772 nm of GOME scenes containing known types of UV-absorbing aerosols.

The different GOME products are first described and defined in section 3.2. Next, in section 3.3 the time series of regionally averaged GOME residues are presented and used to identify aerosol characteristics in areas that are known to be influenced by UV-absorbing aerosols. In section 3.4 GOME spectra of reflectances (3.4.1) and residues (3.4.2) at UV to near-IR wavelengths from areas with known types of aerosols are explored to find aerosol specific fingerprints caused by spectrally different absorbing characteristics. An attempt is made to make a distinction between desert dust and biomass burning aerosols (3.4.3), using statistical information of the GOME spectra. The results are discussed in section 3.5.

3.2 Definition of GOME residues

GOME [*Burrows et al.*, 1999] is a 4–channel grating spectrometer, operating in the wavelength range of 237 – 794 nm with a spectral resolution of 0.2 – 0.4 nm. GOME was launched in April 1995 onboard the ERS–2 satellite into a near-polar sun-synchronous orbit at a mean altitude of about 785 km, with a mean local equator crossing time of 1030 LT. GOME performs nadir observations by scanning the surface from east to west (corresponding to a viewing zenith angle of −30° to +30°) in 4.5 s. One across-track scan is divided into three 1.5 s ground pixels with an average size of 40×320 km^2 each. For about 10 % of the time, the swath is reduced to 240 km, and all pixel sizes are four times smaller. Once per day the sun is observed over a diffuser plate for radiometric calibration. A region north of India is never observed, because in this region data from the ERS–2 satellite is downlinked to Earth and during this time no observations can be stored. Since 1999 – 2000 GOME suffers from serious radiometric degradation in the UV. Therefore, only GOME data from 27 June 1995 to 31 December 2000 were used [*De Graaf et al.*, 2005].

GOME measured reflectances were used to determine residues. The residue r_{λ,λ_0} is a wavelength-dependent variable defined as [*Herman et al.*, 1997]

$$r_{\lambda,\lambda_0} = -100 \cdot \left\{ {}^{10}\log\left(\frac{R_\lambda}{R_{\lambda_0}}\right)^{\mathrm{meas}} - {}^{10}\log\left(\frac{R_\lambda}{R_{\lambda_0}}\right)^{\mathrm{Ray}} \right\}. \tag{3.1}$$

R_λ is the reflectance at wavelength λ, defined as $R_\lambda = \pi I_\lambda / \mu_0 E_0$, with I_λ the radiance at the top of the atmosphere (TOA) at a wavelength λ, E_0 the solar irradiance at TOA perpendicular to the direction of the incident sunlight and μ_0 the cosine of the solar zenith angle θ_0. R^{meas} is the measured TOA reflectance in a real atmosphere with aerosols and R^{Ray} the calculated TOA reflectance in an aerosol-free atmosphere with only Rayleigh scattering and absorption by molecules, bounded from below by a Lambertian surface. At the reference wavelength λ_0 a surface albedo A_{λ_0} is calculated so $R^{\mathrm{Ray}}_{\lambda_0}(A_{\lambda_0})$ is identical $R^{\mathrm{meas}}_{\lambda_0}$. Then Eq. (3.1) can be reduced to

$$r_{\lambda,\lambda_0} = -100 \cdot {}^{10}\log\left(\frac{R^{\mathrm{meas}}_\lambda}{R^{\mathrm{Ray}}_\lambda(A_{\lambda_0})}\right). \tag{3.2}$$

λ is the wavelength where the difference between the Rayleigh and the measured scene is calculated. The residue can be calculated for any wavelength pair $[\lambda, \lambda_0]$.

Reflectances were determined at eleven wavelengths, namely 335, 380, 416, 440, 463, 495, 555, 610, 670, 758, and 772 nm, corresponding to the wavelengths at which the GOME surface albedo database was determined [*Koelemeijer et al.*, 2003]. The reflectances were averaged over a one nm wide wavelength window and pixels with solar zenith angles larger than 80° were discarded.

Ten spectral residues were determined with reference wavelength $\lambda_0 = 380\,\mathrm{nm}$, $r_{\lambda,380}$, for all wavelengths other than 380 nm listed above ($r_{\lambda_0,\lambda_0} = 0$). The reference wavelength can be varied, and the sensitivity of the residue is different at different wavelengths because of the varying Rayleigh reflectance, which can be very strong in the UV. Moreover, the relationship between r_{λ,λ_0} and $r_{\lambda_0,\lambda}$ can be nonlinear [*De Graaf and Stammes*, 2005]. But for reference wavelengths in the visible and IR the high surface albedo over land completely dominates the residue. So of the 55 possible wavelength combinations per pixel (no extra information is added with a change of $[\lambda, \lambda_0] \rightarrow [\lambda_0, \lambda]$) only the ten residues with $\lambda_0 = 380\,\mathrm{nm}$ were retained, because 380 nm is the wavelength traditionally used for the AAI and in the UV the surface albedo is dark over both land and oceans.

The AAI is defined as the positive residue determined at $[\lambda, \lambda_0] = [335, 380\,\mathrm{nm}]$, $r_{335,380} > 0$. In general, all pixels with a residue greater than zero are indicative for UV-absorbing aerosols in the scenes [*Hsu et al.*, 1996; *Torres et al.*, 1998; *De Graaf et al.*, 2005]. In this paper a threshold of 0.5 is used to select scenes with UV-absorbing aerosols. Negative residues also contains geophysical information, as is shown in this paper. Negative values generally indicate clouds or scenes free of UV-absorbing aerosols, but these have never yet been investigated.

Between 1995 and 2000 the global monthly averaged residue varied sinusoidally around a mean of −1.2 with an amplitude of 0.13 and a phase shift of 8.0 months. The possibility of a solar zenith angle error for this sinusoidal variation was ruled out, and the sine was removed as it was believed to be the result of an error in the characterisation of the Bi-directional Scattering Distribution Function (BSDF) of the solar diffuser plate of GOME. After 1998 an exponential decrease in the residue was found of about −4 in two years, due to degradation of the UV-channels of GOME which was stronger at 335 nm than at 380 nm. This was also corrected. The corrections in the last two months of the data set, Nov. and Dec. 2000, were rather large and the data of these months should be treated with caution. (See *De Graaf et al.* [2005] for more details on the data calibration.) The resultant global mean residue was −1.2 with a variation in the monthly average of less than 0.25.

3.3 Temporal behaviour of UV-absorbing aerosols from GOME

3.3.1 GOME regionally averaged residue time series

Fifteen areas on the globe were selected to study the local time series and trend of the GOME residue $r_{335,380}$ in that area (see Fig. 3.1), 1: northwest Africa (red); 2: North Atlantic Ocean (magenta); 3: southwest Africa (green); 4: South Atlantic Ocean (cyan); 5: Sahel (khaki); 6: Indonesia (dark green); 7: northern South America (light green); 8: western Europe (blue); 9: Australia (yellow); 10: Saudi Arabia (brown); 11: India (grey); 12: Gobi Desert (orange); 13: Hong Kong (purple); 14: Alaska (blue grey); 15: western North America (brick red). The GOME residue $r_{335,380}$ was averaged over each of these areas daily from July 1995 –

December 2000 (Fig. 3.2), to show the characteristic long-term time series of phenomena related to aerosols and clouds in these particular areas. Residues of all pixels in the areas were averaged, not only residues larger than zero or 0.5. Averages of AAI are also possible, but because the AAI is only defined from zero upwards, averages of AAIs are hard to interpret. Since cloudy and aerosol-free pixels give negative values, the average residue of an area will usually be negative. UV-absorbing aerosol events will raise the average, but not necessarily to positive values. The global daily residue was also determined.

Over northwest Africa and the North Atlantic Ocean very high residues can be found, caused by frequent desert dust blowing events. These desert dust plumes often extend far over the North Atlantic. The sources of both plumes are the desert areas of the Sahara [e.g. *Prospero et al.*, 2002; *Reid et al.*, 2003; *Kaufman et al.*, 2005], therefore the two curves are highly correlated. The curves show a high seasonal variation, the residue peaking in the boreal summer months due to increased wind speeds when the sun is higher overhead. A similar seasonal variation was found in these areas between 1979 and 1993 using TOMS AOT [*Torres et al.*, 2002]. The aerosol loadings over the Sahara were highest in May–July and in July over the Atlantic Ocean between 1979 and 1993. No such time lag exists between these areas in 1995 – 2000.

Over southwest Africa a very clear seasonal variation can also be observed, with high residues in the austral spring. These high residues are caused by anthropogenic biomass burning in the dry period, while the low residues are caused by the monsoon rains, see below. The biomass burning aerosol plumes extend over the South Atlantic Ocean, and the residue over the South Atlantic correlates well with the residue over southwest Africa. Both signals show a secondary maximum in the austral summer, which is caused by aerosols just north of the equator being blown south. The same secondary maxima were also found in TOMS AAI data in areas south of the equator [*Herman et al.*, 1997; *Torres et al.*, 2002]. The region just north of the equator, the Sahel, shows a very strong seasonal variation which peaks at the dry season. In the Sahel biomass burning aerosols and desert dust are often found together in the dry season and it is not clear which aerosols cause the strong maxima. The central African regions are treated in more detail in section 3.3.2.

In Indonesia forest fires are very common during dry periods, but there are usually many single fires scattered throughout the selected region, which cannot be seen in the regional average, so a seasonal variation is not visible in Fig. 3.2. However, from September 1997 till November 1997 severe biomass burning events caused huge persistent forest fires in Borneo and other parts of Indonesia in the El-Niño year 1997 [*Duncan et al.*, 2003], causing high AAIs in this area [*De Graaf et al.*, 2005]. These events were so severe that they cause a solitary peak in the regional averaged residue over Indonesia in the fall of 1997.

High residues are observed over northern South America in boreal autumn almost every year, which is caused by biomass burning of the tropical forests. The strong seasonal variability is consistent with SCAR-B observations, which showed fire activity peaks in late August and September in 1995 [*Kaufman et al.*, 1998], and TOMS AAI, which showed peak values in August and September from 1979 to 1993 [*Torres et al.*, 2002].

Over Europe, very few UV-absorbing aerosols are observed by GOME, therefore the overall residue is low year-round. A clear seasonal signal is observed with higher residues in the winter.

Over Australia no clear pattern is visible. Although in this area desert dust and biomass

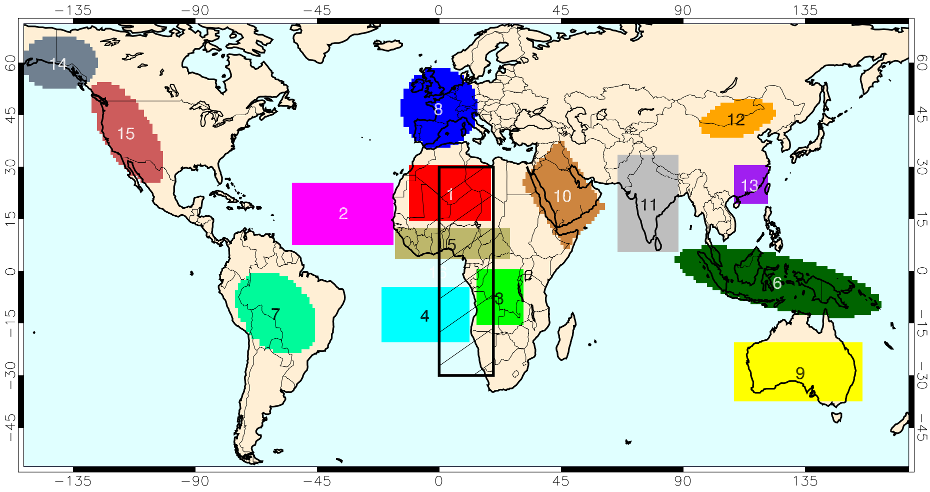

Figure 3.1: *Regions for which the area-averaged GOME residue $r_{335,380}$ time series was determined from July 1995 to December 2000 (coloured and numbered areas), shown in Fig. 3.2. The shaded area was used to determine the temporal behaviour of the zonally averaged GOME residue $r_{335,380}$, shown in Fig. 3.3.*

burning events are common, these events are irregular in space and time and the area-averaging smooths out the events. The north of Australia, where biomass burning events are most common [e.g. *Tanré et al.*, 2001], has been excluded in the present analysis, because this area has the same characteristics as Indonesia.

The Saudi Arabian peninsula shows high residues and distinct seasonalities, correlating well with the signal in northern Africa. The signal over Saudi Arabia is smaller than over northern Africa, but the seasonalities match, because both are caused by desert dust changes driven by the same seasonal variation of the sun over both areas.

Over India residues are highest in spring and lowest in autumn. The source of UV-absorbing aerosols is biomass burning from urban and industrial areas. This pollution reaches its maximum at the end of the hot dry season. The monsoon rains set in in May in the south and in June in the North, lowering the temperatures and washing the aerosols from the atmosphere. After the period of the retreating monsoon, from September in the north to December in the south, the aerosol loading is gradually increased again.

Over the Gobi Desert a strong seasonality can again be observed, with high peaks in the boreal winter, which is its dry period. The source of the high residues over the Gobi Desert is of course desert dust [e.g. *Prospero et al.*, 2002; *Darmenova et al.*, 2005; *Kim et al.*, 2005].

The same strong seasonal variation can be observed over Hong Kong as well. Pollution by industrial aerosols often affects this area [*Tanré et al.*, 2001], however, the high correlation between the residue signal from the Gobi Desert and that from the Hong Kong area suggests a connection between the origin of the high residues over both areas (which is desert dust for the Gobi desert).

Over Alaska, western Canada and the north Pacific a seasonal variability with high resi-

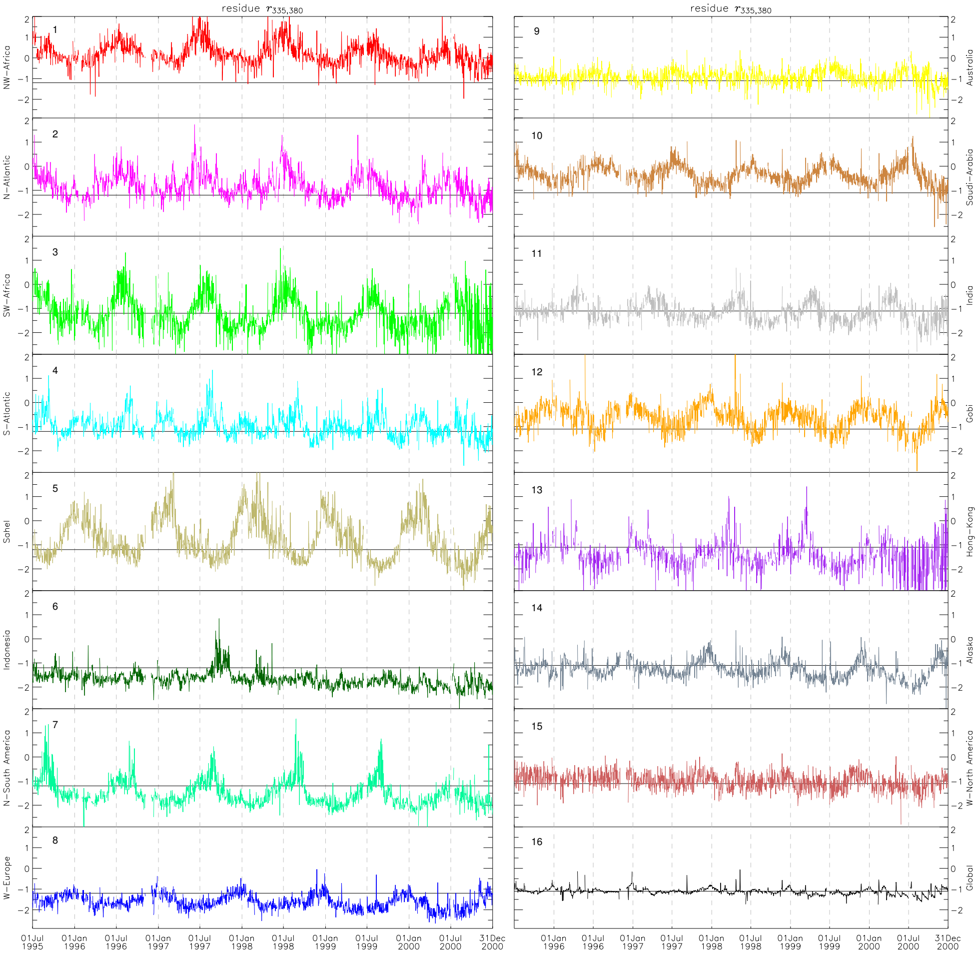

Figure 3.2: *Five and a half year daily GOME residue* $r_{335,380}$ *time series from July 1995 to December 2000 averaged over the areas indicated in Fig. 3.1. The solid black line shows the global average GOME residue of* -1.2.

dues in the boreal winter can be observed. Although this area must be treated with care in view of the large solar zenith angles in winter, biomass burning aerosols from forest wildfires are not uncommon here.

The west coast of North America shows a rather constant signal of negative averaged residues, although occasional outbreaks of forest fires and desert dust events cause locally high residues. But these are irregular and smoothed out in the average.

The global mean residue between 1995 and 2000 is -1.2, with a small decreasing trend of -0.029 per year. The trend is probably due to degradation of the sensors; a residue difference of 0.029 amounts to a reflectance error of less than 0.07 %. The global mean residue does not show any seasonal variation in Fig. 3.2, because a sine with a period of one year (amplitude 0.13 and phase shift of 8.0 months) was filtered out of the data, since it was believed to be a calibration error (see section 3.2). In view of the above discussions, a sinusoidal seasonal variation in the global mean residue could also have a geophysical cause.

3.3.2 GOME residue – African Monsoon relationship

The GOME residue $r_{335,380}$ of the shaded area in Fig. 3.1 (30° S – 30° N, 0°– 20° E), which is an area that is strongly influenced by the African monsoon (both West and East African Monsoon [e.g. *Webster*, 1987; *Janicot et al.*, 1998; *McGregor and Niewold*, 1998]), was averaged zonally. The time series from July 1995 to December 2000 of this zonally averaged residue is plotted in Fig. 3.3a. During the dry period in Africa, desert dust storms and biomass burning events cause high residues, indicated by red pixels. Outside the dry months the monsoon rains prevent the existence of dust storms, fires and aerosol plumes. The atmosphere is cloudy and washed clean, yielding negative residues. As the InterTropical Convergence Zone (ITCZ) and monsoon rains shift with the seasons the negative residues travel along with it, causing the sinusoidal violet-blue path through Fig. 3.3a.

In the north, located over the Sahara, GOME residues are high year-round. North of 20° N the GOME residue peaks in the boreal summer months, in accordance with the time series in Fig. 3.2. A small area centred around 17° N has very high GOME residues year-round for all the years shown. This coincides with the Bodélé depression, an area centred around 17° N, 18° E, which is known to be a enormous source of desert dust aerosols [*Prospero et al.*, 2002].

North of the equator, between 0° and 10° N the GOME residues alternate between high, positive values in the boreal winter months and negative values in the boreal summer months. The high values in winter have two possible origins: biomass burning aerosols from the vegetated Sahel region or desert dust blown in from the Sahara, north of this area. The local aerosol peaks centred around 5° N seem to be disconnected from the desert dust peaks at about 18° N, but mixing with desert dust transported from the north cannot be ruled out. The GOME residue cannot be used to distinguish between these types, but most likely both types of aerosols can be present in the Sahel area, depending on the prevailing wind directions.

Between 0° and 10° S the picture is a bit more complicated. The aerosols in the primary maxima in boreal summer to autumn are local biomass burning aerosols from vegetation fires. The time series of southwest Africa (Fig. 3.2) also showed secondary maxima in boreal winter, which were also found in TOMS residues in a box just south of the equator in Africa between 1984 and 1988 [*Herman et al.*, 1997] and less clearly in TOMS AOT from 1978 to 1993 [*Torres et al.*, 2002], because in the latter only data from 5°– 25° S was used. These secondary maxima were attributed to excursions of smoke aerosols from events just north of the equator to the south by the prevailing winds. Figure 3.3a confirms these excursions of aerosols from north of the equator to the south. However, since the types of aerosols north of the equator are uncertain, the biomass burning aerosols in these secondary maxima can also be mixed with desert dust.

Below about 10° S the GOME residue alternates between high values in boreal summer and autumn and low values in boreal winter, out of phase with residues just north of the equator. The high residues are caused by persistent local vegetation fires occurring every year in and around Angola in the dry period. These fires are mainly man-made to benefit agriculture. The arid west coast of Namibia also regularly produces desert dust, but these contributions are small and usually not picked up by the AAI [*Eckardt and Kuring*, 2005].

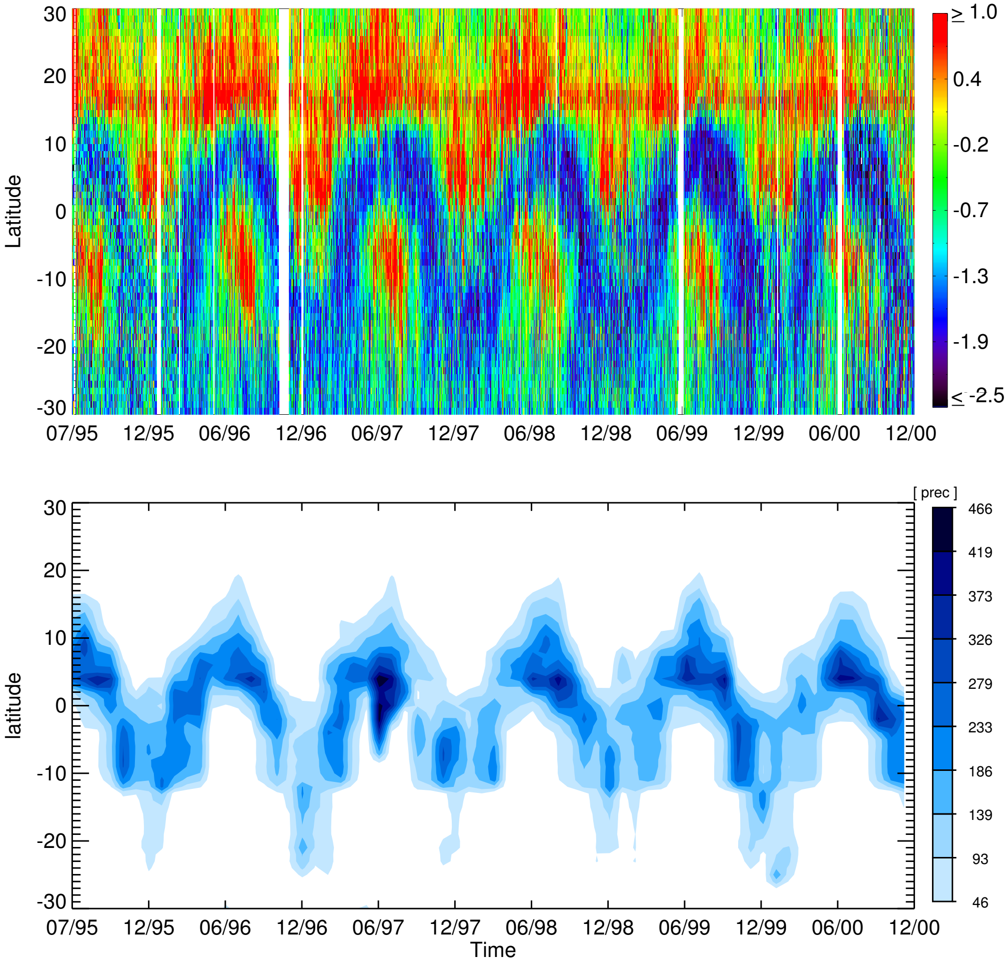

Figure 3.3: *(a) Zonally averaged GOME residue* $r_{335,380}$ *of the shaded area in Fig. 3.1 for each day between July 1995 and December 2000. (b) One by one degree gridded and monthly averaged GPCC precipitation in the shaded area in Fig. 3.1, averaged zonally, from July 1995 and December 2000.*

To check the relationship between negative GOME residues and monsoon rains, the precipitation in the shaded area of Fig. 3.1 was also averaged zonally (Fig. 3.3b). The data used for this figure were precipitation observations gridded to a one by one degree grid, obtained from Deutscher Wetterdienst (`http://gpcc.dwd.de`). Although precipitation data are usually very irregular, the data in Fig. 3.3b correlate very well with the GOME residue, even when the GOME residues were plotted for each day that the data were available, while the precipitation data were monthly averaged.

Figure 3.3 shows the asymmetry of the African monsoon: In the north there is a clear boundary of the monsoon at about 15° N, visible in both the GOME residues and the precipitation data. In the south the monsoon boundary is not very clearly defined and the monsoon travels farther south than north. The well defined northern boundary is caused by dry, hot winds blowing from the north, known as the Harmattan. This hot dry continental air is less dense than the cool moist south-westerly monsoonal flow and is uplifted, suppressing local precipitation [e.g. *McGregor and Niewold*, 1998], and hence suppressing negative residues. Because the ITCZ travels farther south than north and since aerosol plumes will probably not cross the ITCZ, the aerosol plumes originating north of the equator are able to cross the equator, while the aerosol plumes originating south of the equator are mainly confined to the south.

3.4 Spectral behaviour of UV-absorbing aerosols from GOME

In this section GOME spectra of biomass burning aerosol scenes and desert dust aerosol scenes are explored to examine the effect of their spectrally different absorption coefficients on the measured scene. The investigation is restricted to a statistical survey of GOME spectra in four areas, numbers 1 – 4 in Fig. 3.1, which are assumed to be typical for the occurrence of BBA and DDA types, both over land and ocean.

3.4.1 Reflectance spectra

All measured GOME reflectance spectra of scenes containing UV-absorbing aerosols from June 1997 until August 1997 were averaged for each of the four areas (see Fig. 3.4). Scenes with UV-absorbing aerosols were selected choosing only those with an AAI greater than 0.5, therefore the reflectance at 335 nm is always greater than the reflectance at 380 nm. The number of UV-absorbing GOME scenes between June and August 1997 in northwest Africa was about 20,000, over the North Atlantic Ocean about 10,000, in southwest Africa about 3500 and over the South Atlantic Ocean about 4000. In grey-scale a contour plot is given of the histogram of all spectra in the three months, indicating the range of the spectra, while the solid line is the averaged spectrum. The dashed line shows the surface albedo spectrum of the areas averaged over the months June to August. These were determined from GOME minimal reflectances in the years 1995 to 2000 for each month [*Koelemeijer et al.*, 2003].

Over northwest Africa (left upper panel in Fig. 3.4) the reflectances of the (mineral) aerosol laden scenes decrease with increasing wavelength in the UV, and increase with increasing wavelength in the visible and near-IR. In the visible and near-IR the desert surface is very bright and the reflectance is increasingly dominated by the surface albedo. Only below about 500 nm is the desert surface dark enough that the atmospheric component can be distinguished from it.

Over the North Atlantic Ocean (left lower panel) the surface albedo is low in the UV, and even lower in the visible and the near-IR. Thus, the behaviour of the reflectance is primarily due to atmospheric effects. The reflectances of the desert dust aerosol scenes over the ocean decrease with increasing wavelength over the entire spectral region.

Over southwest Africa (right upper panel) the reflectances of the (biomass burning) aerosol laden scenes decrease with increasing wavelength until about 650 nm, after that the reflectances start to increase with increasing wavelength. This is because vegetation is dark until about 650 nm, after that it rapidly becomes brighter with increasing wavelength. In addition, BBA have a black carbon core which is highly absorbing and, although the BBA scene spectra over land have a large spread, on average the reflectance is low.

Over the South Atlantic Ocean (right lower panel) the surface is again dark at all wavelengths, and the average reflectance is almost constant with wavelength. The average reflectance of the BBA scenes over the ocean is much higher than over land, and also the spread is larger.

The spectral behaviour of BBA over ocean is distinctly different from that over land, because BBA is chemically very active and highly hygroscopic, and its internal chemical and physical properties change quickly during the first few hours to days after its creation. The cores of fresh biomass burning aerosols are made up of black carbon and other substances, depending on the source (e.g. combustion and fuel type). Fresh biomass burning aerosols are known to burn away clouds due to the semi-direct effect [*Hansen et al.*, 1997; *Ackerman et al.*, 2000]: The black carbon cores of the aerosols absorb solar radiation and heat the atmosphere locally, inhibiting cloud growth. Therefore, clouds and biomass burning aerosols are rarely found together near fires [*Koren et al.*, 2004]. As the BBA age and move away from the source the aerosols are coated with water, reducing the absorption efficiency of the black carbon core and the aerosols become very efficient cloud condensation nuclei (CCN). Therefore, scenes with aged BBA are often cloud contaminated. Clouds yield high, gray reflectances, and polluted clouds also yield high residues. The relative importance of these competing properties of BBA change over time, which is expressed by the different spectra over land and ocean. Over land BBA scene spectra are on average lower than those over oceans, because over oceans biomass burning aerosols are by definition aged aerosols well away from the source. The most important effect of the high variability of BBA properties however, is the large spread of the BBA scene spectra, which is also larger over ocean than over land.

DDA can usually be found in warm dry desert air, where clouds are created less easily anyway. Mineral aerosols are also chemically more inert and less hygroscopic, so clouds are not easily formed in desert dust aerosol plumes. Therefore the spectra of DDA scenes are more uniform than the BBA spectra.

3.4.2 Residue spectra

As a next step, the spectral behaviour of the residue with reference wavelength 380 nm, $r_{\lambda,380}$, was investigated for all the scenes containing UV-absorbing aerosols in the areas $1-4$ between June and August 1997 (see Fig. 3.5). The residues at the lowest wavelength, $r_{335,380}$, are positive (and higher than 0.5) for all areas, because this criterion was used to select UV-absorbing aerosol scenes. In Fig. 3.5 the grey-scale contour plot indicates the range of the observed residues and the solid line is the average of all residues in the three months.

Over northwest Africa (left upper panel of Fig. 3.5) the residue rapidly decreases with increasing wavelength, because the surface reflectivity increases with increasing wavelength (cf. Fig. 3.4). Furthermore, Rayleigh scattering decreases with increasing wavelength so that the bright desert surface dominates the signal.

Over southwest Africa (right upper panel) the residue slightly decreases with increasing wavelength until about 700 nm, above which the vegetation surface reflectivity starts domi-

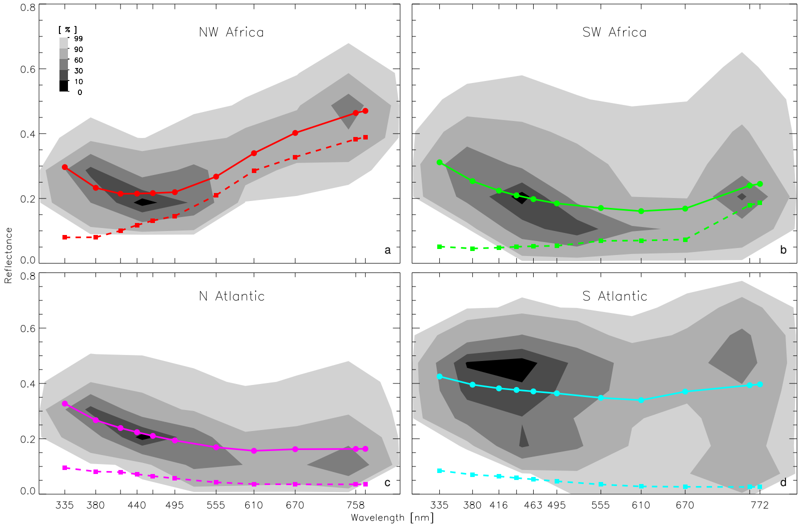

Figure 3.4: *Average GOME reflectance spectrum (solid line) and its spread (grey-scale contours) and average surface albedo (dashed line) at eleven wavelengths for UV-absorbing scenes with AAI > 0.5 in June to August 1997 from areas 1–4 in Fig. 3.1: (a) northwest Africa (red), (b) southwest Africa (green), (c) North Atlantic Ocean (magenta), and (d) South Atlantic Ocean (cyan).*

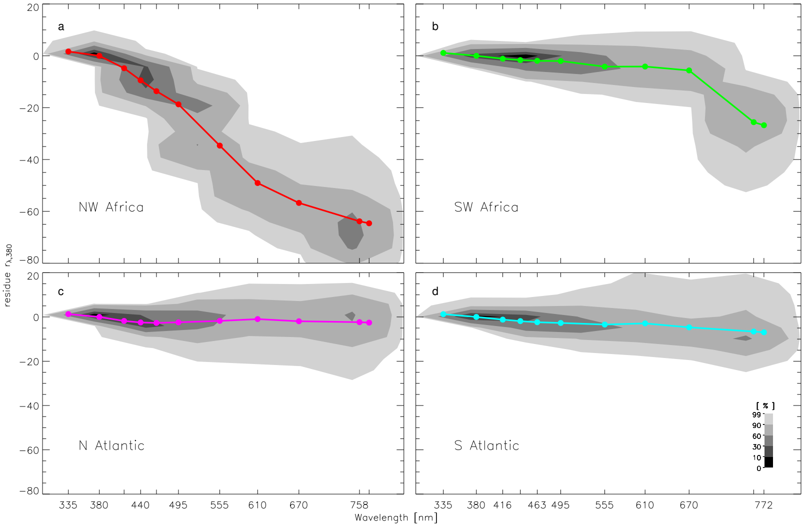

Figure 3.5: *Average GOME residue spectrum $r_{\lambda,380}$ (solid line) and its spread (grey-scale contours) at eleven wavelengths for UV-absorbing scenes with AAI > 0.5 in June to August 1997 from areas 1–4 in Fig. 3.1: (a) northwest Africa (red), (b) southwest Africa (green), (c) North Atlantic Ocean (magenta), and (d) South Atlantic Ocean (cyan).*

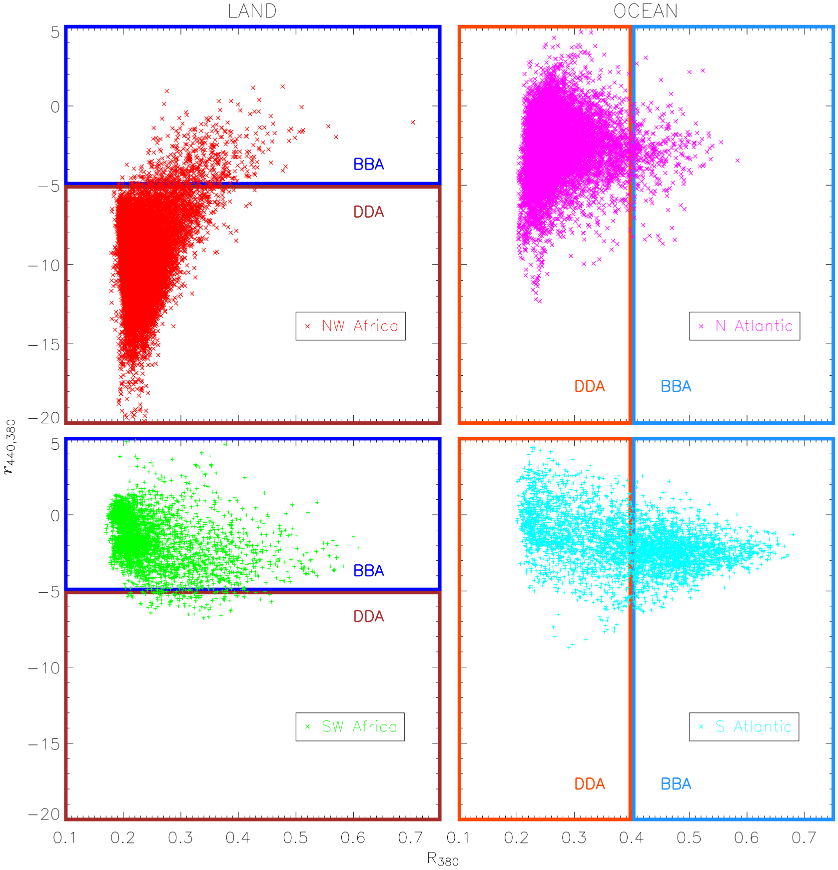

Figure 3.6: *Scatter diagrams of* $r_{440,380}$ *versus* R_{380} *for scenes with AAI > 0.5 in the areas 1 – 4 of Fig. 3.1, left from land, right from ocean areas; GOME pixels from northwest Africa are plotted in red, pixels from southwest Africa are plotted in green, GOME ocean pixels from the North Atlantic Ocean are plotted in magenta and pixels from the South Atlantic Ocean are plotted in cyan. 98 % of the red pixels have an* $r_{440,380} < -5$*; 97 % of the green pixels have an* $r_{440,380} > -5$*; 98 % of the magenta pixels have a reflectance* $R_{380} < 0.4$*; 52 % of the cyan pixels have a reflectance* $R_{380} > 0.4$.

nating the residue, sharply decreasing it.

Over the North Atlantic Ocean (left lower panel) the surface reflectivity is low for all wavelengths given and again atmospheric effects dominate. For desert dust laden scenes the residue decreases slightly until about 450 nm, after which it increases again and becomes almost zero, but the spread becomes large at longer wavelengths. Desert dust is absorbing in the UV, but as the Rayleigh effect becomes negligible at longer wavelengths any effect can influence the sensitive residue there. On average the desert dust aerosols seem to have no effect on the slope of the residue spectrum.

Over the South Atlantic Ocean (lower right panel) the residue is on average continuously decreasing, but only very slightly. The spread of scene residues is comparable for BBA and DDA scenes. At longer wavelengths the spectral behaviour of the single scattering albedo of BBA is different from that of DDA but apparently the effect is too small to be noticeable using a residue, due to the low Rayleigh reflectance at longer wavelengths. Therefore other effects, like clouds and surface albedo, dominate.

The effect of the surface albedo on the residue beyond the UV is strongly increased due to the strongly reduced Rayleigh optical thickness at longer wavelengths, and can be clearly observed in Fig. 3.5a and 3.5b. Furthermore, in the UV a spectrally independent (gray) surface albedo is a good assumption for the four areas (cf. Fig. 3.4), but at longer wavelengths the surface albedo is clearly wavelength dependent. To correct the residue for this effect, i.e. subtracting the contribution of the varying surface albedo, would imply the knowledge of a cloud fraction for each scene. The scene TOA reflectance of the cloud-free part of a pixel could be simulated using the pixel's ground albedo and radiative transfer calculations for a Rayleigh atmosphere. The cloudy part of a scene on the other hand, has a more or less wavelength independent scene albedo, which would not affect the residue calculations. So a correction scheme would imply a good cloud fraction retrieval for GOME pixels and radiative transfer calculations for the cloud-free part of the pixels. Since GOME cloud fraction retrievals are not very accurate, this was not attempted. Indeed, the strong point of the UV residue method is the simplicity of the algorithm and its insensitivity to sub-pixel cloud contamination, which makes it so useful for wide-view sensors.

3.4.3 Selection criteria

From Fig. 3.5 it might be concluded that over land DDA may be separated from BBA using the residue $r_{\lambda,380}$ at short visible wavelengths, e.g. $\lambda = 440$ nm. Similarly, from Fig. 3.4 it might be concluded that over the oceans DDA may be separated from BBA using the absolute reflectance R at e.g. 380 nm. To test this, in Fig. 3.6 four scatter diagrams are presented of the residue $r_{440,380}$ versus the reflectance R_{380} of the GOME scenes in areas 1 – 4 in Fig. 3.1 with AAI > 0.5 between June and August 1997.

Over land 98 % of the scenes from northwest Africa have an $r_{440,380}$ lower than -5, while 97 % of the scenes from southwest Africa have an $r_{440,380}$ higher than -5. The difference between the two sets of points could be increased using $r_{\lambda,380}$ with a wavelength λ higher than 440 nm (see Fig. 3.5), but this difference would be mainly caused by the surface albedo. Therefore, a selection criterion for scenes over land was defined as: All scenes with AAI > 0.5 and $r_{440,380} < -5$ are DDA scenes (lying in the brown box in Fig. 3.6) and all scenes with AAI > 0.5 and $r_{440,380} > -5$ are BBA scenes (lying in the dark blue box).

Over ocean DDA scenes with an AAI > 0.5 have on average a lower absolute reflectance than BBA scenes. 98 % of the scenes over the North Atlantic Ocean have a reflectance r_{380} lower than 0.4. However, the reflectance of BBA scenes is very variable: the reflectances of scenes from the South Atlantic Ocean vary from 0.2 to about 0.7 and only 52 % of the selected scenes have a reflectance higher than 0.4. This large spread of reflectances can also be observed in Fig. 3.4 and is probably caused by the large spread in occurrence of polluted clouds. Still, a selection criterion for scenes over the oceans was defined as: All scenes with AAI > 0.5 and $R_{380} < 0.4$ are DDA scenes (lying in the orange box in Fig. 3.6) and all scenes with AAI > 0.5 and $R_{380} > 0.4$ are BBA scenes (lying in the light blue box).

The selection criteria were applied to data from June to August 1997 (Fig. 3.7a) and November 1997 to January 1998 (Fig. 3.7b). The first period is the same period for which the selection criteria were determined, so the results in Africa are predictable, but it shows the results for the entire globe. The second period shows the result for the entire globe in a different season. All the GOME scenes with absorbing aerosols (AAI > 0.5) in the indicated periods are plotted, except sunglint scenes (see below). All land DDA scenes are plotted in brown, all land BBA scenes are plotted in dark blue, all ocean DDA scenes are plotted in orange, and all ocean BBA scenes are plotted in light blue.

In Fig. 3.7a, over north Africa in boreal summer 98 % of the desert dust pixels over land are plotted in brown and over the North Atlantic 98 % of desert dust aerosols extending over the oceans can be observed as a plume of orange pixels. The expected two percent of blue pixels are scattered through the region without a clear pattern. In southern Africa in boreal summer almost all biomass burning aerosols over land are plotted in dark blue, the three percent of erroneous brown pixels also do not seem to have a pattern. Over the South Atlantic Ocean west of Africa about half of the pixels are plotted in light blue and half of the pixels are plotted in orange. There is no clear separation of light blue and orange pixels, in particular the orange pixels are not found closer to the coast than light blue pixels, rather the contrary. This configuration might be expected if the increase in reflectance (causing the blue-orange colour difference) resulted from an increasing amount of clouds formed by ageing aerosols acting as increasingly effective cloud condensation nuclei.

Over land, outside Africa, in the boreal summer months the results are not unsatisfactory (Fig. 3.7a). In the Middle East region the pixels are correctly marked brown where DDA are expected. In western North America the majority of the land pixels are brown, although both DDA and BBA are common here. Over the Himalayas most pixels are also brown, but high AAIs over high mountainous areas must be treated with caution, because the resolution of the topography database used to determine the residue is insufficient [*De Graaf et al.*, 2005]. The same holds for the Andes. The rest of South America is mainly blue, correctly indicating BBA, which is also true for southern Africa, Indonesia and Australia.

In the winter months (Fig. 3.7b) the results are not so good. Over the Sahel region, central Africa, a large brown area borders a small elongated blue area. In view of the discussion of Fig. 3.3, this is not necessarily erroneous: in boreal winter aerosol plumes from the north travel south and it is not impossible that these aerosols are desert dust from the Sahara, bordered on the south by local BBA. However, the distinct land-sea difference of orange sea pixels and blue adjacent land pixels indicates a problem in either one or both selection criteria.

In central Australia a region is brown in both seasons, indicating desert dust, which is probably caused by specific surface conditions. In Indonesia land pixels are still blue, which is a good result and in Asia pixels are brown near desert areas and blue nearer to the coast. This is an interesting result. BBA are very common in China and east Asia and recent evidence suggests a blackening of DDA due to mixing with soot particles produced over the industrial/urban areas of China, as DDA moves from the central Asian desert areas to the eastern coastal areas, changing the spectral characteristics of the mineral aerosols [*Kim et al.*, 2005]. A spectral change of microphysical properties might induce a change of spectral residue. However, in general the results over land will be determined by the surface reflectance.

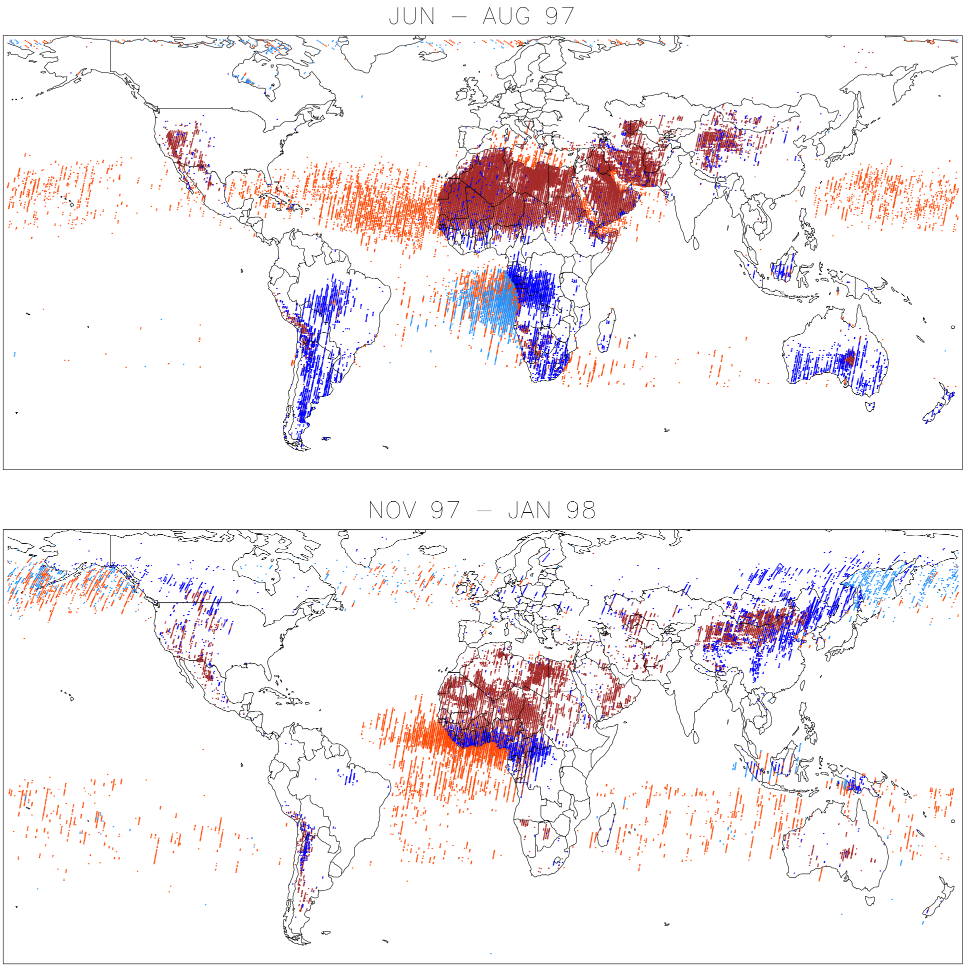

Figure 3.7: *a) World plot of all GOME pixels from June 1997 to August 1997 having AAI > 0.5 (containing UV-absorbing aerosols). Land pixels with a residue $r_{440,380}$ lower than -5 are plotted in brown (assumed to be desert dust aerosols), land pixels with a residue $r_{440,380}$ greater than -5 are plotted in dark blue (assumed to be biomass burning aerosols), ocean pixels with a reflectance at 380 nm R_{380} lower than 0.4 are plotted in orange (assumed to be desert dust aerosols) and ocean pixels with a R_{380} higher than 0.4 are plotted in light blue (assumed to be biomass burning aerosols). b) Same as a), but from November 1997 to January 1998.*

Over the oceans, stripes of orange pixels can be observed over the Pacific and the Atlantic in both boreal summer and winter. In the winter the stripes are shifted to the southern hemisphere to where the sun is overhead. These pixels were assumed to be caused by sunglint, since sunglint causes [*De Graaf and Stammes*, 2005] and GOME AAI pixels were not initially corrected for sunglint. However, to exclude sunglint all east pixels where sunglint could be present have been removed and can thus not explain the orange pixels.

South of Alaska in boreal winter about half of the UV-absorbing pixels are marked blue, indicating BBA, half are orange, indicating DDA. Any absorbing aerosols in this area are caused by biomass burning, but the large spread of reflectances of BBA scenes makes an accurate distinction between DDA and BBA impossible. Orange pixels are ambiguous, but according to the analysis of African summer aerosol scenes, light blue pixels indicate BBA. So the pixels east of Asia over the Pacific in boreal winter are BBA.

3.5 Conclusions

GOME $r_{335,380}$ residue data are useful to study multi-year time series and trends of phenomena connected to aerosols and clouds globally or in a certain area. They can be used to monitor seasonal cycles or individual aerosol events. For example, the exceptionally large amount of biomass burning events in Indonesia in 1997, caused by El Niño, was illustrated with a regionally averaged residue. The seasonal variation of desert dust and biomass burning events in Africa was shown to be related to the African monsoon.

In northern Africa near the Sahara and over the adjacent North Atlantic Ocean desert dust is very common and can be found year-round. In southwest Africa biomass burning events occur regularly in the dry season. These areas were chosen to study the spectra of aerosol laden scenes in order to find spectral fingerprints of different aerosol types.

Dust storms are most severe in the boreal summer in northern Africa, when the sun is overhead and wind speeds are peaking. This can be observed in the residue, which has a clear seasonal variation, peaking in the boreal summer. In boreal winter the dust storms are less severe and frequent but are still among the most intense on the globe. The surface albedo in the visible and near-IR is very high over deserts, therefore UV methods are necessary to study desert dust aerosols. The reflectance spectra of desert dust scenes over land decrease with increasing wavelength in the UV and increase with increasing wavelength in the visible and near-IR due to the increasing surface albedo. Over the oceans the surface albedo is low, and the absolute reflectance of desert dust scenes is low at all wavelengths and decreasing with increasing wavelength. Desert dust aerosols are chemically inert and have a low hygroscopicity, therefore the spectra of desert dust scenes have a small spread and desert dust can be classified spectrally as one type.

Biomass burning aerosols are common in the austral spring over southwest Africa and the adjacent South Atlantic Ocean, which is the local dry season. In the wet season no fires and no aerosols are found in this area. The average spectral behaviour of biomass burning scenes is slightly decreasing with increasing wavelength in the UV and visible and slightly increasing with increasing wavelength in the near-IR, due to the increasing reflectance of vegetation in this spectral range. Biomass burning aerosols are highly variable in chemical and physical properties, depending on fuel type and age of the aerosols. As a result, the variation of the biomass burning aerosol scenes spectra is very large. Over oceans this effect is even more pronounced, as biomass burning aerosols over oceans are by definition aged aerosols, having their origin over land. This is expressed in the spectra of biomass burning aerosols over oceans, which have the largest spread of spectra presented in this paper. The high variability of biomass burning aerosol properties makes it hard to classify biomass burning aerosols spectrally as one distinct type.

The residue method for the detection of UV-absorbing aerosols is suitable for application over both land and oceans. An attempt was made to extend the method using residues at longer wavelengths, i.e. in the visible and the near-IR. However, due to the high surface albedo over land, especially over deserts, and the decreased Rayleigh signal at higher wavelengths, the surface albedo completely determines the result of the residue calculations, whereas in the UV aerosol effects are more pronounced. Using a reference wavelength λ_0 beyond the UV affects all residue calculations, whereas a reference wavelength in the UV and a second wavelength λ in the visible or near-IR merely show surface effects. Over oceans this is less a problem, but the spectral dependence of residues of DDA and BBA over oceans was found to be more or less identical. However, over oceans a difference of absolute reflectances was observed between DDA and BBA scenes.

The above considerations led to an aerosol type classification of desert dust aerosols and biomass burning aerosols using different selection criteria over land and over oceans. Over land the residue $r_{440,380}$ and over oceans the reflectance at 380 nm was used to discriminate between BBA and DDA scenes with AAI > 0.5. Over land this means a characterisation on the basis of geographical information, because actually vegetated land is distinguished from desert surfaces: the surface albedo dominates the residue even at these wavelengths. Over the oceans the absolute value of the reflectances at 380 nm of BBA scenes is highly variable, and the current selection criterion misses about 48 % of the BBA scenes, classifying them as DDA scenes. An aerosol type classification on the basis of the above criteria is of limited use. However, the analysis of African summer aerosol scenes showed that over oceans high reflectance aerosol scenes are caused by biomass burning aerosols.

More detailed spectra of DDA scenes, as e.g. provided by SCIAMACHY, may help to identify spectral fingerprints of desert dust. The high variability of biomass burning aerosols suggests that a more elaborate study of cloud contaminated and cloud-free BBA scenes is needed to gain information on the actual spectral fingerprints of the biomass burning aerosols themselves.

Acknowledgements This work was financed by the Dutch Space Agency (NIVR) SCIAMACHY validation project and DAEDALUS, project number EVK2-CT-2002-00174. Deutscher Wetterdienst (DWD, National Meteorological Service of Germany) is acknowledged for the use of their precipitation data.

4

SCIAMACHY Absorbing Aerosol Index – calibration issues and global results from 2002 – 2004

Abstract

The validity of the Absorbing Aerosol Index (AAI) product from SCanning Imaging Absorption SpectroMeter for Atmospheric CartograpHY (SCIAMACHY) is discussed. The operational SCIAMACHY AAI product suffers from calibration errors in the reflectance as measured by SCIAMACHY and neglect of polarisation effects in the AAI computational algorithm. Therefore, the AAI product was recalculated, compensating for the errors, with reflectance data from the start of measurements of SCIAMACHY until December 2004. Appropriate correction factors were determined for the UV to correct for the radiometric error in the SCIAMACHY reflectances. The algorithm was provided with LookUp Tables in which a good representation of polarisation effects was incorporated, as opposed to the LookUp Tables of the operational product, in which polarisation effects were not accounted for. The results are presented, their validity discussed, and compared to the operational product and independent AAI data from the Total Ozone Mapping Spectrometer (TOMS). The AAI is very sensitive to calibration errors and can be used to monitor calibration errors and changes. The AAI is sensitive to sunglint and a correction flag used for the AAI is presented. From 2004 onwards, the new SCIAMACHY AAI is suitable to add to the continuation of the long-term AAI record. Important changes in the long-term AAI record due to instrument and algorithm changes are highlighted. Recommendations are given for improvement of the operational AAI product.

M. de Graaf, P. Stammes (2005), *ACP 5*, SRef-ID: 1680-7324/acp/2005-5-2385

4.1 Introduction

The AAI is a dimensionless index indicating the presence of ultraviolet (UV)-absorbing aerosols in the Earth's atmosphere [*Herman et al.*, 1997; *Torres et al.*, 1998; *De Graaf et al.*, 2005]. The AAI has been used for a long time in remote sensing to indicate UV-absorbing aerosols, like desert dust [e.g. *Chiapello et al.*, 1999; *Alpert and Ganor*, 2001; *Pandithurai et al.*, 2001; *Spichtinger et al.*, 2001; *Prospero et al.*, 2002; *Moulin and Chiapello*, 2004] and biomass burning aerosols [e.g. *Hsu et al.*, 1996; *Gleason et al.*, 1998; *Hsu et al.*, 1999a; *Duncan et al.*, 2003; *Darmenova et al.*, 2005] over both land and oceans.

Initially developed as an error estimate in the TOMS ozone retrieval algorithm [*Herman et al.*, 1997; *Torres et al.*, 1998], the AAI records have become the longest records of global aerosol measurements available. Starting with Nimbus–7/TOMS in 1978, American TOMS instruments have provided daily global aerosol maps continuously for over 25 years, with a data gap only between May 1993 and June 1996. From 1995, the European ERS–2/GOME provided additional and independent AAI information, adding to the continuity of the AAI record and validity of the AAI as an aerosol detection quantity [*De Graaf et al.*, 2005]. Now, Envisat/SCIAMACHY results will be added to the AAI records.

Operational data production of SCIAMACHY started at the end of July 2002. Several improvements and changes of the data processor and key data characteristics followed in the subsequent two and a half years. In this paper, the operational AAI product of this period is presented briefly.

Improper characterisation of the instrument's response functions (key data) results at the moment in calibration errors in the measured reflectances of SCIAMACHY of up to 20%. This yields AAI errors in the order of 4-6, which is about 100% of the signal [*De Graaf and Stammes*, 2002]. In this paper, correction factors for the reflectances are used and their validity for the calculation of AAIs is investigated.

The operational AAI product is calculated using pre-calculated LookUp Tables (LUTs) of theoretical reflectances in a cloud-free and aerosol-free atmosphere. These LUTs were constructed with a radiative transfer model [*Spurr and Balzer*, 2000] which neglected polarisation effects. Here, the AAI is further improved using LUTs in which linear polarisation is accounted for. The effects of this are presented and discussed.

The result of the changes mentioned above is an off-line AAI algorithm using calibrated SCIAMACHY reflectances, off-line LUTs, and additional calibration constants, producing SCIAMACHY scientific AAIs. All off-line products developed after launch of the ENVISAT spacecraft are termed scientific products, to distinguish them from the operational products owned by ESA, and can be found at `http://www.sciamachy-validation.org`. The scientific AAI is presented and investigated, and compared to the operational product and other independent aerosol data.

This chapter continues with a brief summary of the theory behind the AAI (section 4.2). The characteristics of SCIAMACHY are described (section 4.3), followed by a description of the operational AAI product and its shortcomings (section 4.3.1). Improvements for an off-line product are discussed, leading to a new algorithm for a scientific AAI (section 4.3.2), the results of which are laid out in section 4.4. The spatial and temporal patterns of global aerosols found in the data are discussed and compared to TOMS AAI data. Sunglint and other problems in the data, related to the specific definition of the AAI, are pointed out.

Finally, the results are discussed and some recommendations for future improvements are given (section 4.5).

4.2 Absorbing Aerosol Index

The Absorbing Aerosol Index (AAI) is a measure for the spectral contrast between the reflectance of the real atmosphere-surface system, that may be affected by the presence of UV-absorbing aerosols, and that of a modelled atmosphere-surface system, that does not contain UV-absorbing aerosols. The modelled atmosphere may contain scatterers (Rayleigh scattering molecules, non-absorbing aerosols and cloud particles, as well as absorbing gases) and is bounded below by a surface with a wavelength independent reflectivity. The AAI is defined as the positive part of the residue, where the residue r defined as [*Herman et al.*, 1997]

$$r_\lambda = -100 \cdot \left\{ {}^{10}\log(\frac{R_\lambda}{R_{\lambda_0}})^{\text{meas}} - {}^{10}\log(\frac{R_\lambda}{R_{\lambda_0}})^{\text{Ray}} \right\}. \tag{4.1}$$

R_λ is the reflectance at a wavelength λ. R^{meas} is the measured reflectance in the atmosphere with aerosols, as opposed to a calculated reflectance in an aerosol-free atmosphere R^{Ray}, with only Rayleigh scattering and absorption by molecules and surface reflection and absorption. The reflectance is defined as $R = \pi I/(\mu_0 E_0)$, where I is the radiance at the top of the atmosphere (TOA), E_0 is the solar irradiance at TOA perpendicular to the direction of the incident sunlight and μ_0 is the cosine of the solar zenith angle θ_0.

If the surface albedo A_s for the Rayleigh atmosphere calculation is chosen so that

$$R^{\text{meas}}_{\lambda_0} = R^{\text{Ray}}_{\lambda_0}(A_s), \tag{4.2}$$

where λ_0 is a reference wavelength, Equation (4.1) can be reduced to

$$r_\lambda = -100 \cdot {}^{10}\log(\frac{R^{\text{meas}}_\lambda}{R^{\text{Ray}}_\lambda}), \tag{4.3}$$

where R^{Ray}_λ is calculated for surface albedo $A_s(\lambda_0)$, so the surface albedo is assumed to be constant in the range $[\lambda, \lambda_0]$. In this paper the traditional residue wavelength pair, $\lambda = 340$ nm and $\lambda_0 = 380$ nm, is adopted.

On the assumption that the atmosphere is bounded from below by a Lambertian surface, which reflects incident radiation uniformly and unpolarised in all directions, the surface contribution to the reflectance at TOA can be separated from that of the atmosphere [*Chandrasekhar*, 1960]:

$$R(\mu, \mu_0, \phi - \phi_0, A_s) = R_0(\mu, \mu_0, \phi - \phi_0) + \frac{A_s t(\mu) t(\mu_0)}{1 - A_s s^*}. \tag{4.4}$$

The first term, R_0, is the path radiance, which is the atmospheric contribution to the reflectance. The second term is the contribution of the surface with an albedo A_s. t is the total atmospheric transmission, s^* is the spherical albedo of the atmosphere for illumination from below, μ is the cosine of the viewing zenith angle θ and $\phi - \phi_0$ is the relative azimuth angle.

The path radiance R_0 is calculated with LUTs of $a_i(\mu, \mu_0)$, $t(\mu)$ and s^* for all wavelengths used. Then the surface albedo A_s in Equation (4.2) can be found from

$$A_s = \frac{R - R_0}{t(\mu)t(\mu_0) + s^*(R - R_0)}, \tag{4.5}$$

by replacing R by $R^{\text{meas}}_{\lambda_0}$ in Eq. (4.5). Note that this equation allows negative surface albedos, which occurs for highly absorbing (aerosol) layers.

Sensitivity studies show [*Torres et al.*, 1998; *De Graaf et al.*, 2005] that UV-absorbing aerosols produce an effect on the spectrum that cannot be simulated with a pure Rayleigh atmosphere and an adjusted surface albedo, creating large, positive residues, even for wavelength independent aerosol refractive indices. Scattering effects are much better represented with a Rayleigh atmosphere and underlying adjusted surface albedo, yielding small, negative residues. The AAI is therefore defined as the positive part of the residue, thereby filtering clouds and scattering aerosols.

4.3 SCIAMACHY

SCIAMACHY is part of the payload of the European ’Environment Satellite’ (Envisat), launched on 01 March 2002 onboard an Ariane-5 launch vehicle from the Guyana Space Centre into a polar orbit at about 800 km altitude, with an equator crossing-time of 10:00 AM (local time) for the descending node, orbiting the Earth every 100 minutes. SCIAMACHY is a spectrometer designed to measure sunlight, transmitted, reflected and scattered by the Earth’s atmosphere or surface in the ultraviolet, visible and near-infrared wavelength regions (240–2380 nm) at a moderate spectral resolution of 0.2–1.5 nm [*Bovensmann et al.*, 1999]. The radiance is observed in two alternating modes, nadir and limb, yielding data blocks called states. The nadir state swath is approximately 960×490 km^2, and it is scanned from east to west in four seconds by rotation of one of the two internal mirrors. The result is a subdivision of the states into groundpixels of approximately 60×30 km^2 at the optical integration time (IT) of 0.25 s. Longer integration times of 0.5 s and 1.0 s also occur, yielding groundpixels of 120×30 km^2 and 240×30 km^2. Even longer integration times occur, but they will not be considered here. The extra-terrestrial solar irradiance is measured each day, once per 14 orbits.

4.3.1 Operational AAI algorithm

SCIAMACHY’s operational AAI product (L2-AAI) is calculated directly after downlinking of the data in the so-called near-real time level 1 (L1) to level 2 (L2) processing step. The processing steps are described in detail in *Balzer et al.* [2000]. A brief summary is given here, to highlight the most important differences with the scientific AAI product, described below.

The reflectance is determined in the level 0 (L0) to L1 processing step for each groundpixel from channel 2, cluster 9, which contains the spectrum from 320.14 nm to 391.76 nm. Common normal mode ITs in cluster 9 are 0.25 s, 0.5 s and 1.0 s. These are constant within states, but can vary within orbits. The AAI is computed using the reflectances at 340 nm and

380 nm. A Rayleigh reflectance is determined from a pre-calculated LUT, for each pixel, dependent on geometry and surface height. The LUT has inputs for 11 reference heights from 0 to 5 km and 8 reference albedos from 0.0 to 0.9. The solar zenith angle θ_0 must be between 15° and 85° and the viewing zenith angle θ lower than 35°, otherwise no AAI is calculated.

The L2-AAI suffers from two major flaws. Firstly, the original LUTs were calculated with the use of a scalar radiative transfer model, so that polarisation was not accounted for in the Rayleigh scattering computations. When the LUTs were calculated, only a scalar version of the model, LIDORT [*Spurr et al.*, 2001], was available. The residue calculations are sensitive to errors in the reflectances, see Fig. 4.1a. This figure shows the residue in a modelled Rayleigh atmosphere where polarisation has not been accounted for, for different geometries. In a Rayleigh atmosphere the residues should be exactly zero. The errors in the reflectance in the modelled atmosphere are of the order of about 10 – 15 %, yielding erroneous residues of a maximum of -4 to 3.5. New LUTs have been created using a model that accounts for polarisation effects.

Secondly, the reflectances as measured by SCIAMACHY are underestimated in the UV by 10 – 20 %, as reported by several workers [e.g. *Tilstra et al.*, 2004]. This results in an offset of the AAI of about 4-6 [*De Graaf et al.*, 2004], which is of the order of the maximum expected AAI. To correct for these errors, a scientific AAI algorithm was constructed, which uses corrected SCIAMACHY L1 data (calibrated reflectances).

4.3.2 Scientific AAI algorithm

The scientific AAI (SC-AAI) is calculated off-line, i.e. after L1 data have been received via satellite link at the Royal Netherlands Meteorological Institute (KNMI). The data are calibrated and radiances and irradiances are extracted to determine the reflectances at 340 nm and 380 nm. These reflectances are averaged over a one nm wide window. After this, the reflectances are corrected for the underestimation of the reflectance by SCIAMACHY. This correction consists of a simple multiplication of the reflectances by a constant factor. Several factors were tried and the best multiplication factors were 1.210 for R_{340} and 1.130 for R_{380} [*Tilstra et al.*, 2004]. Note that different multiplication factors will lead to a linear shift in the resulting AAI [*De Graaf et al.*, 2004, 2005].

The corrected reflectances are used in Equations 4.2 and 4.3. The inversion process and the LUTs used therein are described in detail in *De Graaf et al.* [2005]. The LUTs were created using the Doubling-Adding KNMI (DAK) radiative transfer model [*De Haan et al.*, 1987], in which polarisation is accounted for. The surface albedo is calculated directly using Equation 4.5.

The changes are illustrated in Fig. 4.1b. This figure shows the scientific residue compared to the L2-AAI for 5 states of orbit 10969 on 5 April 2004 over the Sahara, where a dust plume was present at that time. Note that the scientific residue is the quantity that is determined for all SCIAMACHY pixels. The SC-AAI is the quantity that signals the presence of aerosols, or other absorbing effects, by filtering of negative residues. The figure shows the offset of 4-6 of the L2-AAI compared to the scientific residue, caused by the underestimation of the reflectances. Moreover, it shows that the offset differs by about two for east and west pixels, which is caused by the neglect of polarisation in the L2-AAI. This behaviour is found throughout the data.

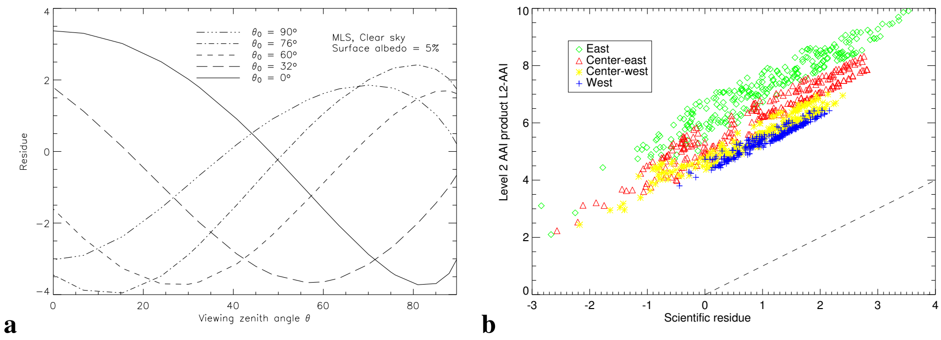

Figure 4.1: *(a) The residue in a modelled Rayleigh atmosphere where polarisation has not been accounted for as a function of viewing and solar zenith angles. Relative azimuth angle is zero. (b) The scientific residue compared to the operational level-2 AAI data for orbit 10969, states 5–9. The colours refer to pixels with approximately the same viewing geometry. The first four pixels of* 30×60 *km*^{2} *in a forward swath are called East pixels, the next 4 Centre–east, the next 4 Centre–west and the last 4 West pixels. The dashed line is the one-to-one line.*

4.4 Results

The L2 data can be obtained from the European Space Agency (ESA). The scientific data are available at `http://www.temis.nl`. Both gridded daily data and gridded monthly means are available as well as daily and monthly pictures. The SC-AAI was determined from all SCIAMACHY L1 data available from 22 July 2002 to 31 December 2004.

The calibration processor of SCIAMACHY has regularly been updated over the last two and half years. This is reflected in the AAI data, which is very sensitive to calibration errors. In that way the AAI can be used as a monitor for calibration errors and improvements. This is illustrated in Fig. 4.2, which shows the number of pixels available at KNMI for the SC-AAI calculation, the processor version number that processed the L1 data of a certain period, and the results.

The uppermost panel and the colour code show the L1 processor version number, which reflects the status of the calibration process. Processor version 3.51 was the default when the first data became available. The processor was steadily updated to version 5.04 in December 2004, but reprocessed data have replaced older versions frequently (the newest available data was always used). The lower panel shows the number of residues that have been determined in a day. Because a residue is computed for all pixels which have a reflectance at 340 nm and 380 nm, this is a good measure for the amount of SCIAMACHY data of a certain day available at KNMI. The centre panel of Fig. 4.2 shows the scientific residue, averaged daily over the globe, as the normal black line and some isolated dots. The bold black line is its 30 day running mean.

The daily global scientific residue was highly erratic in the beginning, ranging from −7 and lower to more than 0.5. This is due to the very few number of measurements available at that time and the poor status of the calibration. Often, only one orbit was available on a day and the measurements frequently gave poor results. In 2004 the results improved considerably as the spread in the measurements decreased.

The monthly mean residues, averaged over the globe, are given as black diamonds. They are not exactly the same as the 30 day running mean, mainly because the monthly means are first monthly averaged per gridbox and then averaged over the globe. In 2004 the monthly mean maps of SC-AAI show results in the expected range of −2 to −1.

The L2-AAI, shown in purple, correlates well with the scientific residue, but note that the y-axis is shifted by +6. The correction factors used to correct the reflectances to compute the SC-AAI cause a linear shift of the residue. The differences that remain between the SC-AAI and L2-AAI are due to the neglect of the polarisation in the Rayleigh atmosphere calculations and different sensitivities to processor changes.

An example of SCIAMACHY SC-AAI measurements is given in Fig. 4.3, which shows the SC-AAI on 16 June 2204. The daily global coverage of SCIAMACHY is illustrated, which is only 1/6th of the globe. The black rectangles are the outlines of the nadir states. Only within these states can an AAI be derived. This resolution makes daily monitoring of aerosols difficult, but the data is provided daily to offer the best possible resolution to end-users. The irregularly spaced orbits show that not all orbits were available, which was often the case (see Fig. 4.2, lower panel).

On 16 June 2004 desert dust aerosols can be found over northern Africa, the Middle East region, and parts of China, which are very common in these areas in June. Over the northern Atlantic low SC-AAI values can be observed in a number of states, with clear parts in the east pixels of some states. These are desert dust plumes extending over the Atlantic, with sun glint (see below) pixels removed from the data. Also over the Mediterranean Sea and the northern Pacific some remnants of sun glint can be observed.

4.4.1 Sun glint

Sun glint is a problem that occurs throughout the year. Sun glint generates a high SC-AAI signal in the eastern pixels of SCIAMACHY. If the sun glint angle is defined as the angle for which sun glint would occur if an ocean was a perfect mirror, the deviation from this angle $\Delta\Omega_{\mathrm{glint}}$ can be defined for each pixel as

$$\cos(\Delta\Omega_{\mathrm{glint}}) = \cos\theta_0 \cos\theta + \sin\theta_0 \sin\theta \cdot \cos(\phi - \phi_0). \tag{4.6}$$

Because the roughness of the oceans spreads out the sun glint signal, pixels having a sun glint deviation angle $\Delta\Omega_{\mathrm{glint}}$ larger than zero can also be affected by sun glint. The geometrical sun glint condition was defined as the geometry for which the sun glint deviation angle was lower than 12°. A pixel satisfied the sun glint condition when it satisfied the geometrical sun glint condition and had an ocean as underlying surface. The underlying surface was determined using the 0.25° × 0.25° GTOPO elevation database with an ocean flag. Pixels satisfying the sun glint condition were removed.

The residues of all pixels satisfying the sun glint condition of three months (October – December 2004) were compared to all land pixels satisfying the geometrical sun glint condition. The average residue of the sun glint pixels was −0.38 and that of the land pixels was −1.38. The average residue for pixels not satisfying the geometrical sun glint condition was −1.56 over both land and ocean. This was considered a confirmation that the high residue in ocean sun glint pixels was anomalous and caused by sun glint.

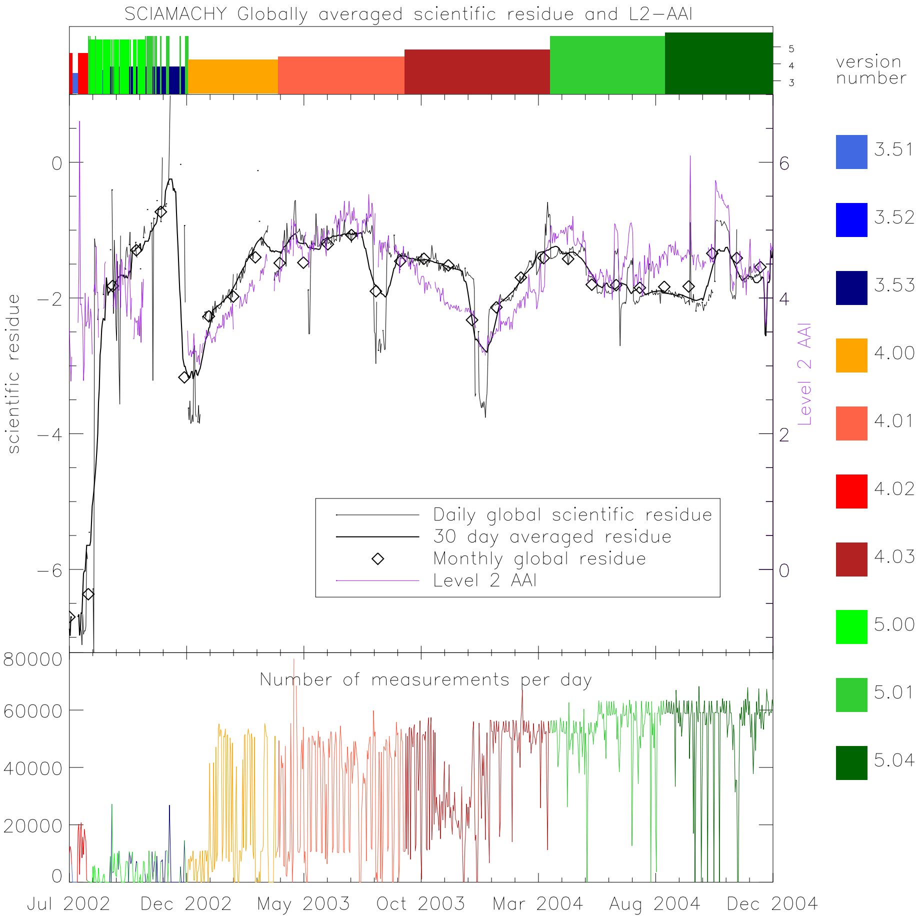

Figure 4.2: *Statistics of the off-line data as a function of time for the entire measurement period, 22 July 2002–31 December 2004. The uppermost panel and the colour codes denote the L1 processor version number of the data of a certain period. The central panel shows the data, averaged per day over the entire globe. The normal black line and individual points show the daily global averaged scientific residue. The bold black line is its 30 day running mean. The black diamonds show the monthly mean scientific residue. The purple line shows the L2-AAI (Note that the right axis is shifted by +6). The lower panel shows the number of pixels that where available for the scientific residue calculations per day.*

The effect of using a sun glint deviation angle $\Delta\Omega_{\mathrm{glint}}$ lower than 12° is illustrated in Fig. 4.4. Figure 4.4a shows the sun glint deviation angle for SCIAMACHY pixels on 12 December 2004 over the Indian Ocean, Indonesia and Australia, and the south–west Pacific. The pixels satisfying the sun glint condition are marked in red, other ocean pixels' sun glint deviation angles are marked according to the continuous colour scale. Figure 4.4b shows the SC-AAI when no sun glint mask is applied. Several bands with high SC-AAI values can be

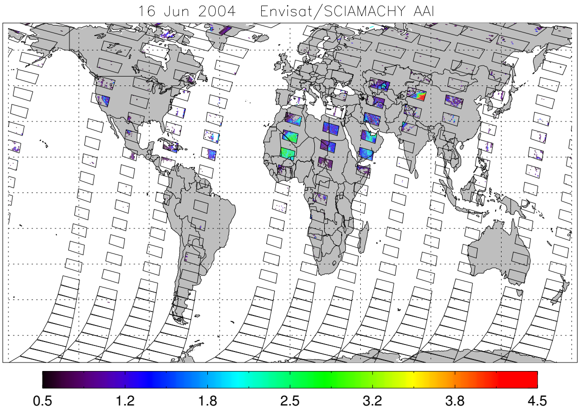

Figure 4.3: *Global SCIAMACHY SC-AAI on 16 June 2004. The black rectangles are the outlines of the nadir states.*

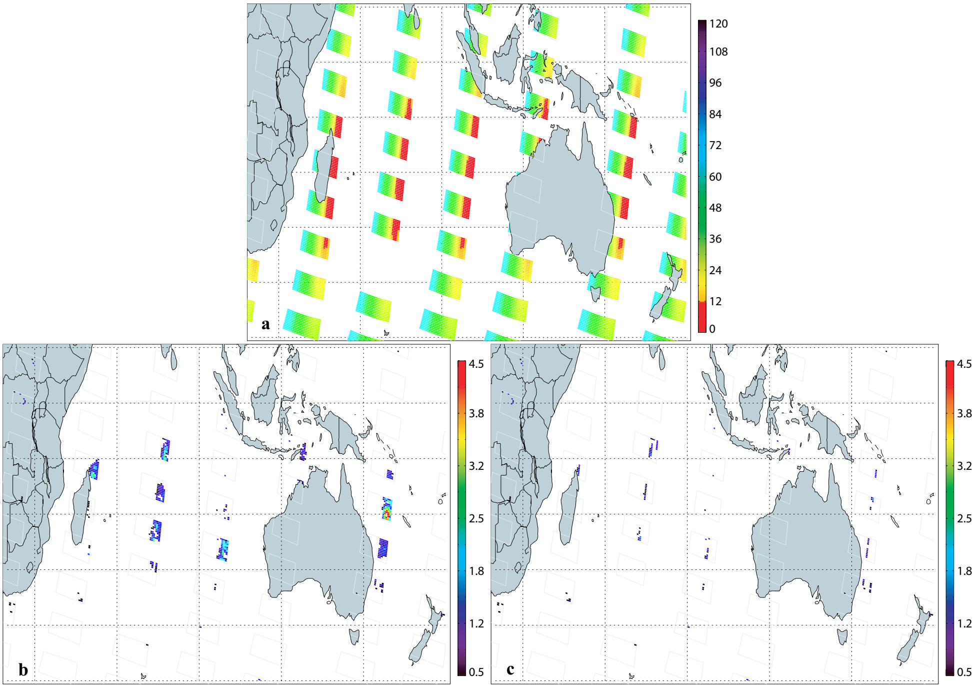

Figure 4.4: *SCIAMACHY SC-AAI on 12 December 2004 over the Indian Ocean, Indonesia and Australia, and the south-western Pacific.* **(a)** *Sun glint deviation angle of SCIAMACHY ocean pixels. The sun glint deviation angle has a smooth scale, but all pixels satisfying the sun glint condition, i.e. having a sun glint deviation angle lower than 12°, are marked in red.* **(b)** *SC-AAI without sun glint mask.* **(c)** *SC-AAI with all ocean pixels with a sun glint deviation angle lower than 12° removed.*

distinguished in the eastern pixels over the oceans, but not over land. Applying the 12° sun glint deviation angle mask removes most of the pixels with high signals (Fig. 4.4c). A more severe sun glint mask, e.g. removing all ocean pixels with sun glint deviation angles lower than 15°, improves the picture on 12 December 2004, because it is not likely that any aerosol events caused the high signals on this day in the area shown. But since the sun glint mask does not discriminate between sun glint and aerosol events, the sun glint mask will remove pixels with aerosol information for situations with aerosol plumes over the oceans. To reduce this problem the condition was set strict enough that sun glint is removed from most of the pixels, leaving only some small remnants in clear sky pixels with sun glint deviation angles close to 12°. These remnants will not easily be mistaken for artificial aerosol events. On the other hand, the condition is not so strict that it will remove all aerosol pixels from aerosol plumes over oceans. The locations of pixels satisfying the sun glint condition are easily recognised and the gaps which the sun glint mask produces are small enough so they will not greatly reduce the signal caused by aerosols.

4.4.2 Spatial and temporal patterns

Three-monthly means of SC-AAI in 2004 are presented in Fig. 4.5 to show the most persistent aerosol sources and seasonal variations. The range of the AAI data plotted in Fig. 4.5 is from −0.4 to 2.5. Theoretically, for a well-calibrated AAI positive values should indicate absorbing aerosols. In reality some fine-tuning is needed to establish the right threshold. Figure 4.2 shows that the average of the scientific residue is about −2, lower than the global average GOME residue in the period 1995 – 2000 [*De Graaf et al.*, 2005], which was −1.2. The correction factors for the SCIAMACHY reflectance offset are not entirely correct, causing the residue to be smaller than usual (see section 4.4.4). Therefore, the lower plotting boundary was lowered to −0.4.

The first panel of Fig. 4.5 is the average of the monthly means of January, February and December (JFD) of 2004. Only a few persistent aerosol sources over the Sahara show up in the plot. As was shown in Fig. 4.2, the average AAI in the first two months of 2004 was very low, probably due to incorrect calibration. Still, the southern part of the Sahara shows some signal.

The next panel in Fig. 4.5 shows the boreal spring (MAM) main aerosol sources. As was found with GOME [*De Graaf et al.*, 2005], very persistent aerosol sources are found over northern Africa and the Middle East. SCIAMACHY also detects the aerosol plumes north-west of India, which were never detected by GOME because of its data storage problem in that region.

In the summer (JJA) the typical desert dust plume over the Sahara, extending far over the northern Atlantic, is clearly present. This is one of the most prominent features of the AAI and can be observed in all summer months. Also the biomass burning aerosol plume west of Angola, that was found every summer of 1995 – 2000 by GOME, is present. The aerosol plumes over the northern Sahara and the Middle East are strongest and most persistent, as a result of the most northerly position of the Inter-Tropical Convergence Zone (ITCZ) at that moment.

In autumn (SON) all aerosol plumes present in the summer are weaker, but still discernible. A clear plume is visible over the north-west of Australia. This plume frequently showed up in the GOME data as well, but was difficult to distinguish from the noise, because of the large footprint of GOME (40×320 km^2). SCIAMACHY data however clearly show a persistent aerosol source in this area. Possible sources might be desert dust from Australia or biomass burning from Indonesia and Australia or both.

4.4.3 Comparison with TOMS AAI

The SCIAMACHY SC-AAI was compared to the TOMS AAI. However, the TOMS AAI is different from the SCIAMACHY AAI in several ways. The definition of the TOMS AAI has changed with the introduction of version 8 data (2004), which has increased the sensitivity of the TOMS index, compared to that of version 7 data. This fact is not very widely known, but has quite large implications for the interpretation of the index. Also, the calibration differences of the instruments have an impact on the behaviour of the indices. Before the indices are compared, the different definitions are given and the differences in sensitivities will be highlighted.

Two wavelengths in the UV are used to calculate the AAI (Equation 4.1). In the definition of the V7 TOMS AAI (also used for SCIAMACHY), the reference wavelength λ_0 is the largest of the two wavelengths (360 nm for TOMS and 380 nm for SCIAMACHY). In the definition of the V8 TOMS AAI this has changed and the reference wavelength is the shortest wavelength (331 nm for TOMS). This has increased the sensitivity of the index, see Fig. 4.6 where the monthly averaged TOMS V8 AAI is compared to the monthly averaged TOMS V7 AAI. The V8 AAI is about $1.5 - 2$ times as sensitive as the V7 AAI and correlates nonlinearly. Also the V7 AAI was valid only from 0.7 upward, to indicate the presence of absorbing aerosols, in V8 this threshold has changed to zero (P.K. Bhartia, pers. comm.). Note that the majority of the points in Fig. 4.6 are on the line where V7 TOMS AAI is zero. In the V7 definition this meant that there would be no absorbing aerosols, while all V8 pixels with AAI larger than zero now do indicate absorbing aerosols.

The reason for the increased sensitivity is the larger optical thickness at the lower wavelength (about 60 % larger at 331 nm compared to 360 nm). In the AAI method all atmospheric scattering and absorbing effects are modelled with an adjusted surface albedo under a Rayleigh atmosphere. At the lower wavelength the atmospheric effects are relatively larger and the retrieved surface albedo is affected more strongly. The relationship between the V7 and the V8 AAI is nonlinear, because the reflectivity at the reference wavelength is a nonlinear function of geometry and atmospheric conditions. Nonlinear relationships between AAIs with different reference wavelengths was also found by *De Graaf et al.* [2005].

Also note that the sensitivity of the TOMS AAI changes with the different TOMS instruments since different instruments haD different channels. Currently, EP/TOMS uses channels in the UV at 331 nm and 360 nm. Before this (i.e. data from before 1996), TOMS instruments had channels in the UV at 340 nm and 380 nm. The same is true for GOME and SCIAMACHY; for GOME the wavelengths used were 335 nm and 380 nm and for SCIAMACHY the wavelengths were 340 nm and 380 nm, but as long as the reference wavelength is unchanged the relationship is linear.

Note that all TOMS AAI data from 1978 to present are reprocessed according to the V8 definition. So all the data presently available on the Internet are $1.5 - 2$ times as sensitive as those published in papers so far. The definition of SCIAMACHY AAI is the same as the

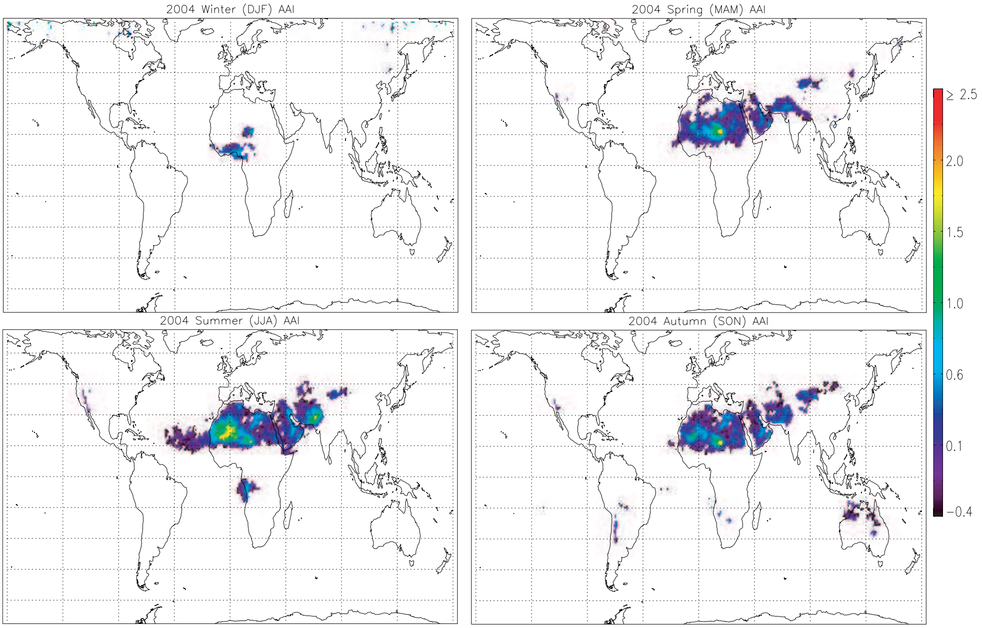

Figure 4.5: *Maps of the seasonally averaged global SC-AAI. Shown are the mean SC-AAI in January, February and December of 2004 (Winter), mean SC-AAI in March, April and May 2004 (Spring), mean SC-AAI in June, July and August 2004 (Summer) and mean SC-AAI in September, October and November 2004 (Autumn).*

original TOMS V7 AAI, so the results from SCIAMACHY (and also its predecessor GOME) are comparable with TOMS V7 AAI and the results of the papers that explain and investigate the sensitivity of the AAI [*Herman et al.*, 1997; *Torres et al.*, 1998; *De Graaf et al.*, 2005].

4.4.4 Zonal patterns

The performance of the SC-AAI was compared to TOMS data, see Fig. 4.7. In this figure the zonal averages of the SCIAMACHY residue (black bold solid line), the SCIAMACHY AAI (black normal solid line), the TOMS V7 residue (purple dashed line), the TOMS V7 AAI (green dashed-dotted line), and the TOMS V8 AAI (red dotted line) are plotted, for 2002, 2003, and 2004. The TOMS V7 residues are daily values, the TOMS V7 AAI are monthly averages. These V7 products are no longer available, because the data are replaced by V8 data, but the V7 products in the figure had been saved from previous studies. The monthly averaged TOMS V7 AAI were only available from January 2002 to July 2003, the daily TOMS V7 residues were available from January 2002 to June 2004. All other other products are freely available for the periods that the various instruments produced measurements. The SCIAMACHY data is cut-off above 60° N and S. Zero values (and invalid data) are not plotted, hence the curves do not always extend to the poles.

The differences between the TOMS V7 residue (purple dashed line) and the TOMS V7 AAI (green dashed-dotted line) show the behaviour of averaging a quantity that is defined by

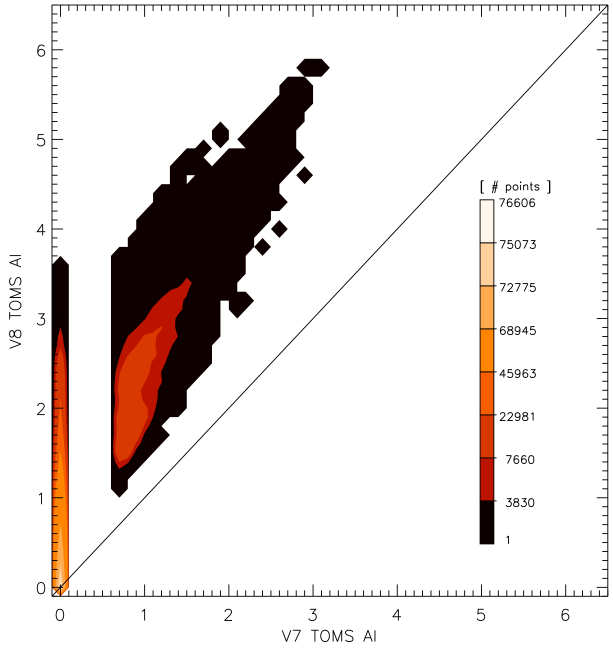

Figure 4.6: *Comparison of monthly averaged TOMS V7 AAI and TOMS V8 AAI, for all valid points in the period Jan. 2002 – Jul. 2003. TOMS V7 AAI is only defined for values* > 0.7.

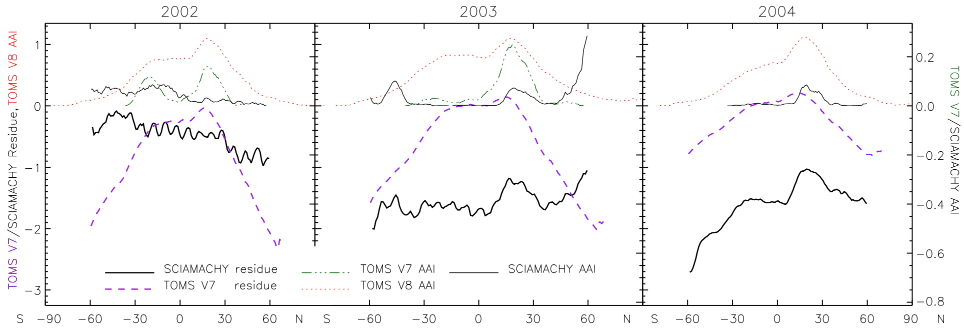

Figure 4.7: *Zonal average of SCIAMACHY residue (black bold solid line), SCIAMACHY AAI (black normal solid line), TOMS V7 residue (purple dashed line), TOMS V7 AAI (green dashed-dotted line), and TOMS V8 AAI (red dotted line), for 2002 – 2004. Left y-axis refers to the TOMS and SCIAMACHY residues and the TOMS V8 AAI, the right y-axis refers to the SCIAMACHY and TOMS V7 AAI.*

a threshold. Since only TOMS V7 residues larger than 0.7 are defined as TOMS V7 AAIs, the averaged TOMS V7 AAI is always positive and the zonal structure of the AAI is different from the zonal structure of the residue because the number of points over which is averaged is not constant for the AAI (it is not always defined). The same holds for the SCIAMACHY AAI (black normal solid line) and the SCIAMACHY (black bold solid line) residue. Since the calibration of SCIAMACHY is different from that of TOMS the threshold from which to define the AAI is different and comparison of the AAIs is difficult. Instead we compare residues (SCIAMACHY and TOMS V7), because an error in the calibration in one or both instruments will only yield a different absolute value of the residue (assuming the sensitivity of the residue to the geometry and atmospheric conditions is the same). Of the version 8 data only AAI data are provided in the TOMS L3 datasets. The full residuals are provided on the TOMS L2 datasets but these were not investigated.

In 2002 the SCIAMACHY residue (and hence SC-AAI) results are not very satisfactory, no clear zonal pattern is discernible in Fig. 4.7. In 2003 a local peak is seen around 25°N, but the picture is mostly determined by the noise near the poles. In 2004 the noise level has dropped below the signal level and is confined to a region near 60° N and S. The SCIAMACHY residue correlates well to the TOMS V7 residue in 2004, although the SCIAMACHY residue is lower by about 0.2. The SCIAMACHY residue correlates also well with the TOMS V8 AAI in 2004 (but shifted by −0.4).

A clear peak in the SCIAMACHY residue can be distinguished between 5° −30° N, which is where the major Northern Hemisphere (NH) deserts are located. A smaller peak can be found on the Southern Hemisphere (SH), between 0° – 30° S. The TOMS V7 AAI shows the same behaviour, although the relative differences between the NH and SH are less than in the SCIAMACHY residue. In the period 1996 – 2000 both TOMS and GOME found a similar behaviour, with a large difference between the NH and SH [*De Graaf et al.*, 2005].

From the difference between the SCIAMACHY and TOMS V7 residues we might conclude that the quotient of the correction factors is not correct, producing smaller residues than expected. Therefore the threshold where absorbing effects and scattering effects are separated, and from which the AAI must be defined, is smaller than that of TOMS, probably even negative. Whether the correction factor for the smallest wavelength (R_{340}) is too large or the correction factor for the largest wavelength (R_{380}) is too small cannot be determined, because the residue only gives information about the slope of the reflectance spectrum. From the value of –0.2 we can conclude the error in the quotient of the correction factors is about 0.5 – 1 %. The TOMS V8 AAI is larger than the SCIAMACHY residue by about 0.4, but this additional value is caused TOMS' higher sensitivity and greater daily global coverage. When more positive values are found the (zonal) average will increase since the number of pixels over which is averaged will increase.

4.5 Conclusions

The scientific Absorbing Aerosol Index product (SC-AAI) of SCIAMACHY shows promising results for 2004. The underestimated reflectance of SCIAMACHY in the UV [*Tilstra et al.*, 2004] was corrected with constant multiplication factors at the AAI wavelengths 340 nm (1.210) and 380 nm (1.130). This resulted in an AAI that is almost in the expected range of lower than zero for scattering events (clouds and scattering aerosols) and higher than zero for absorbing aerosols. However, Figs. 4.5 and 4.7 show that the correction factors are still not correct and a better calibration of the reflectances is necessary. The error in the quotient of the correction factors is about 0.5 – 1 %.

The SC-AAI algorithm accounts for polarisation in the Rayleigh reflectances, thereby improving the viewing angle offset found in the operational AAI product (L2-AAI). As the L2-AAI is calculated in the level 1 to level 2 processing stage, the LUTs used by the processor can easily be updated using a radiative transfer model incorporating (linear) polarisation. This would improve the L2-AAI and make it a useful product. The only problem remaining then for the operational product would be the reflectance offset, which can be corrected using a linear shift of the AAI. This change of LUTs is highly recommended.

The SCIAMACHY SC-AAI has revealed sun glint related problems in the interpretation of the AAI. Sun glint can easily be defined geometrically, but the sun glint mask used for SCIAMACHY pixels does not distinguish between high AAIs as a result from sun glint or from aerosol events. This might be improved using the absolute value of the reflectances. Absorbing aerosol events reduce the reflectances, but more so at the lower wavelength, causing a positive residue. It is anticipated that sun glint will increase the reflectances, but probably more so at the higher wavelength, also creating a positive residue.

The SC-AAI gives reasonable results after March 2004, when the processor version was updated to version 5.01. The seasonal means in 2004 show the same characteristics as were found by GOME in 1995 – 2000 and the same as found by TOMS. This makes SCIAMACHY suitable for the continuation of the long-term AAI record, now that GOME is failing and EP/TOMS is suffering from degradation.

Acknowledgements L. G. Tilstra is thanked for his many helpful contributions to this paper. NASA GSFC is acknowledged for the use of their data. SCIAMACHY data were provided by the European Space Agency. SCIAMACHY is a joint project of the German Space Agency DLR and the Dutch Space Agency NIVR with contribution of the Belgian Space Agency BUSOC. This work was financed by the NIVR SCIAMACHY validation project.

5

Analysis of reflectance spectra of UV-absorbing aerosol scenes measured by SCIAMACHY

Abstract

Reflectance spectra from 280–1750 nm of typical desert dust aerosol (DDA) and biomass burning aerosol (BBA) scenes over oceans are presented, measured by the space-borne spectrometer SCanning Imaging Absorption SpectroMeter for Atmospheric CartograpHY (SCIAMACHY). DDA and BBA are both UV absorbing aerosols, but their effect on the top-of-atmosphere (TOA) reflectance is different due to differences in the way mineral aerosols and smoke reflect and absorb radiation. Mineral aerosols are typically large, inert particles, found in warm, dry continental air. Smoke particles, on the other hand, are usually small particles, although often clustered, which are chemically very active and highly variable in composition. Moreover, BBA are hygroscopic and over oceans BBA were invariably found in cloudy scenes. Spectra of typical DDA and BBA scenes were analysed, using radiative transfer simulations, and compared. The DDA spectrum was successfully simulated using a layer with a bimodal size distribution of mineral aerosols in a clear sky. The spectrum of the BBA scene, however, was determined by the interaction between cloud droplets and smoke particles, as is shown by simulations with a model of separate aerosol and cloud layers and models with internally and externally mixed aerosol/cloud layers. The occurrence of clouds in smoke scenes when sufficient water vapour is present usually prevents the detection of these aerosol plumes using space-borne sensors. However, the Absorbing Aerosol Index (AAI), a UV colour index, is not sensitive to scattering aerosols and clouds and can be used to detect these otherwise obscured aerosol plumes. This method can be an important tool to estimate the global impact of shortwave radiation absorption by smoke and industrial aerosols inside clouds.

M. de Graaf, P. Stammes and I. Aben (2006), *JGR 111*, DOI: 10.1029/2006JD007249, *submitted*

5.1 Introduction

Our understanding of the effect of absorbing aerosols on the Earth's radiative budget has increased rapidly over recent years, especially since aerosols were identified as the largest uncertainty in modelling of climate radiative forcing [*IPCC*, 2001]. Absorbing aerosols reduce the irradiance at the surface and heat the atmosphere, thereby changing the lapse rate and vertical stability of the atmosphere, the hydrological cycle and circulation patterns. As cloud condensation nuclei (CCN), aerosols influence cloud growth rates, cloud lifetimes and precipitation intensities, and cloud albedo [e.g. *Twomey*, 1959b; *Albrecht*, 1989; *Hansen et al.*, 1997; *Haywood and Boucher*, 2000; *Ackerman et al.*, 2000; *Ramanathan et al.*, 2001; *Koren et al.*, 2004; *Lohmann and Feichter*, 2005]. The characterisation of aerosol properties is difficult using ground-based measurements, due to the short lifetime of atmospheric aerosols and heterogeneous horizontal distribution in the atmosphere. The continuous observations by satellite instruments are therefore essential to monitor aerosol distributions and assess their radiation impact [*Kaufman et al.*, 2002].

Satellite measurements, especially from the Total Ozone Mapping Experiment (TOMS), have been used extensively to study the global distribution of UV-absorbing aerosols. The most important UV-absorbing aerosols are desert dust [e.g., *Chiapello et al.*, 1999; *Prospero et al.*, 2002; *Eckardt and Kuring*, 2005; *Darmenova et al.*, 2005; *Kaufman et al.*, 2005], biomass burning aerosols [e.g., *Gleason et al.*, 1998; *Hsu et al.*, 1999a; *Spichtinger et al.*, 2001; *Duncan et al.*, 2003; *Tanré et al.*, 2001], and volcanic aerosols [e.g., *Seftor et al.*, 1997].

Most current satellite aerosol retrieval algorithms rely on cloud screening before retrieving aerosol information [e.g. *Tanré et al.*, 1996; *Torres et al.*, 1998; *Veefkind et al.*, 2000; *Diner et al.*, 2001; *King*, 2003; *Hauser et al.*, 2005; *Kusmierczyk-Michulec and de Leeuw*, 2005]. This means a huge reduction of the global monitoring capability of satellite instruments, especially for those with large footprints. Furthermore, it prohibits remote sensing studies of cloud-aerosol interactions in those cases where clouds are present. However, the AAI, the scene colour in the UV compared to that of a pure Rayleigh atmosphere, is insensitive to scattering aerosols and clouds [*Herman et al.*, 1997; *Torres et al.*, 1998; *De Graaf et al.*, 2005], and can be used to monitor the distribution of UV-absorbing aerosols in cloud free and cloud contaminated satellite data, both over land and ocean.

Using Global Ozone Monitoring Experiment (GOME) data, UV-absorbing aerosols have been shown to have a different effect on the TOA reflectance spectrum in the range of 300 – 800 nm for different aerosol types [*De Graaf et al.*, 2006]. Over land the reflectances at visible and longer wavelengths were mainly determined by the surface albedo, but over ocean all DDA scenes showed a relatively low reflectivity decreasing with wavelength, even when the mineralogical properties of desert dust can be very variable [*Sokolik and Toon*, 1999]. BBA scenes were much more variable. About half of the BBA scenes were also low reflectance scenes decreasing with wavelength, like the DDA scenes, while the other half showed a high reflectance increasing with wavelength. In this paper the reflectance spectra of a typical ocean DDA scene and a high reflectance ocean BBA scene are shown in a broad spectral range (280–1750 nm) with a high spectral resolution, using SCIAMACHY measurements. They are compared to reflectance spectra of clear sky scenes, and the effects of the aerosols on the TOA reflectance is modelled using radiative transfer simulations. The two cases of high aerosol loading scenes are a Saharan dust blowing event and a smoke scene from intense savanna fires over south western Africa. Both cases had a high AAI of around 3.5.

Globally, the Sahara desert is the most important source of mineral aerosols. Several hundred million tons are estimated to be transported from the Sahara to the tropical North Atlantic Ocean and the Mediterranean Sea yearly [*D'Almeida*, 1986; *Prospero et al.*, 1996]. The most intense period of dust transport from the Saharan source region is the boreal summer, but dust storms can be observed year-round [*De Graaf et al.*, 2006]. Saharan dust usually resides in a near-neutrally stable layer of dry air confined between two temperature inversion layers [*Prospero and Carlson*, 1972]. Mineral aerosols provide surfaces for chemical reactions, change the concentration of other aerosols in the atmosphere, and affect cloud nucleation and optical properties. The iron content in desert dust plays a major role in ocean fertilisation and oceanic carbon dioxide uptake, thereby affecting the global carbon budget [*Gao et al.*, 2001]. Dust transported to downwind terrestrial ecosystems can play a major role in soil formation and nutrient cycling [*Okin*, 2005].

Spectrally, desert dust is a UV-absorbing aerosol, mainly due to the presence of hematite and other iron oxides. The imaginary part of the refractive index of desert dust is largest in the UV and decreases rapidly with wavelength, although the amount of absorption of desert dust in the UV is still under discussion [*Patterson et al.*, 1977; *Sinyuk et al.*, 2003; *Torres et al.*, 2005]. Since mineral particles are irregularly shaped, the optical modelling of desert dust is also a matter of debate. Mie theory, which is valid for homogeneous, spherical particles, is often used because it is well developed and good results can be produced [e.g. *Sinyuk et al.*, 2003; *Waquet et al.*, 2005]. As an alternative spheroids might be used, which reduces the amount of small mode particles in ground-based aerosol retrievals [*Dubovik et al.*, 2002a]. More complex particle-shape models are available [*Veihelmann et al.*, 2004], but these are computationally demanding and beyond the scope of this paper.

Smoke is produced by annually recurring savanna fires in south west Africa, during the local monsoonal dry period [*Herman et al.*, 1997; *Torres et al.*, 2002; *De Graaf et al.*, 2006]. These fires are mainly man-made to benefit agriculture. Smoke plays an important role as CCN, influencing cloud microphysics and precipitation processes. The presence of smoke plumes decreases cloud droplet sizes and increases the reflectivity of clouds [*Twomey*, 1959a; *Lohmann and Feichter*, 2005]. Smoke properties vary between fires depending on fuel type and moisture, combustion phase, flame temperature, wind conditions, and other variables. Smoke particles are usually internally mixed, typically with a core of black carbon and alkali earth compounds coated with organic compounds. Fresh smoke properties change rapidly and aged smoke properties, which are more of interest for global climate dynamics, are markedly different from fresh smoke properties, but vary more slowly. Smoke particles are typically small, but increase in size with age and aged particles are more spherical than fresh ones. Eighty percent of the mass and over ninety percent of scattering by smoke can be attributed to the fine mode [*Reid et al.*, 2005b]. Small absorbing particles are very efficient in absorbing and scattering light, independent of their sizes. Therefore, small quantities of light-absorbing particles can make a considerable contribution to the attenuation of light in the atmosphere [*Horvath*, 1993; *Reid et al.*, 2005a]. The aerosol component responsible for absorption in biomass burning is black carbon, or soot. Black carbon absorption depends weakly on wavelength over the near-UV to near-IR spectral region, where the soot imaginary refractive index is relatively constant [*Bergstrom et al.*, 2002; *Torres et al.*, 2005].

In this paper, first the methods and data used for the analyses are described in section 5.2. A description of the desert dust and biomass burning aerosol scenes, the SCIAMACHY reflectance spectra of these scenes and the radiative transfer simulations are presented in section 5.3. The results and conclusions are discussed in section 5.4.

5.2 Methods and Data

5.2.1 Radiative transfer modelling

Atmospheric reflectances were simulated using the Doubling-Adding KNMI (DAK) radiative transfer model [*Stammes*, 2001]. This model computes the monochromatic reflectance and transmittance in a plane-parallel atmosphere including polarisation, using the polarised doubling-adding method [*De Haan et al.*, 1987]. This method calculates the vectorised internal radiation field of the atmosphere in an arbitrary number of layers, each of which can have Rayleigh scattering, gas absorption, and aerosol and cloud particle scattering and absorption. Only ozone absorption was accounted for, all other trace gases were ignored. For the atmospheric gas and temperature profiles 32 atmospheric layers were used, simulating the standard Mid-Latitude Summer atmosphere for scenes at latitudes greater than ±23°, and the standard Tropical atmosphere for scenes at latitudes less than ±23° [*Anderson et al.*, 1986]. The standard ground pressure was 1013 hPa and the standard ozone column 334 DU.

5.2.2 Mie modelling

The optical properties of aerosol and cloud particles in the model were calculated using Mie theory [*De Rooij and van der Stap*, 1984]. In each layer a mono-modal or bimodal log-normal size distribution could be prescribed. In case of a bimodal size distribution, a weight function w defines the relative number of fine mode and coarse mode particles [*Bösche et al.*, 2006],

$$\frac{dN}{dr} = w \cdot \mathrm{L}_f + (1 - w) \cdot \mathrm{L}_c, \tag{5.1}$$

where dN/dr is the number distribution and $L_{f,c}$ the log-normal size distributions for the fine and the coarse mode, constrained by the effective radius r_{eff} and the effective variance v_{eff} [cf. *Hansen and Travis*, 1974].

The microphysical parameters used in this paper are given for 340, 550 and 1000 nm in Table 5.1. The effective radii and variances for the bimodal size distribution of the desert dust model were chosen similar to the small and large mode (unimodal size distribution) models of *Torres et al.* [1998], where the effective radii were fitted to the measurements, described in section 5.3.1. The real and imaginary parts of the refractive index were taken from *Hess et al.* [1998] for transported mineral aerosol, smoothed and interpolated to a one nm grid.

A model for absorbing biomass burning aerosols was chosen similar to the carbonaceous models of *Torres et al.* [1998], where the effective radius was fitted to the measurements, described in section 5.3.2. The absolute value of the imaginary part of the refractive index for this aerosol model was 0.08, which represents extreme absorption and should be considered as an upper limit.

Water droplets were simulated using a large effective radius (Table 5.1) and the real and imaginary parts of the refractive index were taken from *Palmer and Williams* [1974] (Table 5.2).

In one case in section 5.3.2, an effective single scattering albedo was determined from the measurements, using a Henyey-Greenstein (HG) phase function [*Henyey and Greenstein*, 1941] instead of Mie calculations. In this way no knowledge of the refractive index is needed and the single scattering albedo can be directly determined from the measurements.

5.2.3 SCIAMACHY reflectance spectra

SCIAMACHY is part of the payload of the European 'Environment Satellite' (Envisat), launched on 1 March 2002 by an Ariane-5 launch vehicle from the Guyana Space Centre into a polar orbit at about 800 km altitude, with an equator crossing-time of 10:00 a.m. (local time) for the descending node, orbiting the Earth every 100 min. SCIAMACHY is a spectrometer designed to measure sunlight, transmitted, reflected and scattered by the Earth's atmosphere or surface, in eight channels from 240–2380 nm at a spectral resolution of 0.2–1.5 nm [*Bovensmann et al.*, 1999]. The radiance is observed in two alternating modes, nadir and limb, yielding data blocks called states. The size of a nadir state is approximately 960×4870 km^2. In nadir mode, SCIAMACHY scans the Earth from east to west in four seconds by rotating one of its internal mirrors. The radiance measurements of the first six channels were used at an optical integration time (IT) of one second, to produce a continuous reflectance spectrum from 240–1750 nm. With this IT a state is divided into thirteen swaths, which are divided into four pixels of approximately 240×30 km^2. The reflectance is defined as $R = \pi I/(\mu_0 E_0)$, where I is the radiance at TOA, E_0 is the solar irradiance at TOA perpendicular to the direction of the incident sunlight and μ_0 is the cosine of the solar zenith angle θ_0. The extra-terrestrial solar irradiance is measured each day, once per fourteen orbits.

Table 5.1: *Mie calculation parameters at 550 nm for a log-normal size distribution.*

Aerosol model		Size parameters $r_{\text{eff}}(\mu\text{m})$	Size parameters v_{eff}	Refractive index $Re(m)$	Refractive index $Im(m)$
DDA	fine mode	0.07	1.95	1.53	−0.0055*
	coarse mode	0.35	2.20		
BBA		0.08	1.45	1.55	−0.08
water droplets		6.0	1.50	1.335*	0.0*

* wavelength dependent variable

Table 5.2: *Aerosol optical properties at 340, 550 and 1000 nm*

Aerosol model	type	τ			ω_0			τ_{abs}		
		340	550	1000	340	550	1000	340	550	1000
DDA fine mode	Mie	1.34	1.06	0.54	0.87	0.96	0.97			
DDA coarse mode	Mie	0.64	0.68	0.73	0.64	0.85	0.93			
Desert dust	bimodal Mie	1.98	1.74	1.27	0.79	0.92	0.95	0.42	0.14	0.06
BBA	Mie	0.64	0.30	0.083	0.72	0.66	0.46			
Water droplets	Mie	19.4	19.7	20.2	1.0	1.0	1.0			
1 Layered	mono-modal Mie	20.1	20.0	20.3	0.991	0.995	0.997	0.18	0.10	0.06
2 Internal mix	HG	20.0	20.0	20.0	0.968	0.992	0.999	0.64	0.16	0.02
3 External mix	bimodal Mie	20.1	20.0	20.3	0.991	0.995	0.997	0.18	0.10	0.06

SCIAMACHY's reflectances are about 15-20% too low [*Acarreta and Stammes*, 2005; *Tilstra et al.*, 2005], therefore calibration corrections were applied to the spectra using a smooth function through the correction factors in the UV supplied by *Tilstra et al.* [2005] and the correction factors in the visible and near-IR supplied by *Acarreta and Stammes* [2005]. Above 900 nm the correction function was kept constant. In addition, a correction for a calibration error caused by improper characterisation of the instrument's polarisation response function around 350 nm was applied [*Tilstra and Stammes*, 2005]. Reflectance jumps between neighbouring channels were corrected by averaging the measurements where wavelengths of neighbouring channels overlap.

5.2.4 SCIAMACHY AAI

The AAI separates the radiance contrast at two wavelengths (λ_0, λ) in the UV caused by aerosol absorption from that caused by molecular Rayleigh scattering. It uses measured reflectances $R^{\text{meas}}_{\lambda_0,\lambda}$ and simulated reflectances for a Rayleigh atmosphere $R^{\text{Ray}}_{\lambda_0,\lambda}$ with an adjustable Lambertian surface albedo. The AAI is derived from the residue.

The residue $r_{\lambda_0,\lambda}$ is usually defined as [*Herman et al.*, 1997; *Torres et al.*, 1998; *De Graaf et al.*, 2005]

$$r_{\lambda_0,\lambda} = -100 \cdot {}^{10}\log\left(\frac{R^{\text{meas}}_{\lambda}}{R^{\text{Ray}}_{\lambda}}\right), \tag{5.2}$$

with the assumption that the surface albedo A_s for which R^{Ray}_{λ} is calculated, satisfies

$$R^{\text{Ray}}_{\lambda_0}(A_s) = R^{\text{meas}}_{\lambda_0}. \tag{5.3}$$

So the surface albedo is assumed to be constant in the range $[\lambda, \lambda_0]$. The SCIAMACHY residue is calculated for $\lambda = 340$ nm and $\lambda_0 = 380$ nm, so this assumption is valid for most surfaces. Now $r_{\lambda_0,\lambda}$ can be expressed as

$$r_{\lambda_0,\lambda} = -100 \cdot \left\{ {}^{10}\log\left(\frac{R_\lambda}{R_{\lambda_0}}\right)^{\text{meas}} - {}^{10}\log\left(\frac{R_\lambda}{R_{\lambda_0}}\right)^{\text{Ray}} \right\}, \tag{5.4}$$

i.e. the difference between the slope of the measured reflectances and the slope of the Rayleigh reflectances at λ_0 and λ. Note that $R^{\text{Ray}}_{\lambda_0}$ and R^{Ray}_{λ} are dependent on the surface albedo, which changes for every scene. Therefore, it is more convenient to eliminate the Rayleigh reflectances $R^{\text{Ray}}_{\lambda_0}$ and R^{Ray}_{λ} from Eqs. (5.2) and (5.3) and express $r_{\lambda_0,\lambda}$ as a function of only the measured reflectances $R^{\text{meas}}_{\lambda_0}$ and $R^{\text{meas}}_{\lambda}$ and some atmospheric constants.

In order to do so, the surface contribution to the reflectance at TOA is separated from that of the atmosphere, using the assumption that the atmosphere is bounded from below by a Lambertian surface, which reflects incident radiation uniformly and unpolarised in all directions [*Chandrasekhar*, 1960]:

$$R(\lambda, \mu, \mu_0, \phi - \phi_0, A_s) = R_0(\lambda, \mu, \mu_0, \phi - \phi_0) + \frac{A_s T(\lambda)}{1 - A_s s^*(\lambda)}. \tag{5.5}$$

The first term, R_0, is the path radiance, which is the atmospheric contribution to the reflectance, depending on the relative azimuth angle $\phi - \phi_0$. The second term is the azimuth-independent contribution of the surface with an albedo A_s. Here, $T = t(\mu)t(\mu_0)$, where t is the total atmospheric transmission, dependent on μ_0 and μ, which is the cosine of the viewing zenith angle θ and s^* is the spherical albedo of the atmosphere for illumination from below. Substituting Eq. (5.5) in Eq. (5.3), the surface albedo is expressed in terms of $R^{\text{meas}}_{\lambda_0}$,

$$A_s = \frac{R^{\text{meas}}_{\lambda_0} - (R_0)_{\lambda_0}}{T_{\lambda_0} + s^*_{\lambda_0}(R^{\text{meas}}_{\lambda_0} - (R_0)_{\lambda_0})}. \tag{5.6}$$

When A_s is substituted in Eq. (5.5) the Rayleigh reflectance at wavelength λ is found,

$$R^{\text{Ray}}_{\lambda} = (R_0)_\lambda + \frac{T_\lambda \cdot (R^{\text{meas}}_{\lambda_0} - (R_0)_{\lambda_0})}{T_{\lambda_0} + (s^*_{\lambda_0} - s^*_\lambda)(R^{\text{meas}}_{\lambda_0} - (R_0)_{\lambda_0})}. \tag{5.7}$$

Now R^{Ray}_{λ} can eliminated from Eq. (5.2):

$$r_{\lambda_0,\lambda} = -100 \cdot {}^{10}\log\left(\frac{R^{\text{meas}}_{\lambda}}{(R_0)_\lambda + c_a}\right), \tag{5.8}$$

where

$$c_a = T_\lambda \cdot \left((s^*_{\lambda_0} - s^*_\lambda) + \frac{T_{\lambda_0}}{R^{\text{meas}}_{\lambda_0} - (R_0)_{\lambda_0}}\right)^{-1} \tag{5.9}$$

is the adjusted surface contribution. Equation 5.8 shows that the residue will be positive in cases where the measured scene reflectance is smaller than the sum of the path radiance and adjusted surface contribution. In case of a low surface reflectivity, this can be accomplished when the measured reflectance is decreased relative to the path radiance at λ, by absorption in the atmosphere. In the UV the path radiance is strongly wavelength dependent due to Rayleigh scattering, and even gray absorbers can reduce the reflectance stronger at λ compared to λ_0, where $\lambda < \lambda_0$ [*Torres et al.*, 1998; *De Graaf et al.*, 2005]. In case of a bright surface however, the contribution of the path radiance is small and the positive residue must be caused by a wavelength dependent absorber.

The AAI is defined as the positive part of the residue, which has been shown to be indicative for UV-absorbing aerosols [*Hsu et al.*, 1996; *Herman et al.*, 1997; *Torres et al.*, 1998; *De Graaf et al.*, 2005, 2006]. The SCIAMACHY AAI was used to find scenes with high aerosol loadings.

5.2.5 Surface albedo database

The surface albedo used in the radiative transfer model was taken from the GOME spectral surface albedo database [*Koelemeijer et al.*, 2003]. With this database a surface reflectivity can be determined for the range 335-772 nm for an arbitrary area on the Earth's surface. At wavelengths larger than 772 nm the surface albedo is kept constant, which is a good approximation for ocean surfaces.

5.2.6 Cloud detection

For every SCIAMACHY pixel the effective cloud fraction and cloud pressure are determined using the Fast REtrieval Scheme for Clouds from the O_2 A-band (FRESCO) algorithm [*Koelemeijer et al.*, 2001; *Fournier et al.*, 2006], which makes use of the reflectance in and around the oxygen A-band at 760 nm. The algorithm uses simplified radiative transfer modelling to determine the amount of cloud and clear sky reflected radiance, where the cloud is assumed to be a Lambertian reflector with albedo 0.8 and the clear sky is bounded from below by a Lambertian surface, the albedo of which is taken from the GOME spectral surface albedo database.

Additionally, SCIAMACHY's Polarization Measurement Devices (PMD) were used to create true colour images. The PMDs have a higher spatial resolution (7.5×30 km^2) than the spectral channel measurements and were used to visually identify clouds. The PMD images are not shown here.

5.2.7 MODIS Aerosol Optical Thickness and RGB images

From MODerate resolution Imaging Spectroradiometer (MODIS) aboard NASA's Terra satellite, the aerosol optical thickness (AOT) at 550 nm was used to characterise the aerosol loading of the scenes. Terra/MODIS, launched at the end of 1999 into a polar orbit at about 700 km altitude, with an equator crossing-time of 10:30 a.m. (local time) for the descending node, is making near-global daily observations of the Earth. The AOT is available over both land and ocean, using different algorithms. Cloud and sunglint screening is performed before retrieving an AOT. The error of MODIS optical thickness retrievals are within ($\pm 0.03 \pm 0.05\,\tau$) over ocean and ($\pm 0.05 \pm 0.15\,\tau$) over land [*Remer et al.*, 2005].

In addition to the MODIS AOT, true-colour composites were created from MODIS bands 1, 4 and 3 (RGB), using reprojected level 1B granules mosaics with a desert style colour enhancement. No quantitative information was extracted from these files, but they were used as a visual aid.

5.2.8 Back trajectory modelling

Atmospheric back trajectories used in the analyses were calculated using the trajectory model TRAJKS [*Scheele et al.*, 1996; *Stohl et al.*, 2001]. TRAJKS is an off-line model, using three dimensional European Centre for Medium-Range Weather Forecasts (ECMWF) L60 forecasting model data. L60 data have 60 vertical levels with a horizontal resolution of less than one degree. The time resolution of the input data is six hours. The output data are gridded to a $0.1^\circ \times 0.1^\circ \times 1$ hour grid.

5.3 Analyses

5.3.1 Desert dust scene

A Saharan desert dust blowing event on 25 July 2004 was selected to study the spectrum of a desert dust aerosol scene over a dark ocean surface, compared to that of a clear sky ocean

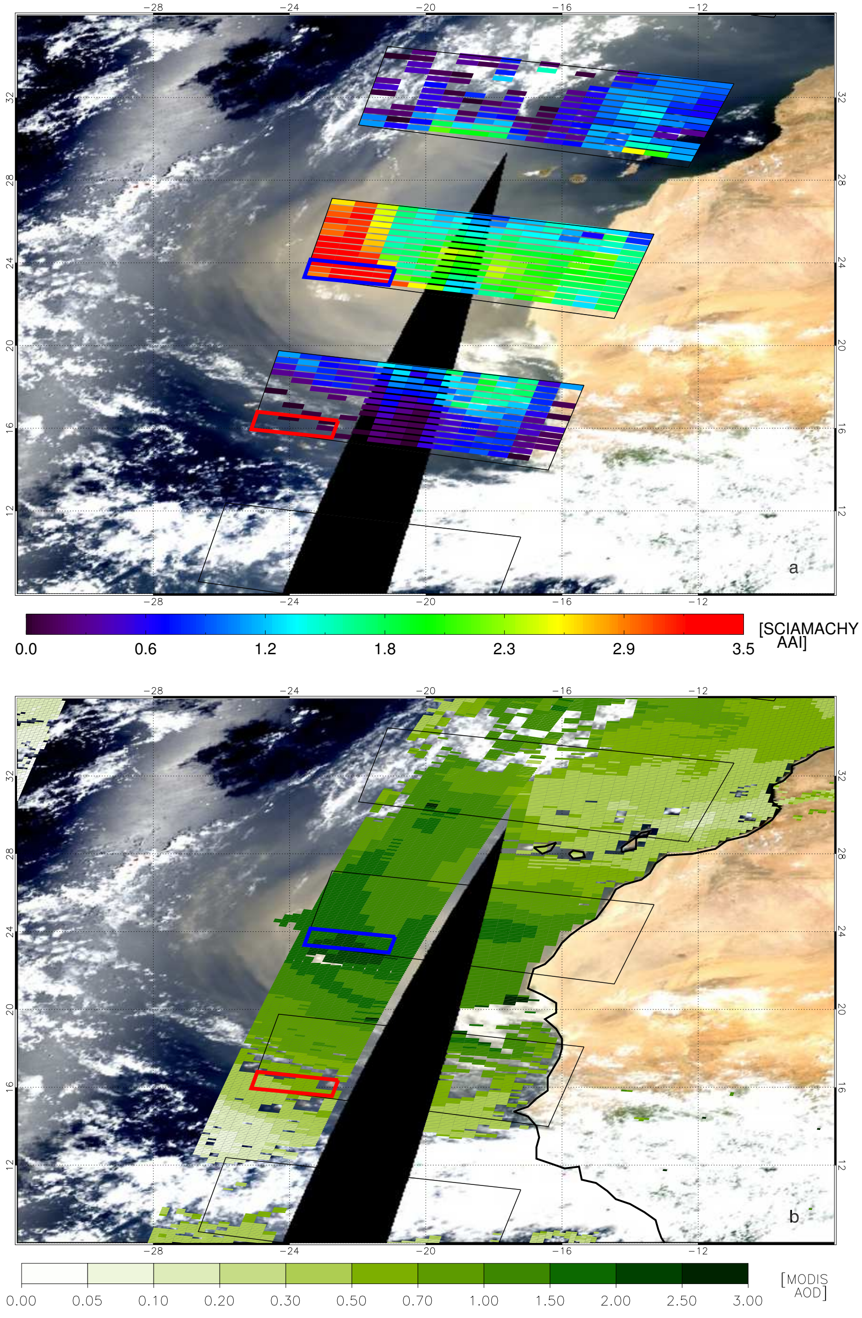

Figure 5.1: *MODIS RGB image of dust storm on 25 July over west Sahara and eastern North Atlantic Ocean with (a) SCIAMACHY AAI and (b) with MODIS total AOT at 550 nm. The blue and red rectangles are the selected scenes. the geometries* [$\theta_0, \theta, \phi - \phi_0$] *of the blue and red scenes are* [*24.7°,28.7°,189.9°*] and [*24.7°,30.4°,203.3°*], *respectively.*

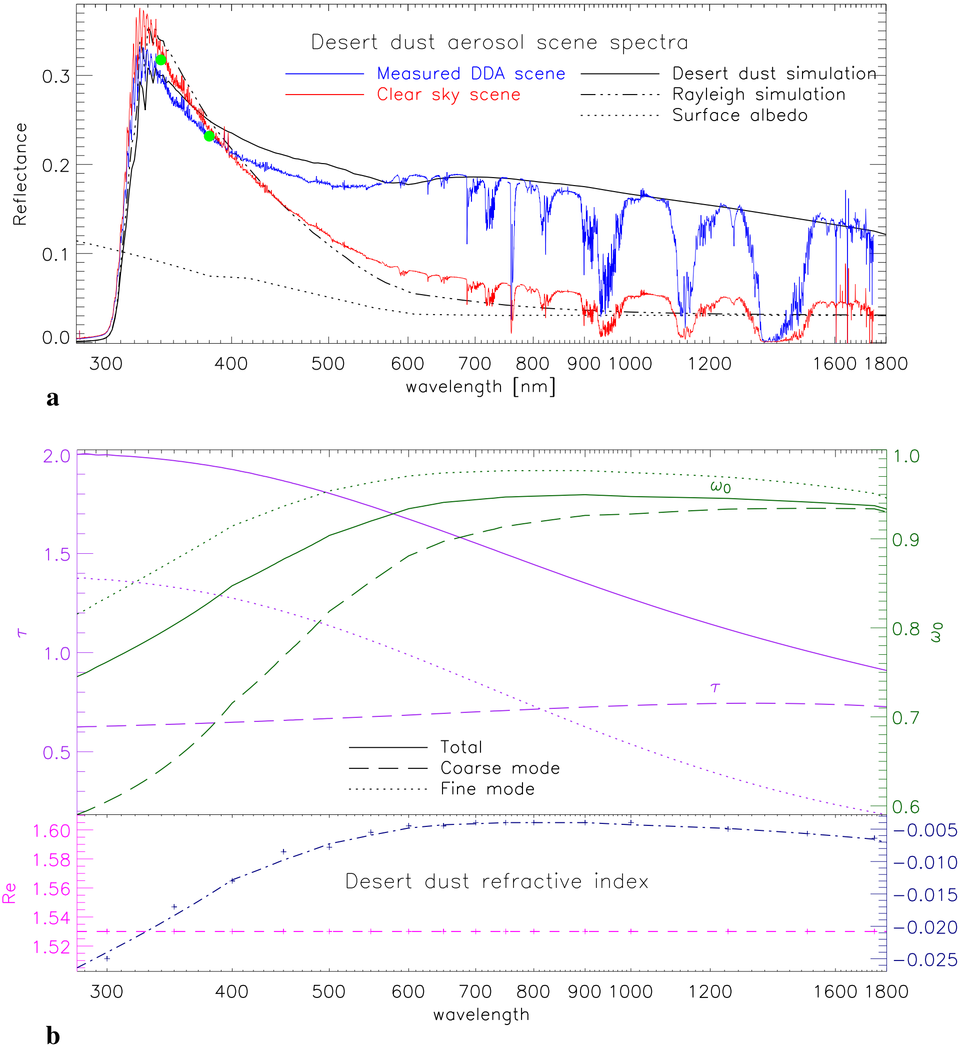

Figure 5.2: *(a) Measured spectra of clear sky (red) and desert dust (blue) scenes of Fig. 5.1 and simulations using a bimodal mineral aerosol model (black solid line) and Rayleigh atmosphere model (black dashed-dotted line). The surface albedo used in the simulation is given by the dotted line. The green dots are the simulated Rayleigh atmosphere reflectances with adjusted surface albedo used in the residue calculations. (b) Upper panel. Optical parameters for the desert dust model: Optical thickness (purple) and single scattering albedo (green) of the fine mode (dotted lines), coarse mode (dashed lines) and the total layer (solid line). Lower panel. The real (magenta dashed line) and imaginary (blue dashed-dotted line) part of the refractive index used for the simulation of the bimodal mineral aerosol model. The +-signs refer to the data points given by Hess et al. [1998].*

scene. In Fig. 5.1a the horizontal distribution of SCIAMACHY AAI at 9:15 UTC is overlaid on a MODIS RGB picture, acquired around 11:10 UTC (right side of the plot) and 12:50 UTC (left side of the plot). The black triangular area is the area outside the MODIS swath. The black rectangular contours depict the nadir states of SCIAMACHY within which data are available. Outside these states limb data or no data are available.

In Fig. 5.1b the MODIS AOT at 550 nm over land and ocean is overlaid over the same MODIS RGB picture as in Fig. 5.1a. No MODIS AOT is retrieved over bright land surfaces, cloudy areas and sunglint areas. In Fig. 5.1 the left upper third of the picture is a sunglint area for MODIS' geometry.

The blue and red rectangles are selected scenes for which the SCIAMACHY reflectance spectra were determined. The blue rectangle, the desert dust scene, was chosen where the SCIAMACHY AAI was greatest. The red rectangle, the clear sky scene, was chosen so that the scene had almost the same geometry as the scene of the blue rectangle, but negative SCIAMACHY residue, and no clouds according to the PMD true colour image. In contrast to the PMD image, the MODIS RGB picture shows remnants of the dust plume in the red rectangle and the MODIS AOT value was around 0.3–0.5. However, the MODIS data was acquired $3\frac{1}{2}$ hours after the SCIAMACHY data and the dust plume is spreading outwards. Therefore, the AOT in the red rectangle at the time of the SCIAMACHY overpass is assumed to be small. The average FRESCO effective cloud fraction for all pixels in the red rectangle was 3%.

The reflectance spectra for the selected scenes are shown in Fig. 5.2a. The red curve shows the clear sky spectrum and the blue curve the desert dust spectrum. Also shown, in black, are simulated spectra for a pure Rayleigh atmosphere (dashed-dotted line), the simulated spectrum for an aerosol laden atmosphere (solid line) and the surface albedo used in the simulations (dotted line). The aerosol laden atmosphere was simulated with a bimodal size distribution of mineral aerosols in a layer between three and four kilometres above the surface, which is a normal height for lofted mineral aerosols and sufficient to produce high AAIs. The geometries for both simulated scenes are the same as the geometries of the mean measured scenes.

The measured clear sky spectrum shows the opaque atmosphere for wavelengths below 300 nm due to ozone absorption, a peak in the reflectance and the Huggins band between 310 and 400 nm, and the strong decrease of the reflectance with wavelength above 330 nm due to the λ^{-4} decrease of Rayleigh optical thickness. Above 500 nm several oxygen and water vapour absorption bands can be observed. The reflectance drops to about 0.05 at 1750 nm, which is slightly higher than the modelled clear sky reflectance, that is controlled by the surface albedo from the surface albedo database. This excess of reflectance might be due to aerosol scattering that is possibly still present in the clear sky scene.

The blue curve in Fig. 5.2a shows the reflectance change due to the presence of desert dust aerosols in the atmosphere, when compared to the reflectance of the clear sky. Mineral aerosols are absorbing in the UV; below 400 nm the reflectance of the aerosol laden scene is lower than that of the clear sky scene. This change of the reflectance in the UV is used by the AAI. The AAI of the desert dust scene is 3.34, a high value indicative of the presence of UV absorbing aerosols at a high altitude. The green dots in Fig. 5.2a are the calculated Rayleigh reflectances R^{Ray} in the residue calculation, at 340 and 380 nm. At 380 nm, R^{Ray}_{380} is exactly equal to the measured scene reflectance R^{meas}_{380} (by definition), but at 340 nm R^{Ray}_{340} is larger

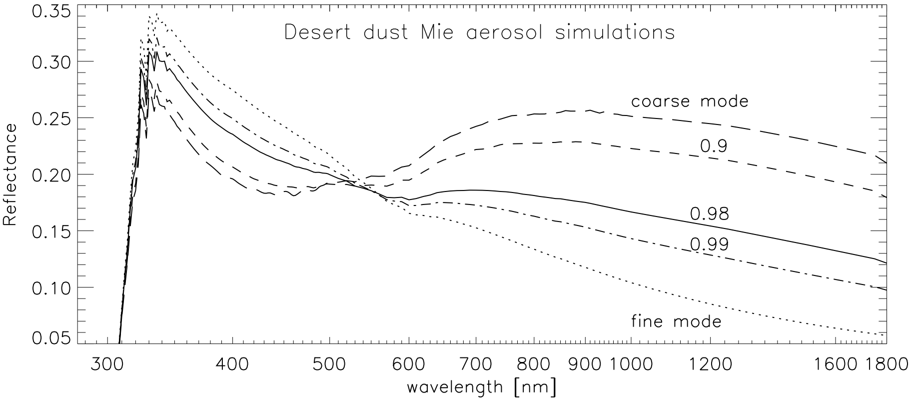

Figure 5.3: *Multiple simulated bimodal mineral aerosol spectra for different weights of the coarse and fine mode. Given weight factors w refer to the number density.*

than the measured scene reflectance, which is caused by the absorption of the large mineral aerosols in the UV and expressed by a positive residue. On the other hand, both points are more or less on the red clear sky spectrum, therefore the residue of the clear sky is small.

Above 400 nm the mineral aerosols are mainly scattering, the reflectance of the aerosol laden scene is higher than that of the clear sky scene.

The real measured scene has a slightly lower reflectance than the modelled scene reflectance between 350 and 570 nm, and higher around 600 nm. The amount of absorption in the UV and scattering at higher wavelengths, which peaks around 650 nm, increases with increasing particle size of the mineral aerosols. For small mineral aerosols the absorption in the UV is negligible and the scattering at larger wavelength is much smaller than for large mineral aerosols, as shown in Fig. 5.3, which illustrates the contributions of the fine and coarse modes. The small mode (dotted line) yields a continuously decreasing reflectance with increasing wavelength larger than 330 nm, not much different from the clear sky spectrum. The coarse mode (long dashed line) on the other hand, is responsible for the absorption at UV wavelengths, while at wavelengths larger than 500 nm the scattering becomes dominant. For increasing weight factor w the absorption in the UV and the scattering at longer wavelengths decreases. A best fit to the measured spectrum was found using a weight w of 0.98, yielding a fine mode/coarse mode AOT fraction of 1.06/0.68 at 550 nm. This confirms the large fraction of the fine mode particles in a retrieved bimodal size distribution when using Mie theory to model mineral aerosols, found by AERONET data fits [*Dubovik et al.*, 2002a, b].

The wavelength dependence of the optical thickness of the aerosol layer (purple solid line in Fig. 5.2b) is completely determined by the fine mode (dotted purple line), which vanishes at near-IR wavelengths, while the absolute value of the AOT is determined by the weight of fine and the coarse mode. This was used to fit the AOT and the effective radius of the coarse mode at longer wavelengths. The best fit AOT was 1.74 at 550 nm, comparable to the MODIS AOT (see Fig. 5.1b). The single scattering albedo of the coarse mode (green dashed line), on the other hand, is lower than that of the fine mode (green dotted line), showing again

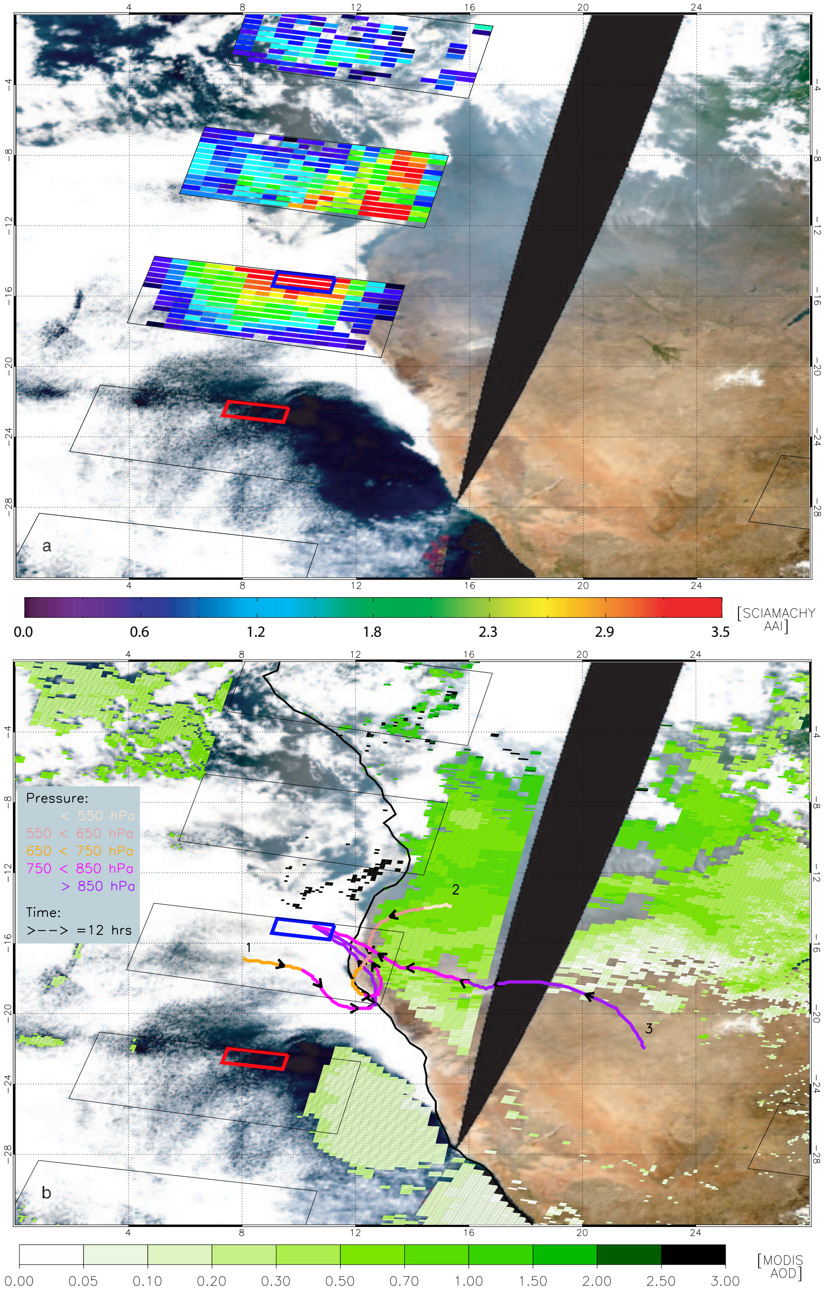

Figure 5.4: *MODIS RGB image of biomass burning on 9 September 2004 over eastern South Atlantic Ocean with (a) SCIAMACHY AAI and (b) MODIS total AOD at 550 nm and TRAJKS back-trajectories. The blue and red rectangles are the selected scenes, the geometries [$\theta_0, \theta, \phi - \phi_0$] of the blue and red scenes are [9.7°,36.5°,43.9°] and [9.7°,41.6°,50.3°], respectively.*

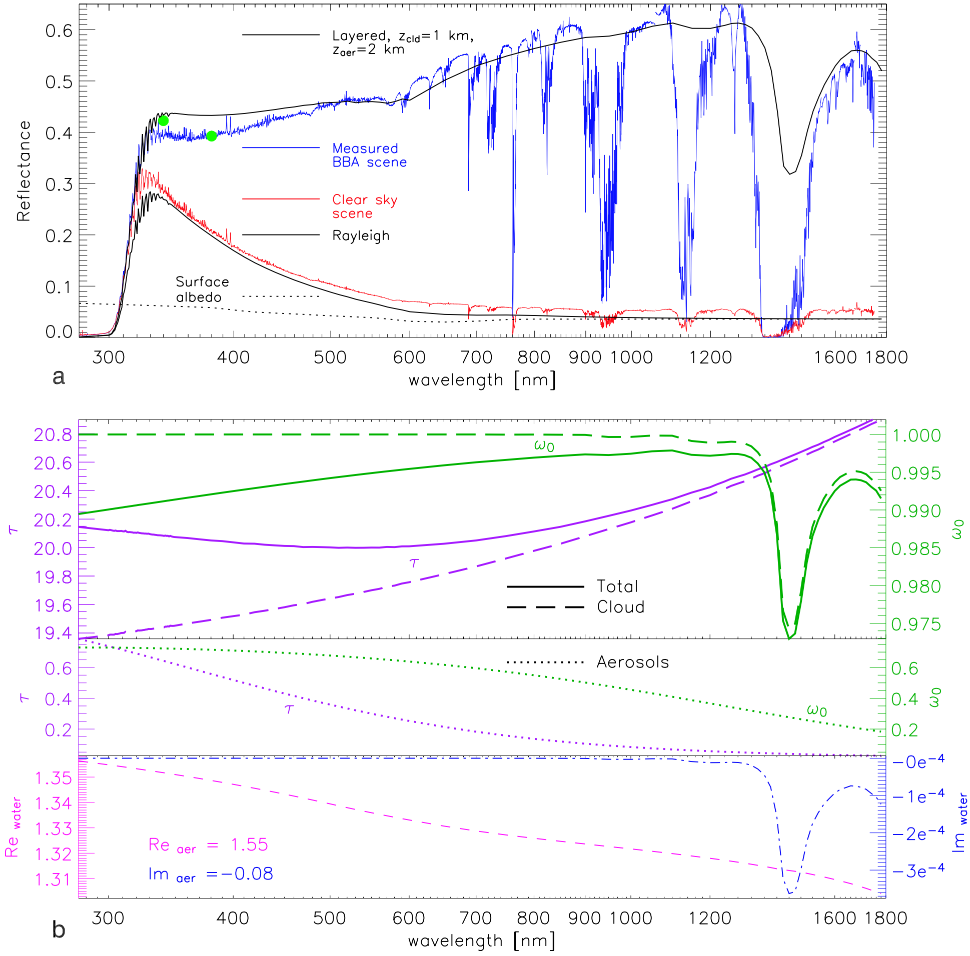

Figure 5.5: *(a) Measured spectra of clear sky (red) and biomass burning aerosol (blue) scenes of Fig. 5.4 and simulation using a layered model of BBA and cloud (black normal line). The simulation of the Rayleigh atmosphere is given by the dashed dotted line and the surface albedo is given by the dotted line. The green dots are the simulated Rayleigh atmosphere reflectances with adjusted surface albedo used in the residue calculations. (b) The single scattering albedo (green) and optical thickness (purple) of the aerosols (dotted lines), cloud layer (dashed lines) and total for both layers (solid lines). The refractive index used for the Mie calculations is given in the lower panel.*

the larger contribution of the coarse mode particles to the absorption in the UV. For both the fine and the coarse mode the same refractive index was used, shown in the lower panel of Fig. 5.2b.

Thus, in the case of mineral aerosols the coarse mode is responsible for the UV absorption and the scattering in the visible and near-IR. The spectrum of the small mode shows a decreasing reflectance with wavelength, comparable to that of the clear sky spectrum (Fig. 5.2a). Therefore, the AAI is sensitive to large mineral particles, but, using spherical particles, the shape of the spectrum cannot be fitted by a single coarse mode alone.

With this fit of the mineral aerosol model to the measurements the absorption optical thickness can be estimated. The absorption optical thickness (τ_{abs}) is the part of the extinction optical thickness that is caused by absorption [*Torres et al.*, 2005]

$$\tau_{\mathrm{abs}} = (1 - \omega_0)\tau. \tag{5.10}$$

This quantity was also derived for the desert dust scene (Table 5.2). It is strongly decreasing with wavelength, as both the single scattering albedo and the optical thickness of the aerosols are wavelength dependent. At 340 nm the absorption optical thickness is 0.42, which is 21% of the total AOT.

5.3.2 Biomass burning scene

An intense smoke scene on 9 September 2004, of a persistent biomass burning event over south west Africa, was selected to study the spectrum of a biomass burning pollution scene with clouds over a dark ocean surface, compared to that of a clear sky ocean scene. The smoke from this agricultural burning was extensive and could be observed at the end of August 2004, circulating over Angola and the adjacent South Atlantic Ocean for a few weeks.

In Fig. 5.4 the SCIAMACHY AAI at 09:12 UTC of 9 September 2004 is overlaid on a MODIS RGB picture, acquired around 08:15 UTC (right side of the plot) and 09:55 UTC (left side of the plot) of the same day. The black rectangular contours depict the nadir states of SCIAMACHY where data were available. The blue and red rectangles are the selected areas for which the reflectance spectra were determined. The blue rectangle was chosen where the SCIAMACHY AAI was greatest and the red rectangle was chosen so that the scene had almost the same geometry as the scene of the blue rectangle, but negative SCIAMACHY AAI, and no clouds according to the PMD true colour image. The average FRESCO effective cloud fraction for all pixels in the red rectangle was 5%. The average FRESCO effective cloud fraction for all pixels in the blue rectangle was 72% and the average cloud top height 1.1 kilometers.

In Fig. 5.4b the MODIS AOT at 550 nm over land and ocean is overlaid over the same MODIS RGB picture as in Fig. 5.4a. Also shown are the back trajectories of air parcels arriving at the blue rectangle on 9 September 2004, 12:00 UTC from three days before. Three back trajectories were computed, one of an air parcel which arrived at 1 km altitude (1), another parcel arriving at 1.5 km altitude (2), and one arriving at 2 km altitude (3). The pressure levels of the air parcels at certain times are given by the colour scale, while the arrow heads denote the direction and the distance travelled in 12 hours.

The trajectories show that air parcel 1 started at 3.5 km altitude over the ocean three days before 9 September 2004, made a turn over land to end in the blue rectangle, all the while loosing altitude. Parcel 2 started over land in the heavily smoke covered area at 5 km altitude, first travelling south-west, making a 270° turn to the north-west on 9 September. The altitude of this parcel continuously decreased. Finally, parcel 3 started at 1.5 km altitude, travelled north-westerly all three days, gradually increasing in altitude.

The smoke causing the high AAI in the blue rectangle was probably transported to this area at all altitudes, since the smoke plume over Angola was already observed over both land and ocean weeks before. Furthermore, the trajectories show that the marked land-ocean boundary in the cloud cover is probably caused by the flow of biomass burning aerosols from over land to the moist ocean. At all three altitudes the wind direction was south-easterly the last 12 hours before arriving at the blue rectangle, thereby crossing the land boundary. Since BBA are very effective CCN, they will immediately condense water when water vapour is available. Therefore, it is likely that the blue rectangle scene contains a mixture of clouds and biomass burning aerosols.

The MODIS RGB picture shows almost no remnants of smoke or clouds in the red rectangle and the MODIS AOT product (Fig. 5.4b) also shows no AOT. Since the overpasses of MODIS and SCIAMACHY are within half an hour, the SCIAMACHY spectrum of the red rectangle scene can be assumed to be a clear sky spectrum.

The SCIAMACHY reflectance spectra of both scenes are plotted in Fig. 5.5. The spectrum of the clear sky scene (plotted in red) is similar to the clear sky scene of Fig. 5.2a, since essentially only the geometries are different. However, the spectrum of the polluted cloudy scene (plotted in blue) shows a reflectance that is, outside gas absorption bands, continuously increasing with wavelength until about 1400 nm. Instead of the expected absorption in the UV, the reflectance is much larger than the clear sky scene reflectance, and increasing with wavelength instead of decreasing, which was the case in Fig. 5.2a.

The green dots in Fig. 5.5a are again the calculated Rayleigh reflectances in the residue calculation, at 340 and 380 nm. The residue for this scene was comparable to that of the desert dust case, $r = 3.45$, but because of the bright scene, the adjusted surface contribution c_a that is used in the residue calculation (Eq. 5.8) is now much higher ($A_s = 0.33$) than in the DDA case ($A_s = 0.046$). Since the surface albedo is not wavelength dependent, the reflectance difference of the green dots is much less than in the desert dust case, i.e. the slope of the spectrum is smaller.

In order to understand the radiative transfer processes involved in a BBA polluted cloudy scene, three models for the mixture of aerosols and cloud droplets were constructed (Fig. 5.6). The first model represents a scene with two separate layers, one with only BBA and one with cloud droplets. The second model represents a model of one layer, with an internal mixture of aerosols and cloud droplets, for which an effective single scattering albedo is determined. Finally, the third model is a more sophisticated one-layer model, representing an external mix of water droplets and aerosols, with nonabsorbing water droplets and absorbing aerosols. In all models the thickness of the layers is 1 km and the total optical thickness of each model is always the same at 550 nm (see Table 5.2 for the layer parameters).

Model 1, layered The spectrum of the two separate cloud and aerosol layers was fitted to the measurements using an aerosol optical thickness of 0.3 and a cloud optical thickness of 19.7. The optical properties of the cloud droplets and smoke aerosols were determined using Mie theory, with the size parameters listed in Table 5.1. The cloud was placed in the

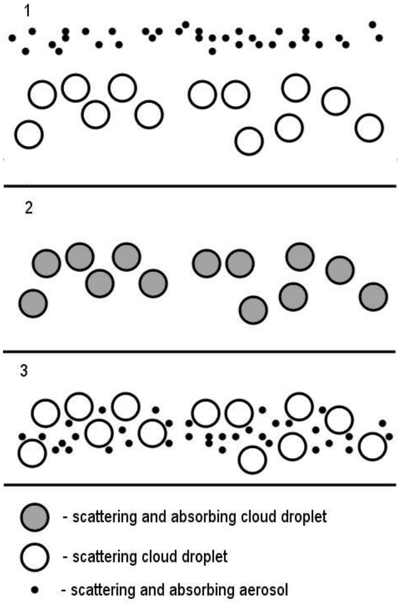

Figure 5.6: *Conceptual models of the distribution of cloud droplets and biomass burning aerosols in the polluted cloud scene. 1. Layered model. Cloud droplets and aerosols are in separate layers, with the cloud layer above the aerosol layer. 2. Internal mix. The aerosols are coated with water, resulting in cloud droplets with an absorbing core. 3. External mix. The cloud droplets and aerosols are mixed in the same layer, but not internally. The cloud droplets are large scattering aerosols and the aerosols are small absorbing aerosols.*

bottom one kilometre of the atmosphere and the aerosol layer was directly on top of the cloud layer. The spectrum of this scene is plotted in Fig. 5.5a as the solid black line and simulates the measured scene reflectance outside absorption bands reasonably well. It is monotonically increasing with wavelength until about 1200 nm like the measured scene reflectance, although the slope is a little smaller. The drop in single scattering albedo around 1400 nm is due to absorption by the water droplets.

In Fig. 5.5b the wavelength dependence of the optical thickness (purple) and the single scattering albedo (green) are given for the aerosols (dotted lines), the water droplets (dashed lines) and the total of both layers (solid lines). The values for 340, 550 and 1000 nm are also given in Table 5.2. The single scattering albedo of the aerosols is decreasing with wavelength, as was also retrieved from AERONET measurements for African savanna smoke aerosols [*Dubovik et al.*, 2002a]. The single scattering albedo of water droplets is one for the entire wavelength range, except around 1400 nm. However, the total single scattering albedo is increasing with wavelength due to the strong decrease of AOT with wavelength. In the UV the effect of absorption of the aerosols is much larger than at longer wavelengths, because of the large value of AOT in the UV, even when the aerosol single scattering albedo decreases with wavelength.

When an absorbing aerosol layer overlays a bright cloud, the reflection of radiation by the

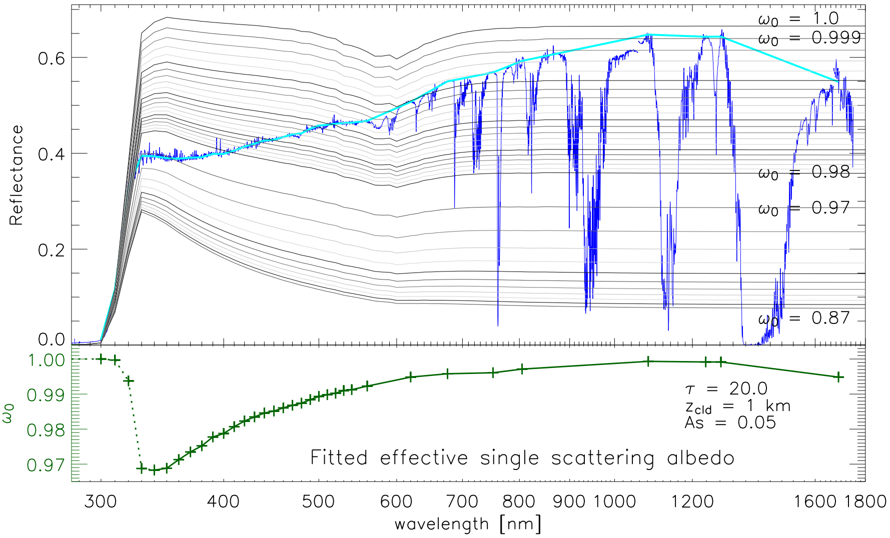

Figure 5.7: *Cloud single scattering albedo fit. Top panel. Measured ocean biomass burning aerosol scene (blue), its envelope outside absorption bands (green) and simulations of polluted cloudy ocean scenes with increasingly lower single scattering albedo (gray scales). Lower panel. Retrieved single scattering albedo from the fit of the mean envelope of the measured spectrum (green line in top panel) to a simulated absorbing cloudy scene spectrum.*

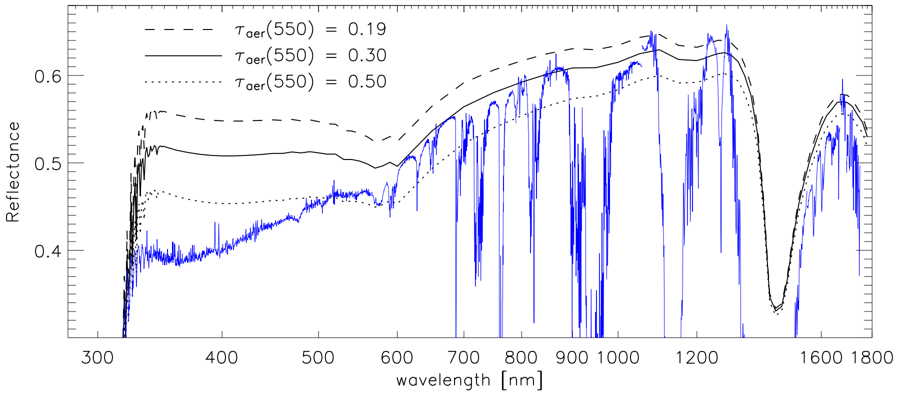

Figure 5.8: *Multiple simulations of a smoke scene using model three (black lines), compared to the measured BBA scene (blue). The solid black line shows a fit to the measured reflectance spectrum, using a mixture of 99.5% aerosols in number density, corresponding to an aerosol optical thickness at 550 nm of 0.30, which is the same as the AOT of model 1. The reflectance spectra of layers with an AOT of 0.19 and 0.50 are shown for comparison by the dashed and the dotted line, respectively.*

cloud is suppressed by the aerosol layer, due to absorption in the aerosol layer and internal reflections between the scattering cloud and the absorbing aerosol layer. This suppression is strongest at shorter wavelengths, because of the increase of AOT with decreasing wavelength, which is measured by the AAI. Even when the total reflectance of cloud and aerosols is much higher in the UV than the clear sky Rayleigh reflectance, the reflectance in the UV is still lower than that of a cloudy scene or a scene with a bright surface without aerosols. This is contrary to a cloudless aerosol scene with a high AAI, where the aerosols suppress the strongly wavelength dependent Rayleigh scattering.

Changing the height of the aerosol layer above the cloud did not change the simulated reflectance spectrum. This is also different from a cloudless aerosol scene, where the amount of suppressed Rayleigh scattering under the aerosol layer is partly determined by the height of the aerosol layer. In the current case all the cloud multiple scattering is below the aerosol layer. Of course, if the cloud was placed over the aerosol layer the opaque cloud reflected all incident radiation and the effect of aerosol absorption was nullified. The spectrum of a purely scattering cloud layer is plotted in Fig. 5.7 with $\omega_0 = 1$.

Model 2, internal mix The spectrum could also be fitted to a one-layer model (model 2) with absorbing cloud droplets. A lookup table of simulated spectra of clouds with droplets having a range of gray (wavelength independent) single scattering albedos was created, using a simple HG phase function for the cloud droplets, with $g = 0.85$. The cloud spectra were calculated using an optical thickness of the cloud of 20 at all wavelengths, a cloud top altitude of one kilometre and a surface albedo of 0.05. The spectra are plotted in grey-scale in the top panel of Fig. 5.7, together with the measured spectrum (blue).

The spectral effective single scattering albedo of this model was fitted to an averaged envelope of the measured spectrum (cyan line in top panel of Fig. 5.7), representing the spectrum outside the absorption bands. The effective single scattering albedo (lower panel of Fig. 5.7) is smallest around 340 nm at about 0.968 and increases with wavelength until about 1200 nm. The fitted single scattering albedo more or less follows the shape of the measured spectrum above 340 nm, which is not surprising since the individual simulated cloud spectra are almost horizontal lines, except in the O_3 Chappuis band around 600 nm. Below 340 nm the single scattering albedo can have any value, since the distinctions between the cloud spectra vanish due to the strong ozone absorption in the O_3 Hartley-Huggins band.

Model 3, external mix The previous model (2) can be used to constrain the effective single scattering. However, to model the effect of individual cloud droplets and aerosol particles, a one-layer model with a bimodal size distribution (Eq. 5.1), where the aerosols are the fine mode and the cloud droplets are the coarse mode, was created, using the size parameters given in Table 5.2. This represents an external mixture of cloud droplets and aerosols (model 3). The weight w controlled the relative number of aerosols and cloud particles, the optical thickness of the layer was 20 at 550 nm. The spectra for different AOTs are given in Fig. 5.8a.

Using again an AOT of 0.30 at 550 nm (weight = 0.995), the reflectance spectrum can be modelled rather accurately outside absorption bands above about 600 nm, just like with model 1. Below 600 nm however, the steep slope of reflectance with wavelength cannot be reproduced with model 3. The total single scattering albedos and optical thicknesses for this model are the same as the ones of model 1 (Table 5.2 and Fig. 5.5b), but the suppression of cloud reflection in the UV for the mixed layer is less than when the aerosol layer is placed over the cloud layer. This is caused by the homogeneous distribution of aerosols through the layer, whereas the radiation is concentrated in the top of the optically thick layer. Consequently, only aerosols in the top part of the cloud will contribute to absorption of radiation and the effect of the wavelength dependence of the aerosol optical thickness is less than in model 1.

The absorption optical thickness of the biomass burning scene is dependent on the model used to fit the spectrum (Table 5.2). The absorption optical thickness at 340 nm is 0.18 for both models 1 and 3, which is 0.9% of the total optical thickness of the cloud/aerosol layers and only slightly wavelength dependent. Using the simpler one-layer HG cloud model 2, the absorption optical thickness increases to 0.64 at 340 nm and decreases strongly with wavelength.

5.4 Discussion and conclusions

In this paper the presence of aerosols was demonstrated in both a clear sky Saharan desert dust ocean scene and a high reflectance (cloud contaminated) savanna smoke ocean scene, using the AAI. The physical mechanism for the AAI is different in clear sky scenes and cloud contaminated scenes, due to the interaction between cloud droplets and aerosols. Understanding this interaction is important to further develop aerosol retrieval algorithms. Aerosols were not demonstrated before in cloud contaminated scenes using space-borne reflectance measurements.

SCIAMACHY reflectance spectra of desert dust and biomass burning aerosol scenes were analysed for the wavelength range 280–1750 nm. The measured desert dust reflectance spectrum was lower in the UV and higher at longer wavelengths than a clear sky spectrum, due to absorption in the UV and scattering at longer wavelengths of large mineral particles. The desert dust spectrum was not critically determined by a particular set of parameters. Nevertheless, a bimodal size distribution of spheres was necessary to fit the spectrum. Although a bimodal distribution is also found from AERONET retrievals for transported desert dust, an artificially increased small mode is created by the assumption of spherical particles [*Dubovik et al.*, 2002b]. However, the application of a nonspherical model is beyond the scope of this paper.

The measured reflectance spectrum of the biomass burning aerosol scene showed a high reflectance in the UV, increasing with wavelength. The suppression of cloud multiple scattering due to absorption by aerosols is more efficient in the UV, because of the decreasing AOT with wavelength, even if the refractive index of smoke aerosols is wavelength independent [*Dubovik et al.*, 2002a; *Torres and Barthia*, 1999], which yields an increasing single scattering albedo with wavelength. This decreases the reflectance in the UV compared to that of a normal cloud scene, which is measured by the AAI. The effect is strongest when an aerosol layer is placed above the cloud, because in an optically thick cloud the radiation is concentrated in the top of the cloud. However, in a layer with an external mix of aerosol and cloud droplets the effect can also be observed.

The radiation in the cloud can also be absorbed by cloud droplets which are internally mixed with smoke aerosols. The mass absorption efficiency of a black carbon particle coated with a water layer is generally greater than that of a pure black carbon particle, because the nonabsorbing water shell increases the total cross-sectional area of the particle and focuses light toward the absorbing core [*Martins et al.*, 1998]. This is valid for particles with radii of around 0.1 μm with a shell in the same order of size, where the water droplets used in this study had effective radii of 6 μm. However, additional absorption by water droplets or water coated aerosols cannot be excluded.

The suppression of cloud multiple scattering is stronger at shorter wavelengths for small (smoke) particles, due to the strong decrease of AOT with wavelength in the UV, which is detected by the AAI in the BBA polluted cloud case. Smoke was detected before over bright surfaces using the AAI over snow and ice scenes in Greenland [*Hsu et al.*, 1999a]. There, the high AAIs were attributed to suppression of wavelength dependent Rayleigh scattered radiation between the surface and the aerosol layer. However, the present study shows that decrease of AOT with wavelength is a more likely mechanism for the high AAI value in case of a bright surface.

The slope of the spectrum in the UV, and hence the AAI, did not change with the height of the aerosol layer above the cloud, as long as the aerosols are above the cloud, since multiple scattering by the cloud is dominant over Rayleigh scattering. This would imply that the AAI is capable of detecting small particles close to the surface over bright surfaces.

The effect of desert dust in the scene, on the other hand, is the suppression of the strongly wavelength dependent Rayleigh scattering by the coarse mode mineral particles, and to a lesser degree the wavelength dependent (increasing) single scattering albedo of the mineral particles in the UV. The slope of the spectrum in the UV, and the value of AAI, is strongly dependent on the amount of Rayleigh scattering under the aerosol layer, and thus the height of the aerosol layer [*Torres et al.*, 1998; *De Graaf et al.*, 2005]. However, if the optical properties of desert dust are strongly wavelength dependent in the UV, as suggested by *Sinyuk et al.* [2003], also desert dust can be detected close to the ground [*Mahowald and Dufresne*, 2004].

The spectrum presented for the desert dust case was a typical, often observed spectrum. Desert dust is usually found in warm, continental, cloudless air. Good estimates for the AOT can be found for these cases, using both ground-based and space-borne instruments, although the latter often need a dark surface, which can be a problem over deserts. In biomass burning cases the spectra are much more variable. The presented spectrum is found only for BBA scenes, but BBA scene spectra with reflectances decreasing with wavelength also occur frequently, and cannot easily be separated from desert dust scenes [*De Graaf et al.*, 2006]. Those BBA scenes, however, have a much lower AAI. An inspection of occurrences of different BBA scenes in 2004 suggests that cloudless BBA scenes over oceans never have an AAI larger than one. However, cloudless ocean BBA scenes are very hard to find, since clouds are formed almost immediately when BBA enter moist air (although the survey was performed with SCIAMACHY, which has a large footprint, 30×60 km^2). On the basis of this survey we conclude that ocean BBA scenes with a high AAI are invariably cloudy scenes, like the one presented in this paper. This suggests that clouds enhance the AAI signal and that these clouds are polluted clouds.

The AAI method is therefore extremely suitable for the detection of aerosols in high reflectance scenes. AOT retrievals using radiance measurements usually neglect cloudy scenes. However, clouds and aerosols are closely linked, and our quantitative knowledge of aerosol-cloud interactions will greatly benefit from direct measurement of aerosol properties inside clouds. Unfortunately, the conversion of AAI measurements into AOT or other aerosol properties is hampered by the dependence of the AAI on many related aerosol and atmospheric parameters [*Herman et al.*, 1997; *Torres et al.*, 1998; *De Graaf et al.*, 2005].

A quantitative measure of aerosol absorption using the AAI is the absorption optical thickness [*Torres et al.*, 2005]. In this study the absorption optical thickness was derived using the various models. The absorption optical thickness of desert dust is strongly decreasing with wavelength, as both the single scattering albedo and the optical thickness of the aerosols are wavelength dependent. The biomass burning case shows that the absorption optical thickness is dependent on the model used to fit the spectrum. The AAI and absorption optical thickness can be valuable quantities to estimate the amount of globally absorbed radiation in the atmosphere due to absorbing aerosols in cloudy scenes. However, in that case a good model is necessary to estimate the optical thickness and single scattering albedos of the aerosols and clouds.

Acknowledgements The MODIS team is acknowledged for the use of the MODIS data. M. Scheele is acknowledged for his help with the TRAJKS simulation and E. Bösche for his work on the bimodal size distribution calculations.

6

Summary and Outlook

In this thesis the Absorbing Aerosol Index (AAI) data from space-borne spectrometers SCIAMACHY and GOME were analysed, to improve the space-borne retrieval of aerosol properties. The AAI is a threshold quantity, namely the positive part of the residue which is sensitive to UV-absorbing aerosols. The AAI is hard to interpret in statistical analyses due to neglect of half of a normal distribution (Fig. 4.7). Therefore, the residue was considered in most of this thesis.

6.1 Summary

Sensitivities of the residue In chapter 2 an extensive analysis confirmed known sensitivities of the residue and revealed sensitivities for Mie scattering aerosols unknown so far. In chapter 4 the change of residue due to a change of UV wavelengths was confirmed and in chapter 5 the effect of the presence of clouds in the scene on the residue was shown. A short overview of the sensitivities of the residue will be given.

- The most important sensitivities of the residue are due to aerosol optical thickness and single scattering co-albedo (Figs. 2.3a and 2.4a). The residue is linearly proportional to the product of these aerosol properties (the absorbing optical thickness) due to the suppression of Rayleigh scattering. However, since the amount of Rayleigh scatterers below the aerosol layer determines the amount of suppressed scattering, the residue is dependent on aerosol layer height, which is often unknown (Fig. 2.4b).

- The spectral dependence of the absorption efficiency of the aerosols is important for the residue, since the residue is a measure for the slope of the reflectance between two (UV) wavelengths. Large mineral aerosols have a strong spectral dependence of the imaginary part of the refractive index, creating a positive residue even without suppression of Rayleigh scattering (chapter 2). Small smoke aerosols have a strong spectral dependence of optical thickness in the UV, creating a higher residue than gray absorbers. This effect is more pronounced when clouds in the scene increase the multiple scattering under the aerosol layer (chapter 5).

- The effect of clouds is to pronounce the spectral dependence of the absorption and reduce the effect of suppression of Rayleigh scattering (chapter 5). The increase of reflectance induced by a cloud under an aerosol layer reduces the relative amount of Rayleigh multiple scattering. Therefore, the residue of gray absorbers decreases for increasing cloud optical thickness and increases for nongray absorbers (Fig. 5.5). The height of the aerosol layer above the cloud is of less importance for increasing cloud optical thickness, since all the scattering is inside (the upper part of) the cloud. However, when the aerosol layer is inside or below the cloud, the absorption by the aerosols is decreased and the residue rapidly decreases to zero (Fig. 2.7a).

- The effect of increasing surface albedo is the same as for a cloud beneath the aerosol layer. However, in the UV most surfaces are dark. The effect of reduced surface pressure (mountains) is about 1.5 residue units increase for every 100 hPa decrease of pressure for a surface albedo of 0.05 (Fig. 2.7b). For increasing surface albedo this effect is decreased, because of the reduced relative contribution of Rayleigh scattering (only 0.1 units of residue increase for every 100 hPa decrease of pressure for a surface albedo of 0.6).

- The effect of different UV wavelengths for which the residue is calculated is shown in Figs. 2.8 and 4.6 and Eq. 5.8. Increasing the range between the two wavelengths increases the residue linearly by about 2% per nanometre increase for the Rayleigh scattering suppression. However, changing the reference wavelength has nonlinear effects, since the reflectance at the reference wavelength is dependent on geometry and surface albedo, and this changes the surface contribution in the residue calculations. The effect of changing the wavelength range in case of nongray absorbers is dependent on the spectral dependence of the absorption of the aerosols.

- The sensitivity of the residue is 0.43 residue units for 1% error in the reflectance, which makes it a very sensitive calibration parameter. Neglect of polarisation in the radiative transfer code results in errors of 10–15% in the calculated reflectances in the residue calculations, which induces errors of up to 6.5 units in residue (chapter 4).

A retrieval algorithm for the residue involves the determination of measured reflectances at two or more wavelengths and an initial tabulation of precomputed Rayleigh atmospheres. The latter has become relatively easy with the availability of radiative transfer codes accounting for multiple scattering and polarisation, both essential for a successful application of the residue method. The continued recording of residues from space-based instruments provides valuable information on distributions of UV-absorbing aerosols over both land and ocean. Therefore, the retrieval of residues is recommended for current and future satellite missions. Currently, the AAI is determined off-line from SCIAMACHY data and operationally for OMI on EOS-Aura. In the summer of 2006 GOME-2 will be launched and an AAI retrieval is planned for this instrument.

GOME and SCIAMACHY AAI The residue method is very sensitive to calibration errors and can be used to monitor reflectance errors and degradation of the satellite instruments. The AAI was derived from GOME and SCIAMACHY data (chapters 2 and 4). The GOME AAI was calculated from calibrated reflectances from 1995 – 2000. The reflectances from GOME show a degradation of the sensor in the UV from 1999 onward, visible in the retrieved AAI as an exponential decay. Before 1999 the global mean GOME AAI was very stable: a decreasing trend of only -0.029 in global averaged residue per year was found, which amounts to a reflectance error of 0.07%. The error in the AAI derived from SCIAMACHY data before 2004 was difficult to estimate due to the large amount of missing data. After 2004 the SCIAMACHY AAI correlated well with the TOMS AAI, although the use of different wavelengths makes a good comparison difficult. The reflectances of SCIAMACHY suffer from radiometric calibration errors, which were corrected before determining the AAI. The accuracy of the correction factors is about 0.5 – 1.0%.

Regions where UV-absorbing aerosols are commonly found were studied in chapter 3. The presence of UV-absorbing aerosols was confirmed in desert areas and regions with an abundance of biomass. In monsoonal areas dust and biomass burning aerosols are common in the dry season, but absent during the wet season. Negative residues coincide well with precipitation data. Negative residues, due to scattering aerosols and clouds, contain a wealth of information, but are not easy to interpret. Closer examination of negative and small residues are recommended to quantify the effect of scattering aerosols and clouds on the residue.

Additional information in reflectance spectra Reflectance data in a large spectral range from GOME (335 – 772 nm) and SCIAMACHY (280 – 1750 nm) were used to study the effect of UV-absorbing aerosols in the scene on the reflectance spectrum (chapters 3 and 5). Over land the reflectances in the visible and near-IR are determined by the high surface albedo. Over oceans, Saharan dust scenes showed decreasing reflectance with increasing wavelength, although the slope is much less than that of a pure Rayleigh atmosphere. Since Saharan dust is often found in dry, hot, continental air, most dust scenes are cloudless and have a low reflectance. An extensive analysis of the spectrum of one typical cloudless ocean scene with Saharan dust, using the large spectral range of SCIAMACHY and radiative transfer simulations, showed that the coarse mineral aerosols cause a net absorbing effect in the UV, which is detected by the AAI, and a net scattering effect in the visible and near-IR. Fine mode mineral aerosols contribute little to the change of the reflectance spectrum compared to that of a Rayleigh atmosphere.

Ocean biomass burning scenes are much more diverse than desert dust scenes. The spectra for ocean biomass burning scenes varied from low reflectance spectra for cloudless biomass burning scenes, decreasing with increasing wavelength, to high reflectance spectra for cloud contaminated biomass burning scenes, increasing with increasing wavelength. Cloudless biomass burning scenes invariably have a small AAI (lower than about one), although completely cloudless biomass burning scenes are hard to find with SCIAMACHY due to its large footprint. Because biomass burning aerosols are very efficient cloud condensation nuclei, clouds are quickly formed when biomass burning aerosol plumes encounter moist ocean air. Cloudy biomass burning scenes often have a high AAI. The presence of clouds in or under the aerosol layer enhances the effect of the spectrally varying aerosol optical thickness on the residue, which is very strong in the UV for small particles like smoke particles.

Currently, a general aerosol type discrimination from reflectance spectra is not possible for desert dust and biomass burning aerosols. However, high reflectance and high AAI scenes over oceans were not observed for desert dust scenes, and are invariably caused by biomass burning aerosols in combination with clouds. More spectral information of aerosol scenes over dark ocean scenes can help identify spectral fingerprints of aerosols on the reflectance spectrum. More importantly, detailed analyses of reflectance spectra can help identify the processes which govern the transfer of light in aerosol-laden atmospheres, with and without clouds, and with different types of aerosols.

The interaction between (biomass burning) aerosols and clouds that was demonstrated in chapter 5 of this thesis, proves the unique capability of the residue method to retrieve aerosol information in cloud contaminated scenes. Using the difference of reflectance measurements at two wavelengths and comparing it to known properties of a modelled atmosphere, the effects of clouds can be separated from that of aerosols. This provides a valuable tool to estimate the aerosol absorption optical thickness on a global scale, including cloudy scenes that are normally neglected in aerosol retrievals. Closer investigation of the interaction between clouds and aerosols with this tool will help quantify the indirect effects of aerosols.

6.2 Outlook

The application of the residue method to GOME and SCIAMACHY revealed the large sensitivity of the method for calibration errors. Once the method is developed, which implies an initial calculation of Rayleigh atmosphere LookUp Tables and (operational) processing of calibrated radiances and irradiances, the method is easy to apply and very suitable for monitoring of the degradation of UV-sensors. Long-term trends of AAI in absorbing-aerosol free areas, which can be found in remote areas over the Pacific oceans or Antarctica, may be good indicators for the performance of space-borne sensors, and so the AAI may help in-flight calibration. However, sporadic occurrences of aerosol events must be accurately detected in these cases, and the application over Antarctica may be hampered by large solar zenith angles.

The separation of aerosol types on the basis of reflectance and residue measurements is difficult, as was demonstrated in chapter 3. However, aerosol type identification on the basis of spectral measurements would be enormously helpful for aerosol retrieval schemes, and deserves further study. Data from the space-borne spectrometers SCIAMACHY and GOME contain a wealth of unexplored spectral information, which is worthwhile inspecting, especially now the calibration of SCIAMACHY reflectance data is improving. More statistical and case studies of known aerosol events will help improve aerosol retrieval algorithms.

A positive AAI often results from suppression of Rayleigh scattering below the aerosol layer. However, *Mahowald and Dufresne* [2004] showed that the strong wavelength-dependence of the imaginary part of the refractive index of mineral desert dust, as found by *Sinyuk et al.* [2003], also produces positive residues, even close to the ground. The results in chapters 2 and 5 show that the strong wavelength-dependence of the optical thickness of smoke also produce positive residues. This will be a general result for small, absorbing particles, which usually have a decreasing AOT in the UV with increasing wavelength.

Furthermore, suppression of multiple scattering in clouds by aerosols can also be detected using the AAI, as demonstrated in chapter 5. The detection of aerosol information in cloud contaminated scenes using spectrometers is a new and exciting result and should be explored further. The AAI can be used to estimate the global amount of aerosol abundance in cloud covered areas, using direct measurements. Furthermore, the ability to measure clouds and aerosols in one scene offers possibilities of measuring and studying indirect aerosol effects. However, in this thesis only one case of a cloud contaminated smoke scene was investigated. A preliminary study of high reflectance scenes from SCIAMACHY showed that in the case of smoke events, the AAI is probably enhanced by cloud contamination, a process which is not yet fully understood. This, and other cloud-aerosol processes, should be explored before an estimate of global absorbing aerosol abundance is feasible. Furthermore, more generic aerosol models should be tested, since in chapter 5 only two aerosol models were chosen, which were best estimates for the cases presented.

References

Abel, S. J., H. J. Highwood, J. M. Haywood and M. A. Stringer, The direct radiative effect of biomass burning aerosols over southern Africa, *Atmos. Chem. Phys.*, *5*, SREF-ID: 1680-7324/acp/2005-5-1999, 2005.

Acarreta, J. R. and P. Stammes, Calibration Comparison Between SCIAMACHY and MERIS Onboard ENVISAT, *IEEE Geoscience and Remote Sensing Letters*, *2*(1), 31–35, 2005.

Ackerman, A. S., O. B. Toon, D. E. Stevens, A. J. Heymsfield, V. Ramanathan and E. J. Welton, Reduction of Tropical Cloudiness by Soot, *Science*, *288*, 1042–1047, DOI: 10.1126/science.288.5468.1042, 2000.

Albrecht, B., Aerosols, Cloud Microphysics, and Fractional Cloudiness, *Science*, *245*, 1227–1230, 1989.

Alpert, P. and E. Ganor, Sahara mineral dust measurements from TOMS: Comparison to surface observations over the Middle East for the extreme dust storm, March 14-17, 1998, *J. Geophys. Res.*, *106*, D16, DOI: 10.1029/2000JD900366, 2001.

Anderson, G. P., S. A. Clough, F. X. Kneizys, J. H. Chetwynd and E. P. Shettle, AFGL atmospheric constituent profiles, *Tech. Rep. AFGL-TR-86-0110*, Air Force Geophysics Laboratory, 1986.

Ångström, A., On the atmospheric transmission of sun radiation and on dust in the air, *Geograf. Ann. Deut.*, *11*, 156–166, 1929.

Balzer, W., R. Spurr, W. Thomas, K. Kretschel and M. Bollner, Sciamachy level 1b to 2 nrt processing input/output date definition, *Tech. Rep. ENV-TN-DLR-SCIA-0010, Issue 3/B*, Dtsch. Zent. für Luft- und Raumfahrt, Oberpfaffenhofen, Germany, 2000.

Bergstrom, R. W., P. B. Russell and P. Hignett, Wavelength Dependence of the Absorption of Black Carbon Particles: Predictions and Results from the TARFOX Experiment and Implications for the Aerosol Single Scattering Albedo, *J. Atmos. Sci.*, *59*, 567–577, DOI: 10.1175/1520-0469, 2002.

Bishop, J. K. B., R. E. Davis and J. T. Sherman, Robotic Observations of Dust Storm Enhancement of Carbon Biomass in the North Pacific, *Science*, *298*, 817–821, DOI: 10.1126/science.1074961, 2002.

Borde, R. and J. Verdebout, Remote sensing of aerosols optical thickness over various sites using seawifs or vegetation and ground measurements., *Remote Sens. Environ.*, *86*(D14), 42–51, 2003.

Bösche, E. et al., *manuscript in preparation*, 2006.

Bovensmann, H., J. P. Burrows, M. Buchwitz, J. Frerick, S. Noël, V. V. Rozanov, K. V. Chance and A. P. H. Goede, SCIAMACHY: Mission Objectives and Measurement Modes, *J. Atmos. Sci.*, *56*(2), 127–150, DOI: 10.1175/1520-0469, 1999.

Burrows, J. P., M. Weber, M. Buchwitz, V. Rozanov, A. Ladstätter-Weißenmayer, A. Richter, R. DeBeek, R. Hoogen, K. Bramstedt, K.-U. Eichmann, M. Eisinger and D. Perner, The Global Ozone Monitoring Experiment (GOME): Mission Concept and First Scientific Results, *J. Atmos. Sci.*, *56*(2), 151–175, DOI: 10.1175/1520-0469, 1999.

Chambers, S. D., J. Beringer, J. T. Randerson and F. S. Chapin III, Fire effects on net radiation and energy partitioning: Contrasting responses of tundra and boreal forest ecosystems, *J. Geophys. Res.*, *110*, D09106, DOI: 10.1029/2004JD005299, 2005.

Chandrasekhar, S., *Radiative Transfer*, 393 pp., Dover, Mineola, N.Y., 1960.

Chen, L.-W. A., H. Moosmüller, W. P. Arnott, J. C. Chow, J. G. Watson, R. A. Susott, R. E. Babbitt, C. E. Wold, E. N. Lincoln and W. M. Hao, Particle emissions from laboratory combustion of wildland fuels: In situ optical and mass measurements, *Geoph. Res. Lett.*, *33*, L04803, DOI: 10.1029/2005GL024838, 2006.

Chiapello, I., J. M. Prospero, J. R. Herman and N. C. Hsu, Detection of mineral dust over the North Atlantic Ocean and Africa with the Nimbus 7 TOMS, *J. Geophys. Res.*, *104*, D8, DOI: 10.1029/1998JD200083, 1999.

Colarco, P. R., O. B. Toon, O. Torres and P. J. Rasch, Determining the UV imaginary index of refraction of Saharan dust particles from Total Ozone Mapping Spectrometer data using a three-dimensional model of dust transport, *J. Geophys. Res.*, *107*(4289), D16, DOI: 10.1029/2001JD000903, 2002.

D'Almeida, G. A., A model for Saharan dust transport, *J. Climate Appl. Meteor.* , *24*, 903–916, 1986.

Darmenova, K., I. N. Sokolik and A. Darmenov, Characterization of east Asian dust outbreaks in the spring of 2001 using ground-based and satellite data, *J. Geophys. Res.*, *110*, D02204, DOI: 10.1029/2004JD004842, 2005.

Dave, J. V., Effects of aerosols on the estimation of total ozone in an atmospheric column from the measurements of its ultraviolet radiance, *J. Atmos. Sci.*, *35*, 889–911, 1978.

Dave, J. V. and C. L. Mateer, A preliminary study on the possibility of estimating total atmospheric ozone from satellite measurements, *J. Atmos. Sci.*, *24*, 414–427, 1967.

De Graaf, M. and P. Stammes, First verification of SCIAMACHY's Absorbing Aerosol Index product, in *Envisat Calibration Review Proceedings*, ESA Special publication SP–531, 2002.

De Graaf, M. and P. Stammes, SCIAMACHY Absorbing Aerosol Index. Calibration issues and global results from 2002 – 2004, *Atmos. Chem. Phys.*, *5*, 3367–3389, SREF-ID: 1680-7324/acp/2005-5-2385, 2005.

De Graaf, M., L. G. Tilstra and P. Stammes, SCIAMACHY absorbing aerosol index: the scientific product compared to the operational product and TOMS data, in *Proceedings of the Second Workshop on the Atmospheric Chemistry Validation of ENVISAT (ACVE-2)*, ESA Special publication SP-562, 2004.

De Graaf, M., P. Stammes, O. Torres and R. B. A. Koelemeijer, Absorbing Aerosol Index: Sensitivity Analysis, application to GOME and comparison with TOMS, *J. Geophys. Res.*, *110*, D01201, DOI: 10.1029/2004JD005178, 2005.

De Graaf, M., P. Stammes and I. Aben, Temporal and spectral variation of desert dust and biomass burning aerosol scenes from 1995 – 2000 using GOME, *Atmos. Chem. Phys. Disc.*, *6*, 1321–1353, SREF-ID: 1680-7375/acpd/2006-6-1321, 2006.

De Haan, J. F., P. B. Bosma and J. W. Hovenier, The adding method for multiple scattering calculations of polarized light, *Astron. Astrophys.*, *183*, 371–391, 1987.

De Rooij, W. A. and C. C. A. H. van der Stap, Expansion of Mie scattering matrices in generalized spherical functions, *Astron. Astrophys.*, *131*, 237–248, 1984.

DeMott, P. J., K. Sassen, M. R. Poellet, D. Baumgardner, D. C. Rogers, S. D. Brooks, A. J. Prenni and S. M. Kreidenweis, African dust aerosols as atmospheric ice nuclei, *Geoph. Res. Lett.*, *30*(14), 1732, DOI: 10.1029/2003GL017410, 2003.

Deuzé, J.-L., P. Goloub, M. Herman, A. Marchand, G. Perry, S. Susana and D. Tanré, Estimate of the aerosol properties over the ocean with POLDER, *J. Geophys. Res.*, *105*, D12, DOI:

10.1029/2000JD900148, 2000.

Diaz, J. P., M. Arbelo, F. J. Expósito, G. Podestá, J. M. Prospero and R. Evans, Relationship between errors in AVHRR-derived sea surface temperature and the TOMS aerosol index, *Geoph. Res. Lett.*, *28*(10), 1989–1992, DOI: 10.1029/2000GL012446, 2001.

Diner, D. J., W. A. Abdou, C. J. Bruegge, J. E. Conel, K. A. Crean, B. J. Gaitley, M. C. Helmlinger, R. A. Kahn, J. V. Martonchik, S. H. Pilorz and B. N. Holben, MISR aerosol optical depth retrievals over Southern Africa during the SAFARI-2000 dry season campaign, *Geoph. Res. Lett.*, *28*(6), 3127–3130, DOI: 10.1029/2001GL013188, 2001.

Dubovik, O., B. N. Holben, T. F. Eck, A. Smirnov, Y. J. Kaufman, M. D. King, D. Tanré and I. Slutsker, Variability of Absorption and Optical Properties of Key Aerosol Types Observed in Worldwide Locations, *J. Atmos. Sci.*, *59*(3), 590–608, DOI: 10.1175/1520-0469, 2002a.

Dubovik, O., B. N. Holben, T. Lapyonok, A. Sinyuk and M. I. Mishchenko, Non-spherical aerosol retrieval method employing light scattering by spheroids, *Geoph. Res. Lett.*, *29*(10), 1415, DOI: 10.1029/2001GL014506, 2002b.

Duncan, B. N., I. Bey, M. Chin, L. J. Mickley, T. D. Fairlie and R. V. Martin, Indonesian wildfires of 1997: Impact on tropospheric chemistry, *J. Geophys. Res.*, *108*(D15), D154458, DOI: 10.1029/2002JD003195, 2003.

Eckardt, F. D. and N. Kuring, SeaWiFS identifies dust sources in the Namib Desert, *Int. J. Rem. Sens.*, *26*(19), 4159 – 4167, DOI: 10.1080/01431160500113112, 2005.

Fournier, N., P. Stammes, M. de Graaf, R. van der A, A. Piters, M. Grzegorski and A. Kokhanovsky, Improving cloud information over deserts from SCIAMACHY Oxygen A-band measurements, *Atmos. Chem. Phys.*, *6*, 163–172, SREF-ID: 1680-7324/acp/2006-6-163, 2006.

Fromm, M., R. Bevilacqua, R. Servranckx, J. Rosen, J. P. Thayer, J. Herman and D. Larko, Pyro-cumulonimbus injection of smoke to the stratosphere: Observations and impact of a super blowup in northwestern Canada on 3–4 August 1998, *J. Geophys. Res.*, *110*, D08205, DOI: 10.1029/2004JD005350, 2005.

Gao, Y., Y. J. Kaufman, D. Tanré, D. Kolber and P. G. Falkowski, Seasonal distributions of aeolian iron fluxes to the global ocean, *Geoph. Res. Lett.*, *28*, 1, DOI: 10.1029/2000GL011926, 2001.

Geogdzhayev, I. V., M. I. Mishchenko, W. B. Rossow, B. Cairns and A. A. Lacis, Global Two-Channel AVHRR Retrievals of Aerosol Properties over the Ocean for the Period of NOAA-9 Observations and Preliminary Retrievals Using NOAA-7 and NOAA-11 Data, *J. Atmos. Sci.*, *59*(3), 262–278, DOI: 10.1175/1520-0469, 2002.

Gleason, J. F., N. C. Hsu and O. Torres, Biomass burning smoke measured using backscattered ultraviolet radiation: SCAR-B and Brazilian smoke interannual variability, *J. Geophys. Res.*, *103*, D24, DOI: 10.1029/98JD00160, 1998.

Goloub, P. and O. Arino, Verification of the consistency of the POLDER aerosol index over land with ATSR-2/ERS-2 fire products, *Geoph. Res. Lett.*, *27*, 24, DOI: 10.1029/1999GL010911, 2000.

Hansen, J., Mki. Sato, A. Lacis and R. Ruedy, The missing climate forcing, *Phil. Trans. Royal Soc. London B*, *352*, 231–240, 1997.

Hansen, J. E. and L. D. Travis, Light scattering in plantary atmospheres, *Space Sci. Rev.*, *16*, 527–610, 1974.

Hasekamp, O. P. and J. Landgraf, Retrieval of aerosol properties over the ocean from multispectral single-viewing-angle measurements of intensity and polarization: Retrieval approach, information content, and sensitivity study, *J. Geophys. Res.*, *110*, D20207, DOI: 10.1029/2005JD006212, 2005.

Hauser, A., D. Oesch, N. Foppa and S. Wunderle, NOAA AVHRR derived aerosol optical depth over land, *J. Geophys. Res.*, *110*, D08204, DOI: 10.1029/2004JD005439, 2005.

Haxby, W. F., G. D. Karner, J. L. LaBrecque and J. K. Weissel, Digital images of combined oceanic and continental data sets and their use in tectonic studies, *Eos. Trans. AGU*, *64*, 995–1004, 1983.

Haywood, J. and O. Boucher, Estimates of the direct and indirect radiative forcing due to tropospheric aerosols: A review, *Rev. Geophys.*, *38*(4), 513–543, 1999RG000078, 2000.

Henyey, L. G. and J. L. Greenstein, Diffuse radiation in the galaxy, *Astrophys. J.*, *93*, 70–83, 1941.

Henzing, J. S., D. J. L. Olivi and P. F. J. V. Velthoven, A parameterization of size resolved below cloud scavenging of aerosols by rain, *Atmos. Chem. Phys. Disc.*, *6*(1), 1355–1384, SREF-ID: 1680-7375/acpd/2006-6-1355, 2006.

Herman, J. R., P. K. Bhartia, O. Torres, C. Hsu, C. Seftor and E. A. Celarier, Global distributions of UV-absorbing aerosols from NIMBUS 7/TOMS data, *J. Geophys. Res.*, *102*, D14, DOI: 10.1029/96JD03680, 1997.

Herman, M., J.-L. D. J. L. Deuz, A. Marchand, B. Roger and P. Lallart, Aerosol remote sensing from POLDER/ADEOS over the ocean: Improved retrieval using a nonspherical particle model, *J. Geophys. Res.*, *110*, D10S02, DOI: 10.1029/2004JD004798, 2005.

Hess, M., P. Koepke and I. Schult, Optical Properties of Aerosols and clouds: The software package OPAC, *Bull. Am. Met. Soc.*, *79*, 831–844, 1998.

Horvath, H., Atmospheric Light Absorption - A review, *Atmos. Env.*, *27A*(3), 293–317, 1993.

Hovenier, J. W., C. V. M. van der Mee and H. Domke, *Transfer of polarized light in planetary atmospheres*, 258 pp., Kluwer, Dordrecht, 2004.

Hsu, N. C., J. R. Herman, P. K. Bhartia, C. J. Seftor, O. Torres, A. M. Thompson, J. F. Gleason, T. F. Eck and B. N. Holben, Detection of biomass burning smoke from TOMS measurements, *Geoph. Res. Lett.*, *23*, 7, DOI: 10.1029/96GL00455, 1996.

Hsu, N. C., J. R. Herman, J. F. Gleason, O. Torres and C. J. Seftor, Satellite Detection of Smoke Aerosols Over A Snow/Ice Surface By TOMS, *Geoph. Res. Lett.*, *26*, 8, DOI: 10.1029/1999GL900155, 1999a.

Hsu, N. C., J. R. Herman, O. Torres, B. N. Holben, D. Tanré, T. F. Eck, A. Smirnov, B. Chatenet and F. Lavenu, Comparison of the TOMS aerosol index with Sun-photometer aerosol optical thickness: Results and applications, *J. Geophys. Res.*, *104*, D6, DOI: 10.1029/1998JD200086, 1999b.

Hsu, N. C., S.-C. Tsay and M. D. King, Aerosol Properties Over Bright-Reflecting Source Regions, *IEEE Geoscience and Remote Sensing Letters*, *42*(3), 557–569, 2004.

Husar, R. B., J. M. Prospero and L. L. Stowe, Characterization of tropospheric aerosols over the oceans with the NOAA advanced very high resolution radiometer optical thickness operational product, *J. Geophys. Res.*, *102*, D14, DOI: 10.1029/96JD04009, 1997.

IPCC, *Climate Change 2001, The Scientific Basis*, 295 pp., Cambridge Univ. Press, Cambridge, 2001.

Janicot, S., A. Harzallah, B. Fontaine and V. Moron, West African Monsoon Dynamincs and Eastern Equatorial Atlantic and Pacific SST Anomalies, *J. Climate*, *11*, 1874–1882, 1998.

Kapustin, V. N., A. D. Clarke, Y. Shinozuka, S. Howell, V. Brekhovskikh, T. Nakajima and A. Higurashi, On the determination of a cloud condensation nuclei from satellite: Challenges and possibilities, *J. Geophys. Res.*, *111*, D04202, DOI: 10.1029/2004JD005527, 2006.

Kaufman, Y. J., P. V. Hobbs, V. W. J. H. Kirchhoff, P. Artaxo, L. A. Remer, B. N. Holben, M. D. King, D. E. Ward, E. M. Prins, K. M. Longo, L. F. Mattos, C. A. Nobre, J. D. Spinhirne, Q. Ji, A. M. Thompson, J. F. Gleason, S. A. Christopher and S.-C. Tsay, Smoke, Clouds, and Radiation - Brazil (SCAR-B) experiment, *J. Geophys. Res.*, *103*, D24, DOI: 10.1029/98JD02281, 1998.

Kaufman, Y. J., D. Tanré and O. Boucher, A satellite view of aerosols in the climate system, *Nature*, *419*, 215–223, DOI: 10.1038/nature01091, 2002.

Kaufman, Y. J., I. Koren, L. A. Remer, D. Tanré, P. Ginoux and S. Fan, Dust transport and deposition observed from the Terra-Moderate Resolution Imaging Spectroradiometer (MODIS) spacecraft over the Atlantic Ocean, *J. Geophys. Res.*, *110*, D10S12, DOI: 10.1029/2003JD004436, 2005.

Keene, W. C., J. M. Lobert, P. J. Crutzen, J. R. Maben, D. H. Scharffe, T. Landmann, C. Hély and C. Brain, Emissions of major gaseous and particulate species during experimental burns of southern African biomass,, *J. Geophys. Res.*, *111*, D04301, DOI: 10.1029/2005JD006319, 2006.

Kim, D. H., B. J. Sohn, T. Nakajima and T. Takamura, Aerosol radiative forcing over east Asia determined from ground-based solar radiation measurements, *J. Geophys. Res.*, *110*, D10S22, DOI: 10.1029/2004JD004678, 2005.

King, M. D., Cloud and Aerosol Properties, Precipitable Water, and Profiles of Temperature and Water Vapor from MODIS, *IEEE Trans. Geosci. Remote Sens.* , *41*(2), 442–458, 2003.

Koelemeijer, R. B. A., P. Stammes, J. W. Hovenier and J. F. de Haan, A fast method for retrieval of cloud parameters using oxygen a band measurements from the Global Ozone Monitoring Experiment, *J. Geophys. Res.*, *106*(D4), 3475–3490,, DOI: 10.1029/2000JD900657, 2001.

Koelemeijer, R. B. A., J. F. de Haan and P. Stammes, A database of spectral surface reflectivity in the range 335-772 nm derived from 5.5 years of GOME observations, *J. Geophys. Res.*, *108*(D2), D24070, DOI: 10.1029/2002JD002429, 2003.

Koren, I., Y. J. Kaufman, L. A. Remer and J. V. Martins, Measurement of the effect of biomass burning aerosol on inhibition of cloud formation over the Amazon, *Science*, *303*, 1342–1345, DOI: 10.1126/science.1089424, 2004.

Krotkov, N. A., P. K. Bhartia, J. R. Herman, V. Fioletov and J. Kerr, Satellite estimation of spectral surface UV irradiance in the presence of tropospheric aerosols 1. Cloud-free case, *J. Geophys. Res.*, *103*(D8), 8779–8794, DOI: 10.1029/98JD00233, 1998.

Kusmierczyk-Michulec, J. and G. de Leeuw, Aerosol optical thickness retrieval over land and water using Global Ozone Monitoring Experiment (GOME) data, *J. Geophys. Res.*, *110*, D10S05, DOI: 10.1029/2004JD004780, 2005.

Liou, K. N., *An Introduction to Atmospheric Radiation*, 583 pp., Academic Press, 2002.

Lohmann, U., A glaciation indirect aerosol effect caused by soot aerosols, *Geoph. Res. Lett.*, *29*(4), DOI: 10.1029/2001GL014357, 2002.

Lohmann, U. and J. Feichter, Global indirect aerosol effects: a review, *Atmos. Chem. Phys.*, *5*, SREF-ID: 1680-7324/acp/2005-5-715, 2005.

Lorenz, L. V., Lysbevaegelsen i og uder en plane lysbolger belyst kulge, *Vidensk. Selk. Skr.*, *6*, 1–62, 1890.

Mahowald, N. M. and J. -L. Dufresne, Sensitivity of TOMS aerosol aerosol index to boundary layer height: Implications for detection of mineral aerosol sources, *Geoph. Res. Lett.*, *31*, L03103, DOI: 10.1029/2003GL018865, 2004.

Martins, J. V., P. Artaxo, C. Liousse, J. S. Reid, P. V. Hobbs and Y. J. Kaufman, Effects of black carbon content, particle size, and mixing on light absorption by aerosols from biomass burning in Brazil, *J. Geophys. Res.*, *103*, D4, DOI: 10.1029/98JD02593, 1998.

McGregor, G. R. and S. Niewold, *Tropical Climatology, An Introduction to the Climates of the Low Latitudes*, 352 pp., John Wiley & Sons, 1998.

Mie, G., Beiträge zur Optik trüber Medien, speziell kolloidaler Metallösungen, *Ann. Phys. Leipzig*, *25*, 377–445, 1908.

Mishchenko, M. I. and L. D. Travis, Satellite retrieval of aerosol properties over the ocean using polarization as well as intensity of reflected sunlight, *J. Geophys. Res.*, *102*, D14, DOI: 10.1029/96JD02425, 1997.

Moulin, C. and I. Chiapello, Evidence of the control of summer atmospheric transport of African dust over the Atlantic by Sahel sources from TOMS satellites (1979–2000), *Geoph. Res. Lett.*, *31*, L02107, DOI: 10.1029/2003GL018931, 2004.

Okin, G. S., Dependence of wind erosion and dust emission on surface heterogeneity: Stochastic modeling, *J. Geophys. Res.*, *110*, D11208, DOI: 10.1029/2004JD005288, 2005.

Palmer, K. and D. Williams, Optical properties of water in the near infrared, *J. Opt. Soc. Am.*, *64*, 1107–1110, 1974.

Pandithurai, G., R. T. Pinker, O. Dubovik and T. O. Aro, Remote sensing of aerosol optical characteristics in sub-Sahel, West Africa, *J. Geophys. Res.*, *106*, D22, DOI: 10.1029/2001JD900234, 2001.

Patterson, E. M., D. A. Gillete and B. H. Stockton, Complex index of refraction between 300 and 700 nm for Saharan aerosol, *J. Geophys. Res.*, *82*, 3153–3160, 1977.

Penner, J. E., S. Z. Zhang and C. C. Chuang, Soot and smoke may not warm climate, *J. Geophys. Res.*, *108*(D21), 4657, DOI: 10.1029/2003JD003409, 2003.

Pincus, R. and M. B. Baker, Effect of precipitation on the albedo susceptibility of clouds in the marine boundary layer, *Nature*, *372*, 250–252, DOI: 10.1038/372250a0, 1994.

Prospero, J. M. and T. Carlson, Saharan air outbreaks over the tropical North Atlantic, *Pure Appl. Geophys.*, *119*, 678–691, 1972.

Prospero, J. M., K. Barrett, T. Church, F. Dentener, R. A. Duce, H. Galloway, H. Levy II, J. Moody and P. Quinn, Atmospheric deposition of nutrients to the North Atlantic basin, *Biogeochem.*, *35*, 27–73, 1996.

Prospero, J. M., P. Ginoux, O. Torres, S. E. Nicholson and T. E. Gill, Environmental characterization of global sources of atmospheric soil dust identified with the Nimbus 7 Total Ozone Mapping Spectrometer (TOMS) absorbing aerosol product, *Rev. Geophys.*, *40*(1), 1002, DOI: 10.1029/2000RG000095, 2002.

Ramanathan, V., P. J. Crutzen, J. T. Kiehl and D. Rosenfeld, Aerosols, Climate, and the Hydrological Cycle, *Science*, *294*, 2119–2124, DOI: 10.1126/science.1064034, 2001.

Reid, J. S., J. E. Kinney, D. L. Westphal et al., Analysis of measurements of Saharan dust by airborne and ground-based remote sensing methods during the Puerto Rico Dust Experiment (PRIDE), *J. Geophys. Res.*, *108*, D19, DOI: 10.1029/2002JD002493, 2003.

Reid, J. S., T. F. Eck, S. A. Christopher, R. Koppmann, O. Dubovik, D. P. Eleuterio, B. N. Holben, E. A. Reid and J. Zhang, A review of biomass burning emissions part III: intensive optical properties of biomass burning particles, *Atmos. Chem. Phys.*, *5*, SREF-ID: 1680-7324/acp/2005-5-827, 2005a.

Reid, J. S., R. Koppmann, T. F. Eck and D. P. Eleuterio, A review of biomass burning emissions part II: intensive physical properties of biomass burning particles, *Atmos. Chem. Phys.*, *5*, SREF-ID: 1680-7324/acp/2005-5-799, 2005b.

Remer, L. A. and Y. J. Kaufman, Aerosol direct radiative effect at the top of the atmosphere over cloud free ocean derived from four years of MODIS data, *Atmos. Chem. Phys.*, *6*, 237–253, SREF-ID: 1680-7324/acp/2006-6-237, 2006.

Remer, L. A., Y. J. Kaufman, D. Tanré, S. Mattoo, D. A. Chu, J. V. Martins, R. R. Li, C. Ichoku, R. C. Levy, R. G. Kleidman, T. F. Eck, E. Vermote and B. N. Holben, The MODIS Aerosol Algorithm, Products and Validation, *J. Atmos. Sci.*, *62*, 947–973, DOI: 10.1175/JAS3385.1, 2005.

Rosenfeld, D., Y. Rudich and R. Lahav, Desert dust suppressing precipitation: a possible desertification feedback loop, *Proc. Natl. Acad. Sci. U.S.A.*, *98*(11), 5975–5980, 2001.

Ruddiman, W. F., The anthropogenic greenhouse era began thousands of years ago, *Climate Change*, *61*(3), 261–293, 2003.

Sassen, K., P. J. DeMott, J. M. Prospero and M. R. Poellet, Saharan dust storms and indirect aerosol effects on clouds: CRYSTAL-FACE results, *Geoph. Res. Lett.*, *30*(12), 1633, DOI: 10.1029/2003GL017371, 2003.

Scheele, M. P., P. Siegmund and P. van Velthoven, Sensivity of trajectories to data resolution and its dependence on the starting point in or outside a tropopause fold, *Meteorol. Appl.*, *3*, 267–273, 1996.

Seftor, C. J., N. C. Hsu, J. R. Herman, P. K. Bartia, O. Torres, W. I. Rose, D. J. Schneider and N. Krotkov, Detection of vulcanic ash clouds from Nimbus 7/total ozone mapping spectrometer, *J. Geophys. Res.*, *102*, D14, DOI: 10.1029/97JD00925, 1997.

Sinyuk, A., O. Torres and O. Dubovik, Combined use of satellite and surface observations to infer the imaginary part of the refractive index of Saharan dust, *Geoph. Res. Lett.*, *30*(D2), 1081, DOI: 10.1029/2002GL016189, 2003.

Sokolik, I. and O. B. Toon, Incorporation of mineralogical composition into models of the radiative properties of mineral aerosol from UV to IR wavelengths, *J. Geophys. Res.*, *104*, D8, DOI: 10.1029/1998JD200048, 1999.

Song-Miao, F., L. W. Horowitz, H. Levy II and W. J. Moxim, Impact of air pollution on wet deposition of mineral dust aerosols, *Geoph. Res. Lett.*, *31*, L02104, DOI: 10.1029/2003GL018501., 2004.

Spichtinger, N., M. Wenig, P. James, T. Wagner, U. Platt and A. Stohl, Satellite detection of a continental-scale plume of nitrogen oxides from boreal forest fires, *Geoph. Res. Lett.*, *28*(24), 4579–4582, DOI: 10.1029/2001GL013484, 2001.

Spurr, R. and W. Balzer, Sciamachy level 1c to 2 off-line processing. algorithm theoretical basis document, *Tech. Rep. ENV-ATB-SAO-SCI-2200-0003, Issue 2*, Dtsch. Zent. für Luft- und Raumfahrt, Oberpfaffenhofen, Germany, 2000.

Spurr, R. J. D., T. P. Kurosu and K. V. Chance, A Linearized discrete Ordinate Radiative Transfer Model for Atmospheric Remote Sensing Retrieval, *J. Quant. Spectrosc. Radiat. Transfer*, *68*, 689–735, 2001.

Stammes, P., Spectral radiance modelling in the UV-visible range, in *IRS 2000: Current problems in atmospheric radiation*, edited by W. Smith and Y. Timofeyev, pp. 385–388, A. Deepak Publishing, Hampton (VA), 2001.

Stohl, A., L. Haimberger, M. P. Scheele and H. Wernli, An intercomparison of results from three trajectory models, *Meteorol. Appl.*, *8*, 127–135, 2001.

Tanré, D. and M. Legrand, On the Satellite Retrieval of Saharan Dust Optical Thickness Over Land: Two Different Approaches, *J. Geophys. Res.*, *196*, D3, DOI: 10.1029/90JD02607, 1991.

Tanré, D., M. Herman and Y. J. Kaufman, Information on aerosol size distribution contained in solar reflected spectral radiances, *J. Geophys. Res.*, *101*, D14, DOI: 10.1029/96JD00333, 1996.

Tanré, D., F. M. Bréon, J. -L. Deuzé, M. Herman, P. Goloub, F. Nadal and A. Marchand, Global observation of anthropogenic aerosols from satellite, *Geoph. Res. Lett.*, *28*, 24, DOI: 10.1029/2001GL013036, 2001.

Tegen, I. and I. Fung, Modeling of mineral dust in the atmosphere: Sources, transport, and optical thickness, *J. Geophys. Res.*, *D11*, 22,897–22,914, 1994.

Tilstra, L. G. and P. Stammes, Alternative polarisation retrieval for SCIAMACHY in the ultraviolet, *Atmos. Chem. Phys.*, *5*, 2099–2107, SREF-ID: 1680-7324/acp/2005-5-2099, 2005.

Tilstra, L. G., G. van Soest, M. de Graaf, J. R. Acarreta and P. Stammes, Reflectance comparison between SCIAMACHY and a radiative transfer code in the UV, in *Proceedings of the Second Workshop on the Atmospheric Chemistry Validation of ENVISAT (ACVE-2)*, ESA Special publication SP-562, 2004.

Tilstra, L. G., G. van Soest and P. Stammes, Method for in-flight satellite calibration in the ultraviolet using radiative transfer calculations, with application to Scanning Imaging Absorption Spectrometer for Atmospheric Chartography (SCIAMACHY), *J. Geophys. Res.*, *110*(D18311), DOI: 10.1029/2005JD005853., 2005.

Torres, O. and P. K. Barthia, Impact of tropospheric aerosol absorption on ozone retrieval from backscattered ultraviolet measurements, *J. Geophys. Res.*, *104*, D17, DOI: 10.1029/1999JD900410, 1999.

Torres, O., J. R. Herman, P. K. Bhartia and Z. Ahmad, Properties of Mount Pinatubo aerosols as derived from Nimbus 7 total ozone mapping spectrometer measurements, *J. Geophys. Res.*, *100*, D7, DOI: 10.1029/95JD01224,, 1995.

Torres, O., P. K. Bhartia, J. R. Herman, Z. Ahmad and J. Gleason, Derivation of aerosol properties from satellite measurements of backscattered ultraviolet radiation: Theoretical basis, *J. Geophys. Res.*, *103*, D14, DOI: 10.1029/98JD00900, 1998.

Torres, O., R. Decae, P. Veefkind and G. de Leeuw, OMI Aerosol Retrieval Algorithm, in *OMI-EOS Algorithm Theoretical Basis Document, Chapter 4*, pp. 1–24, 2001.

Torres, O., P. K. Bhartia, J. R. Herman, A. Sinyuk, P. Ginoux and B. Holben, A long-term record of aerosol optical depth from TOMS observations and comparison to AERONET measurements, *J. Atmos. Sci.*, *59*(3), 398–413, DOI: 10.1175/1520-0469, 2002.

Torres, O., P. K. Bhartian, A. Sinyuk and E. Welton, Total Ozone Mapping Spectrometer measurements of aerosol absorption from space: Comparison to SAFARI 2000 ground-based observations, *J. Geophys. Res.*, *110*, D10S18, DOI: 10.1029/2004JD004611, 2005.

Torricella, F., E. Cattani, M. Cervino, R. Guzzi and C. Levoni, Retrieval of aerosol properties over the ocean using global ozone monitoring experiment measurements: Method and applications to test cases, *J. Geophys. Res.*, *104*, D10, DOI: 10.1029/1999JD900040, 1999.

Tsunematsu, N., T. Sato, F. Kimura, K. Kai, Y. Kurosaki, T. Nagai, H. Zhou and M. Mikami, Extensive dust outbreaks following the morning inversion breakup in the Taklimakan Desert, *J. Geophys. Res.*, *110*, D21207, DOI: 10.1029/2005JD005994, 2005.

Twomey, S. A., The Nuclei of Natural Cloud Formation. Part II: The Supersaturation in Natural Clouds and the Variation of Cloud Droplet Concentrations, *Geofis. Pure Appl.*, *43*, 243–249, 1959a.

Twomey, S. A., The Nuclei of Natural Cloud Formation. Part I: The Chemical Diffusion Method and its Application to Atmospheric Nuclei, *Geofis. Pure Appl.*, *43*, 227–242, 1959b.

Twomey, S. A., The Influence of Pollution on the Shortwave Albedo of Clouds, *J. Atmos. Sci.*, *34*, 1149–1152, 1977.

Van de Hulst, H. C., *Light scattering by small particles*, Wiley, New York, 1957.

Van de Hulst, H. C., *Multiple light scattering*, Academic Press, New York, 1980.

Veefkind, J. P., G. de Leeuw, P. Stammes and R. B. A. Koelemeijer, Regional Distribution of Aerosol over Land, Derived from ATSR-2 and GOME, *Remote Sens. Environ.*, *74*, 377–386, 2000.

Veihelmann, B., H. Volten and W. J. van der Zande, Light reflected by an atmosphere containing irregular mineral dust aerosol, *Geoph. Res. Lett.*, *31*, L04113, DOI: 10.1029/2003GL018229, 2004.

Waquet, F., J.-F. Léon, P. Goloub, J. Pelon, D. Tanré and J.-L. Deuzé, Maritime and dust aerosol retrieval from polarized and multispectral active and passive remote sensors, *J. Geophys. Res.*, *110*, D10S10, DOI: 10.1029/2004JD004839, 2005.

Webster, P. J., Chap. 1: The elementary Monsoon, in *Monsoons*, edited by J. S. Fein and P. Stephens, pp. 3–32, J. Wiley & Sons, 1987.

Yu, H., Y. J. Kaufman, M. Chin, G. Feingold, L. A. Remer, T. L. Anderson, Y. Balkanski, N. Bellouin, O. Boucher, S. Christopher, P. DeCola, R. Kahn, D. Koch, N. Loeb, M. S. Reddy, M. Schulz, T. Takemura and M. Zhou, A review of measurement-based assessments of the aerosol direct radiative effect and forcing, *Atmos. Chem. Phys.*, *6*, 613–666, SREF-ID: 1680-7324/acp/2006-6-613, 2006.

Zhang, S., J. E. Penner and O. Torres, Inverse modeling of biomass burning emissions using Total Ozone Mapping Spectrometer aerosol index for 1997, *J. Geophys. Res.*, *110*, D21306, DOI: 10.1029/2004JD005738, 2005.

Dankwoord

Al staat er op de omslag van dit proefschrift slechts één auteursnaam, zonder de hulp van vele mensen zou dit werk nooit tot stand gekomen zijn. Naast de co-auteurs van de verschillende hoofdstukken zijn er mensen die ik hier graag wil bedanken.
Als eerste mijn promotor, Ilse Aben, voor het accepteren van mijn voorstel tot promotie. De samenwerking was mijns inziens erg aangenaam en vruchtbaar. Dit projekt begon echter bij Piet Stammes, die mij aannam op het SCIAMACHY projekt en direkt mijn promotiewens omzette in een onderzoeks- en publikatietrajekt. Zonder zijn betrokkenheid en wetenschappelijk inzicht was dit boekje er nooit gekomen. Na anderhalf jaar onder Piets vleugels was het tijd voor wat zelfstandigheid en kreeg ik een andere kamergenoot, in de vorm van Gijs. Met Gijs heb ik vele uren in bespreking doorgebracht en mijn jargon is danig vernieuwd; Gijs onderhield tijdens het werk sowieso graag contact met collega's op de afdeling. Op conferenties werd er samen vaak lustig op los gediscussiëerd, met argumenten die menig hoofd deden draaien. Ook tijdens informele momenten als diners en boottochtjes werd kritiek niet geschuwd en ging er van alles over tafel. Maar sommige dingen kunnen beter onbesproken blijven.
Mijn collega's bij AO hebben natuurlijk ook bijgedragen aan de nodige lol, waarvan ik een aantal wil noemen: 'het stukje' van Piet, Gijs, Dominique, Wouter en Nick op onze bruiloft, het leer was erg indrukwekkend; de foute en grappige Internetonzin van Gerben en Eyk; vogels kijken met Marita en Anne; het communiceren tussen Gijs en Wouter (alhoewel vooral zij de lol daarvan inzagen); roddels uitwisselen met Gerd-Jan; beachvolleyballen met Eyk, Rob, Petra, Marita en Janneke. Het beachvolleyballen is met Petra verder geprofessionaliseerd, iets dat we hopelijk nog een tijd lang zullen volhouden, alhoewel de prestaties niet noodzakelijkerwijs beter zullen worden.
Afdelingsoverschrijdend is er ook de nodige afleiding te vinden op het KNMI. Het dinsdagmiddagzwemmen is hopeloos verwaterd, maar heeft een tijd lang voor een zeer welkome conditie gezorgd. Minstens zo sportief was het kerst- en paasklaverjassen, waar ik er bijna van overtuigd ben geraakt dat het vroeger misschien inderdaad wel allemaal beter was. Maar het laatste jaar was het hoogtepunt van de week toch wel de oefensessies in het rokhok, met Erwin, Lucas en Siebren. Vol overgave stortten wij ons op menige briljante liedjes van evenzo briljante bands, om na een paar weken te accepteren dat één en ander toch niet zo geschikt was voor ons. Maar nooit is dat aanleiding geweest om de pret te laten drukken. De beste interafdelingssamenwerking is evenwel met Renske geweest. We hebben een serieuze poging gedaan om t-drinken tot een nationale sport te verheffen. And of course I spent many hours on the Internet 'talking' with Enrica, trying to induce a DoS of the KNMI servers with our email traffic.

Afleiding na het werk vond ik natuurlijk in volleybal, maar hoogtepunt is en blijft klaverjassen met Jop, Gosse, en Erik. Zoals een wijs man zei: „Soms heb je pech.", zo heb ik de laatste tijd een beetje tegenslag gehad, maar dat zal binnenkort zeker weer worden rechtgezet. Bij gelegenheid werden de honneurs waargenomen door Ellen, Astrid, Inge of Sep, wat ook zeer gewaardeerd wordt.

Mijn familie heeft mij altijd gesteund in al mijn ondernemingen en dat was deze keer niet anders, maar het enthousiasme was enigszins onverwacht. Met name mijn schoonfamilie heeft de laatste jaren zeer actief meegeleefd, waarvoor dank. Minder onverwacht, maar oneindig meer gewaardeerd, was de steun van Ellen. Ellen, ik hoop dat je dit kleine hoogtepuntje van mij snel zal doen verbleken.

Martin de Graaf, mei 2006.

Curriculum vitae

Martin de Graaf werd geboren op 16 juni 1973 in Hengelo (O). Na het behalen van het vwo-examen aan het Chr. Lyceum in Almelo was het in 1991 de beurt aan de Rijksuniversiteit Utrecht. In 1993 werd de propedeuse 'Natuurkunde' verkozen boven de destijds nog net niet afgeschafte dienstplicht. Het vervolgcurriculum 'Meteorologie & Fysische Oceanografie' werd een stuk enthousiaster doorlopen, vooral door de veldwerk mogelijkheden. Ook werd in 1995/1996 een bestuursjaar bij de studievereniging 'A-Eskwadraat' vervuld. Het doctoraal-examen werd met goed gevolg afgelegd in 1998 aan de inmiddels omgedoopte Universiteit Utrecht. Dit smaakte naar meer, en nog datzelfde jaar volgde de tweejarige postdoctorale opleiding 'Computational Mechanics' aan de Universiteit Twente. Na een afsluitend jaar bij het Rijksinstituut voor Kust en Zee in Den Haag kon in 2001 de illustere titel 'Master of Technological Design' worden toegevoegd. Terug in Utrecht begon eind 2001 het promotie-onderzoek aan het Koninklijk Nederlands Meteorologisch Instituut, dat uiteindelijk tot dit proefschrift heeft geleid en op 19 juni 2006 verdedigd zal worden.